UNIVERSITÀ DEGLI STUDI DI PADOVA

UNIVERSITA' DEGLI STUDI DI PADOVA

Dipartimento di Ingegneria Industriale DII

Corso di Laurea Magistrale in Ingegneria Aerospaziale

Direct numerical simulation of the hydraulic fracturing of porous media

Relatore: *Prof. Francesco Picano*

Correlatore: *Federico Dalla Barba, Ph.D.*

Laureando: *Luca Placco*

Matricola: 1197613

Anno accademico 2020-2021

Abstract

Hydraulic fracturing indicates the rupture of a solid medium due to pressure applied by a traversing fluid flow. It is a multi-physics, fluid-structure interaction problem, as both fluid and solid mechanics contribute to the phenomenon. We present a study of the fracturing caused by the transition of a generic fluid agent inside a solid porous shell. Crack propagation and fracture mechanics are considered, describing the damaging process of the solid frame subjected to the viscous laminar flow filtering inside. Porous materials represent a typical category involved in this class of problems, being associated with diverse engineering fields and research areas. Strains and fractures caused by the flow are evaluated through the use of Direct Numerical Simulations; Navier-Stokes equations are coupled with the equations of the peridynamics theory to acknowledge solid mechanics and the formation of discontinuities in the structure. A multi-direct Immersed Boundary Method approach is applied to take heed of the time-evolving body surfaces subjected to the fluid stresses. In this manner, the implementation of the no-slip boundary condition is unrelated to the complexity of the solid structure; this allow us to fully describe the deformation of the frame caused by the injected stream. The simulation is performed at a pore-scale, in order to properly capture the crack phenomenon and its development along the structure. The response of the porous structure is then evaluated representing the geometry of the medium through an equivalent capillary model. The efficacy of this configuration is validated through the results obtained from the simulations; ultimately, a basic failure criterion based on the assumptions made is proposed.

Contents

List of figures vii

List of tables ix

1 Introduction **1**

2 Overview of the subject **3**

2.1 Fluid-structure interaction 3

2.2 Mechanics of porous media 4

2.2.1 Physical properties. 4

2.2.2 Models adopted 10

2.3 Hydraulic fracturing 17

2.3.1 Description of the process 17

2.3.2 Types of numerical simulations adopted 19

2.3.3 Environmental impact 20

Chapter conclusions 22

3 Methodology **23**

3.1 FSI implementation 23

3.1.1 Numerical procedures 23

3.1.2 Treatment of meshes 26

3.2 Navier-Stokes equations 32

3.2.1 Direct numerical simulation 33

3.3 Immersed boundary methods 36

3.3.1 Description of the method 36

3.3.2 Numerical implementation 39

3.3.3 Improvements of the method 44

3.4 Peridynamics 47

3.4.1 Fundamentals of peridynamics 48

3.4.2 Numerical discretization 51

Chapter conclusions 55

4 Definition of the problem **57**
4.1 CaNS-ExPS 57
4.1.1 DNS and PD module coupling 57
4.1.2 Dimensional analysis 59
4.1.3 Interface handling and force computation. 61
4.2 Problem configuration 63
4.2.1 Computational domain configuration 64
4.2.2 Geometry generation 65
4.2.3 Definition of the capillary model 67
Chapter conclusions 69

5 Results **71**
5.1 DNS Review 72
5.1.1 Flow initialization 72
5.1.2 Solid initialization 75
5.1.3 Hydraulic fracturing 79
5.2 Comparison of the cases 85
5.2.1 Comparison of the structural evolution 86
5.2.2 Application of the capillary model 89
5.2.3 Failure prediction 92
Chapter conclusions 95

6 Conclusion **97**

Bibliography **99**

List of figures

2.1 Examples of natural porous materials 5
2.2 Computer generated portions of porous media 6
2.3 Velocity contours in 2D non-convex porous media. 7
2.4 Porosity as a function of average sphericity, normalized permeability as a function of average sphericity 8
2.5 Streamlines for different Re inside a porous media composed of cylinders 13
2.6 Permeability vs. porosity of a vesicular basalt, *Saar and Manga* [1999] and natural eruptive material, *Melnik and Sparks* [2002]. 15
2.7 The process of hydraulic fracture 18
2.8 Water use and potential concern in hydraulic fracturing operations 21
2.9 Methane concentrations as a function of distance to the nearest gas well from active and nonactive drilling areas. 22

3.1 Schematic of the monolithic approach and the partitioned approach for fluid-structure interactions. 24
3.2 Schematic of partitioned solver employing for FSI simulation 26
3.3 Two-dimensional structure, unstructured and hybrid mesh 26
3.4 Two-dimensional quadrilateral elements undergoing aspect ratio and skewness deformations. 28
3.5 Two-dimensional conforming, non-conforming and mesh-free configuration . . 29
3.6 Two-dimensional conforming structured multigrid and mesh-free regular and non-regular configuration 31
3.7 Generic solid body immersed in a fluid flow. Schematic of body immersed in a cartesian grid 47
3.8 Transfer of forcing F_l from Lagrangian boundary point X_l to surrounding Eulerian fluid nodes. Distribution functions employed in various studies 41
3.9 L2-norm error of the axial velocity component vs. number of grid points 43

3.10 Illustration of the diffuse distribution of the IBM force around the interface of a particle. Illustration of the shell surrounding a solid particle 46
3.11 Plot of the maximum error in the norm of the Lagrangian velocity $\boldsymbol{U}_l$ 47
3.12 2D schematic of a solid medium discretized with uniform a Lagrangian-peridynamic grid 59
3.13 Schematic of the damage level definition 53
3.14 Schematic of the bond direction for different values of the m factor 54
3.15 Material point $\boldsymbol{X_h}, \boldsymbol{X_b}$ and $\boldsymbol{X_c}$ in a 2D domain; $\boldsymbol{X_b}$ and $\boldsymbol{X_c}$ present truncated family domain being located near the external surface 54

4.1 Flowchart scheme of the algorithm. 60
4.2 2D schematic of the normal probe method adopted to compute the hydraulic stresses on the fluid-solid interface 62
4.3 3D schematic of the computational domain 64
4.4 Flowchart scheme of the porous medium generation algorithm 64
4.5 3D render of an example of the geometrical configuration. 65
4.6 3D render of the adopted computational domain with the final geometrical configuration. 65
4.7 Schematic of the capillary model adopted to represent the porous medium behaviour. 66

5.1 Plot of flow streamlines at the end of the initialization phase 70
5.2 Distribution of the non-dimensional pressure along the x direction; contour of the non-dimensional pressure field 72
5.3 Distribution of the non-dimensional pressure gradient along the x direction . . 72
5.4 Surface contours of the non-dimensional displacement field on different regions of the solid body 75
5.5 Probability density function and cumulative density function of the non-dimensional force density distribution (x) 76
5.6 Probability density function and cumulative density function of the non-dimensional force density distribution (y,z) 76
5.7 Surface contours of the non-dimensional displacement field on different regions of the solid body 78
5.8 Damage factor distributions on the surface of the body to indicate crack propagation 79

5.9 Number of broken particles over the time $t/\tilde{t} \in [2.55, 3.35]$ 81
5.10 Hydraulic fracturing process; plot of flow streamlines, coloured according to the magnitude of the non-dimensional flow velocity together with a 3D render of the porous medium. 82
5.11 3D render of the porous medium employed for the DNS analysis at end of the simulation 83
5.12 3D renders of porous media structural configuration at the end of each corresponding simulation (R1,R2,R10 and R15) 84
5.13 Comparison of the structural quantities of every tested configuration (R1,R2,R5,R10 and R15) over time 85
5.14 Comparison of the distribution of the non-dimensional mean pore radius (for configuration R1,R2,R5,R10 and R15) over time 87
5.15 Distribution of the pressure drop computed with the capillary model together with the reference pressure drop obtained from the DNS 89
5.16 Distribution of the non-dimensional resultant axial force computed with equation (5.4) together with the reference resultant axial force obtained from the DNS for R5 and R15 configurations; corresponding percentage error 92

List of tables

5.1 Physical parameters of the simulations expressed in non-dimensional units; corresponding non-dimensional energy release rate for each simulation 69
5.2 Ratio of the ultimate tensile strength to the wall shear stress at $It = 19000$ for the different structural configurations 91

Chapter 1

Introduction

Hydraulic fracturing defines a field of study associated with diverse engineering categories as it features interaction phenomena between a fluid and a solid phase. It is considered for this reason as a non-linear, multi-physics problem given the involvement of both fluid and solid mechanics. This category of processes are identified as fluid-structure interaction problems and are acknowledged by a plethora of engineering scopes of research as they describe a wide variety of scenarios which ranges from the modeling of aircraft wings and turbine blades to simulating blood flow inside vessels.

In the case here considered, it will be examined and studied the effect of a viscous laminar fluid flow filtering inside a solid porous medium; the analysis that will be carried on will focus on evaluating the phenomenon at a pore-scale level, assessing fracture mechanics and the propagation of the crack around the solid frame due to the pressure of the injected flow.

The strains and fractures caused by the transition of the fluid agent will be evaluated through the use of Direct Numerical Simulations; Navier-Stokes equations are coupled with the equations of the peridynamics theory to acknowledge solid mechanics and the formation of discontinuities in the structure. A multi-direct Immersed Boundary Method approach is used to take heed of the time-evolving body surfaces subjected to the fluid stresses. In this manner, the implementation of the no-slip boundary condition will be unrelated to the complexity of the solid structure; this allow us to fully describe the deformation of the frame caused by the injected stream. The simulation will be performed at a pore-scale level, in order to properly capture the crack phenomenon and its development around the structure.

The present thesis is organized in the following way: firstly, a review of the literature covering our area of interest is addressed. Fluid-structure interaction problems are defined, providing a general outline of their application. Afterwards,

porous materials are characterized, evaluating their distinctive geometrical quantities and corresponding representative models; hydraulic fracturing and the relative crack propagation process is then briefly introduced, together with the typical numerical simulations adopted. Methodology is then presented: the Direct Numerical Simulation technique, the Immersed Boundary Method approach and the Peridynamic theory are examined, evaluating firstly their formulation and subsequently their numerical implementation. Having properly introduced the subject, the configuration that will be studied is presented; all the simulations described in this thesis have been performed by employing a massive MPI parallel solver (CaNS-ExPS [2],[63]), capable of running the computational process that has been set out. A random porous medium generation algorithm has been developed to produce an optimized solid configuration to employ in the final analysis. Five different material configurations will be considered, each of them associated to a different level of material strength.

The results obtained from the numerical simulations are reviewed in-depth; the data collected from the analysis are then employed to evaluate the effectiveness of representing the geometry of the porous frame through an equivalent capillary model, comparing the results of the selected configurations. The failure of the porous structure is ultimately addressed, proposing a basic failure criterion on the made assumptions.

As for the author knowledge, no previous attempts have ever been made to describe the phenomenon of hydraulic fracturing for porous media at a pore-scale level, given the modelling complexity and the high specificity of the analysis. The scientific background surrounding porous materials is undoubtedly very wide, however, the progresses that have been made distribute on a variety of different directions which contribute adversely in giving a clear understanding of the subject. With this present work the author hopes to help clarify the context of study, providing a better insight of what could be of interest for several engineering applications.

Chapter 2

Overview of the subject

Let us begin our review with a summary of the concerning subjects touched by this research. Firstly, fluid-structure interaction problems will be briefly introduced, as they represent the focal point of our scope of interests. The most prevalent computational procedures and meshing techniques adopted will be specifically addressed in the next chapter. Afterwards, the chapter will present the main aspects characterizing a generical porous material involved in this typology of study. Constitutive laws and models also will be presented. The last section will then involve hydraulic fracturing, including a technical description of its general process and the typical numerical strategies adopted to simulate it.

2.1 Fluid-structure interaction

The interaction of a non-rigid body submerged in a flowing liquid can lead to several different physical phenomena involving distinct engineering fields. These may include the response to gusts of aircraft wings, the flutter effect, the behaviour of structures and building to wind force, and even the vibration of the blades inside a compressor or a turbine. All these different cases are acknowledged as fluid-structure interaction problems (FSI) and play a major role in the scientific development of their respective areas of interest. [1],[2]

Examining and understanding these subjects effectively remains a challenge nowadays, due to the strong non-linearity characterizing them; they also involve separate disciplines, presenting the problem more complex to address without a specialized viewpoint. This becomes useful since it's necessary to model both the fluid and the structure to reproduce these phenomena properly. Typically, solids are assumed obeying Hooke's law with deformations described either using a simplified elastic model or, for larger deformations, a more complex nonlinear material. Fluid modelling usually implies laminar flow under the hypothesis of low Reynolds number and constant fluid density (incompressible flow). [4]

As long as analytical solutions are almost unattainable for every type of condition and laboratory experiments are confined to the case studied, only numerical simulations remain employable. These techniques will be reviewed in the next chapter (3.1.1), while for now only a general discussion of the subject will be presented, starting with the object involved by our study.

2.2 Mechanics of porous media

A porous medium is a solid material which features pores in its volume. This void space is identified as empty in the overall dimensions of the body and is determined either continuous if every pore structure is interconnected, or isolated if volumes of the material appear to be confined from the outer environment. The skeletal portion of the material is often called "matrix" or "frame" as they are usually subjected to the flow of a gas or fluid through it. [10]

Being filled with fluid, porous media are typical FSI problems and critical components for a broad range of disciplines and studies such as electrodes for fuel cell and batteries development, reservoirs accessibility and geology; their study is required for a better general understanding of also seawater filtration and underground hydrology, including water contamination. [11,12]

We will first introduce the main aspects characterizing a porous medium and then proceed to assess the models developed to describe their behaviour when traversed by a fluid.

2.2.1 Physical properties

In porous media void space is usually extremely chaotic, as pore size and shape tend to modify across a broad range, being random and dependent on ever-changing processes. In this way, the paths that the solid skeleton provides to the fluid are not straight but full of turns and crosses with other passages; a fluid molecule before exiting from the medium has to travel way longer than its actual effective displacement. For these reasons, only part of their properties can be defined easily: even now these kinds of materials are handled without completely taking into account their complex internal morphology. To evaluate fluid flow inside, conservation laws are averaged over a scale long enough to consider the segment

homogeneous and experimental coefficient are attributed for each medium, given their uniqueness. [13]

We can see in figure 2.1 some examples of different typologies of natural porous materials belonging to various field of interest.

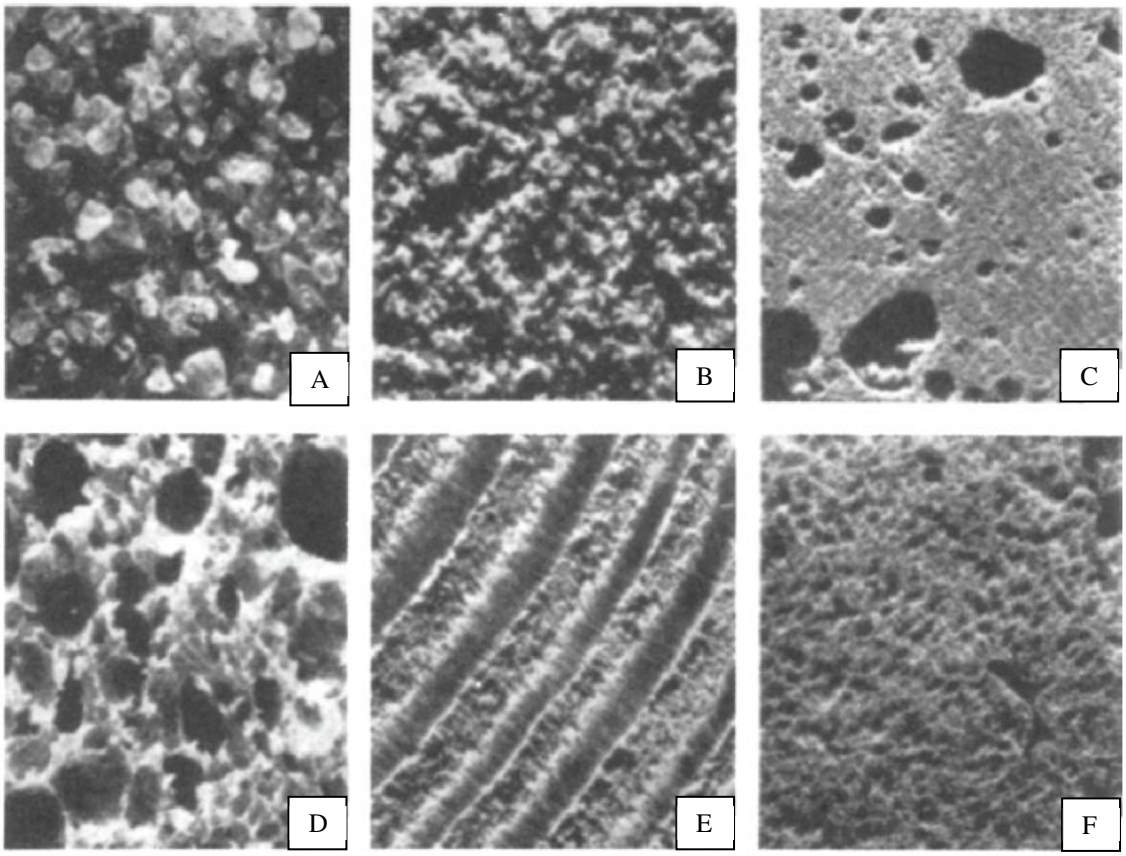

Figure 2.1: Examples of natural porous materials: (A) beach sand, (B) sandstone, (C) limestone; (D) bread slice, (E) wood and (F) human lung. [14]

The first parameter we introduce to describe a porous medium is porosity (φ) or void fraction. It's an intrinsic property of every porous material and is defined as the ratio between the volume of the pores and the total volume of the medium. [15]

$$\varphi = \frac{Void\ volume}{Total\ volume} \tag{2.1}$$

In this case, void space is generated by interconnected pores; however, when the pore network is not completely unified and some pore space is inaccessible from the fluid phase, is necessary to define an effective porosity. This parameter differs from

the first (bulk porosity) as it considers only the void space which contributes to the fluid flow inside the solid.

Being dimensionless, φ will always be lower than one; the closer is to zero, the higher is the volume filled by the solid matrix and the flow struggles to pass through.

As we have already seen in figure (2.1), porosity can be displayed in two different way: convex porosity and non-convex porosity (fig. 2.2). Non-convex porosity is typical of materials formed by stacking of granular particulate. It's usually displayed in natural materials assembled by progressive stacking of grains and particles of various form and size, such as sand or concrete. On the other hand, convex porosity is obtained by the formation of cavities inside the solid frame, forming sponge-like structures. These cavities can have a regular shape (usually it's spherical) or form passages of various shape inside the medium.

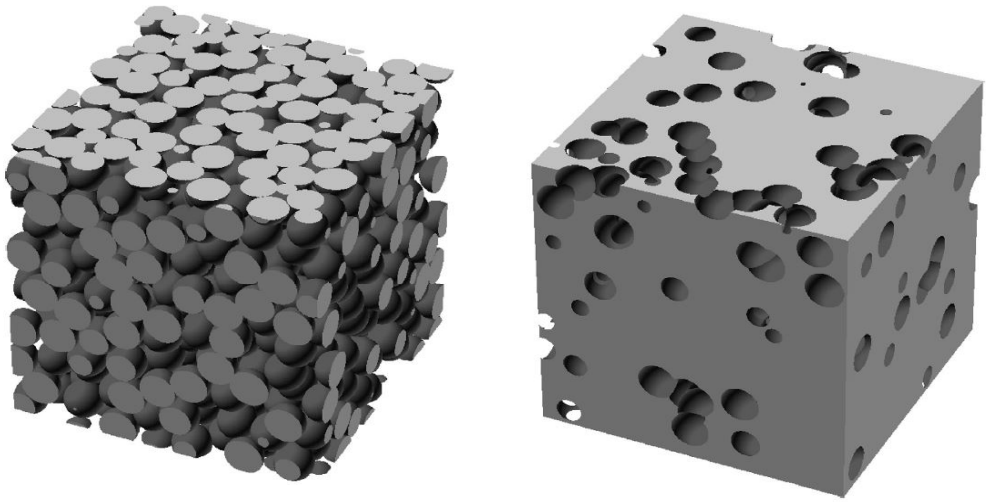

(a) (b)

Figure 2.2: Computer generated portions of porous media with (a) non-convex porosity and (b) convex porosity. Porosity is equal to 30% for both structures. [17]

Fluid phase inside the solid skeleton is obviously very dependent on the shape of the pores as not only porosity but also the morphology of the empty passages influences the flow path and the velocity field. It is easy to imagine that the fluid will slow down and dissipate more of its energy for materials associated with a low

value of φ, as a larger contact surface is offered, increasing the overall drag and pressure drop. (fig. 2.3)

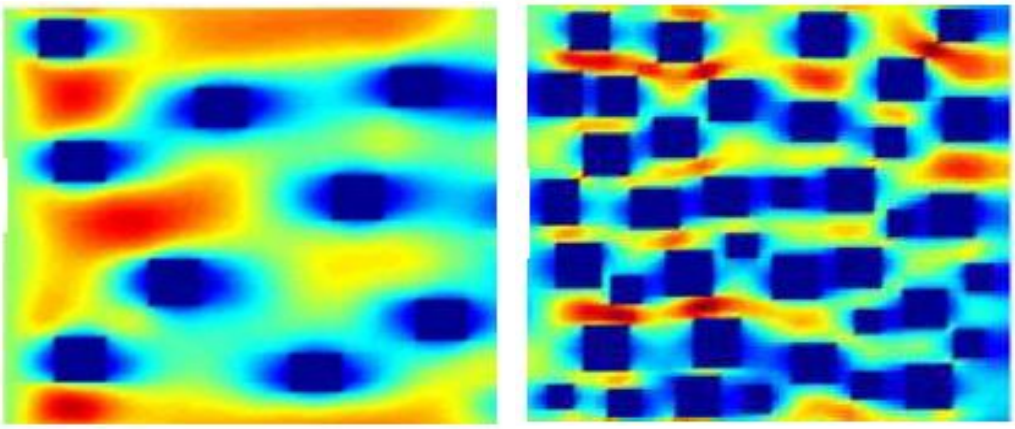

Figure 2.3: Velocity contours in 2D non-convex porous media. Porosity is 0.9 (left) and 0.67 (right). Red indicates high velocity, blue low velocity. [15]

For this reason, when dealing with non-convex porosity, is helpful to include an additional parameter which defines the irregularity of the granular particulate: sphericity. The sphericity of a particle Ψ is the ratio of the surface area of a sphere with the same volume as a given particle to the surface area of the particle and is expressed as: [11]

$$\Psi = \frac{A_s}{A_p} = \frac{\pi^{\frac{1}{3}}(6V_p)^{\frac{2}{3}}}{A_p} \tag{2.2}$$

where V_p is the volume of the particle and A_p its the surface area; A_s is the surface area of a sphere with the same volume as the given particle.

In the studies performed by Kerimov et al. (2018) [11], using digital generated porous media created via an algorithm of stacking of granular particles, it was proved how usually the lower is the average sphericity of the grains in a non-convex material, the lower is porosity.

Worthy of mention is also the effect on the permeability of the material; permeability *(k)* measures the resistance offered by a porous medium to be traversed by a fluid and it was introduced by Darcy (1856) in his self-named law, which will be reviewed in the next pages. Similarly to porosity, it was proved how irregularity in the grains' shape contributes to lower k, increasing the overall pressure drop. We present the results of the studies in figure 2.10:

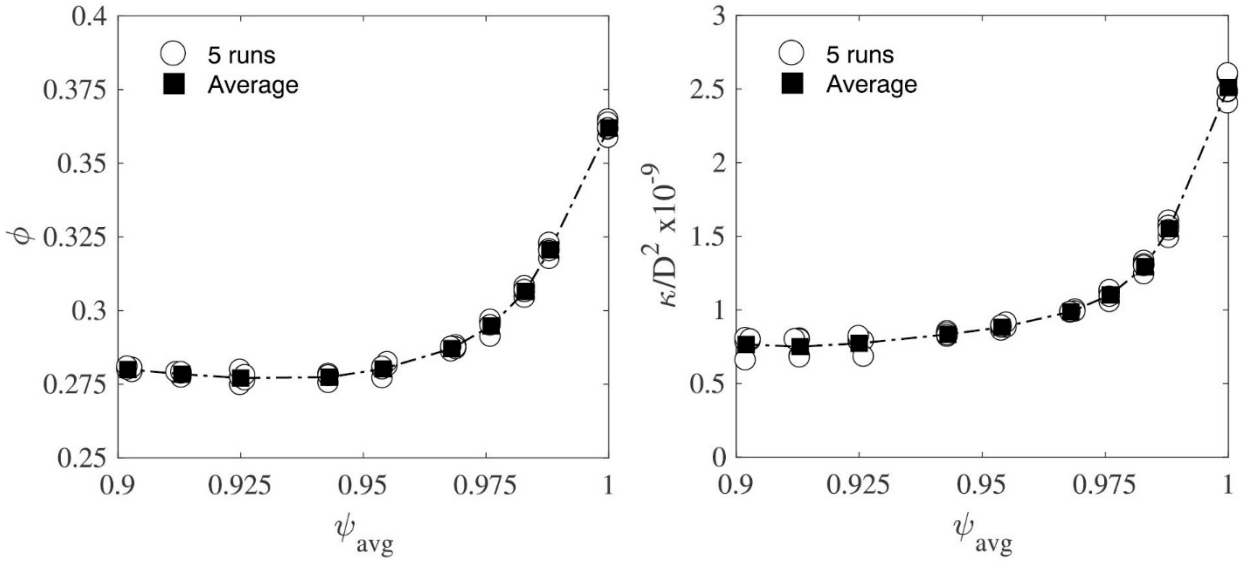

Figure 2.4: Porosity as a function of average sphericity (left), normalized permeability as a function of average sphericity (right); D is the diameter of the grain. [11]

To further predict the permeability of porous media, especially the one presenting convex cavities (Fig. 2.4b), Kozeny (1927) introduced the concept of tortuosity (τ). Initially, it was employed as a tuning parameter to better take into account the effects of the porous structure: the solid phase, deflecting the fluid, extends the route and τ corrects the effective flow path. Yet, later on, it started being used not only to quantify the complexity of internal percolation path but also to evaluate transport properties.

Now tortuosity has become a key factor for several engineering and scientific fields, such as geoscience, energy conversion and storage and chemical applications. As a result, this quantity is not uniquely defined and various evaluation approaches have been introduced from different contexts. In general, however, we can interpret its concept in two ways: (A) a geometrical measure to describe the sinuosity of the flow passages inside the solid skeleton; (B) a physical quantity indicating the resistance offered by the on a particular transport process inside the medium. As long as our field of interest will involve fluid-structure interaction and crack propagation due to the flow pressure, we will proceed to introduce only the geometrical and hydraulic definition of tortuosity, starting with the first.

Geometrical tortuosity (τ_g) is considered an intrinsic microstructural characteristic, as is independent of the particular transport problem considered.

Still, it's commonly used to replace physical formulations of tortuosity when their computation is overly complicated. We can define τ_g as the ratio of the effective length travelled by the fluid flow to the overall dimension of the medium in the macroscopic flow direction: [17]

$$\tau_g = \frac{L_{min}}{L} \tag{2.3}$$

Usually, L_{min} is associated with the shortest polygonal chain traversing the porous material, which is slightly shorter than the effective flow path L_h (or chemical length) as this one follows the track taken by the fluid. Alternatively, L_{min} can be replaced by the average of all the geometric path flow inside the medium. This average can be computed disregarding the difference in velocity for every track or conducting a flux-average instead.

As regards hydraulic tortuosity *(τ_h),* it was introduced by Carman (1937) to expand the studies on permeability carried previously by Kozeny. Similarly to the geometric tortuosity, τ_h is defined as the ratio of the effective hydraulic flow path L_h to the straight-line distance in the direction of movement. [17]

$$\tau_h = \frac{L_h}{L} \tag{2.4}$$

For this reason, hydraulic tortuosity can be read as a parameter describing the average stretching of the flow path in a porous material respect to a non-disrupted flow. The length L_h is usually measured from the streamlines in a condition of steady-state where the flow behaviour is unchanging with time. Still, identifying a streamline inside a porous frame remains not an easy task, as the random shape of its ever-changing cross-section, combined with the "continuous branching and rejoining" of its internal cavities, makes the process tangled. [17]

To solve this problem, some computation methods were proposed; for instance, Zhang and Knackstedt (1995) suggested to evaluate a weighted average of all the streamlines traversing the medium, using as weight the corresponding time requested for a single flow particle to move along its entire flow path.

We can reformulate (2.4) as the following:

$$\tau_h = \frac{1}{L}\left(\frac{\sum_i w_i l_i}{\sum_i w_i}\right) = \frac{1}{L}\left(\frac{\sum_i l_i\, t_i^{-1}}{\sum_i t_i^{-1}}\right) \tag{2.4}$$

where l_i, w_i and t_i are respectively the single streamline length, the related weight and the travel time for a particle. It was later proved by Matyka and Koza (2012) that equation (2.4) can be written using the instantaneous particle velocity v_i or its distribution *v(x,y,z)* obtaining:

$$\tau_h = \frac{\int_\Omega v d\Omega}{\int_\Omega v_x d\Omega} = \frac{\langle v \rangle}{\langle v_x \rangle} \tag{2.5}$$

with Ω being the porous domain saturated by the fluid. It is essential to note that equation (2.5) is based on two hypotheses: (1) fluid flows only in one direction without reentering in the material, and (2) the fluid is incompressible. These two assumptions are acceptable as long as the flow is laminar and associated with a low Reynolds number.

However, as we have already seen in the previous pages, a domain discretization is required if we want to approach numerically the computing of hydraulic tortuosity. The velocity field of the fluid is then defined assigning a value of v_x, v_y and v_z to each of the nodes composing the domain. In this way, we may reformulate equation (2.6) as the following [15]:

$$\tau_h = \frac{\Sigma_{i,j,k} \left| v_{ijk} \right|}{\Sigma_{i,j,k} \left| v_{x,ijk} \right|} \tag{2.6}$$

where x is the flow direction and $|v_{ijk}|$ indicates the velocity magnitude for the node *(i,j,k)* and $|v_{x,ijk}|$ only of the x-component.

Despite existing many other microstructural descriptors for porous media, such as pore size distribution and constrictivity, only the parameters already discussed will be employed for the later analysis. These alone, however, cannot help us to completely understand the phenomenon: mathematical models have to be introduced to further quantify how quantities evolve within the medium as time progresses.

2.2.2 Models adopted

Now that the main physical properties of porous media have been introduced, we will move on presenting the most relevant mathematical models developed to evaluate fluid flow inside porous media. These will be Darcy's law, Kozeny-Carman

equation and the poroelasticity theory proposed by Biot. Being these theories associated to a subject of interest relevant in many fields of study, multiple iterations and revisions have been made over the year, making it necessary to include in this review also the corrections that several studies have proposed to better assess the related phenomena.

Let us start with Darcy's law; it was proposed by Henry Darcy (1856) to estimate the pressure drop of a fluid flowing inside a porous medium in the absence of gravitational forces. It is derived from the Navier-Stokes equations, assuming the condition of incompressible and isothermal flow, volume-averaging its quantities. [18] From a mechanical point of view, the pressure of the fluid filtering through a porous medium is lost due to the fluid viscosity. We can express it in its differential form as:

$$\frac{dP}{dx} = -\frac{\mu}{k} \cdot U \tag{2.7a}$$

where P is the average fluid pressure, μ is the dynamic viscosity of the fluid, k the permeability of the porous material, U the average fluid velocity and x the direction of the flow. Alternatively (2.7a) can be reformulated using the volumetric flow rate Q and the cross-section of the material A, obtaining:

$$Q = -\frac{kA}{\mu}\left(\frac{dP}{dx}\right) \tag{2.7b}$$

which can be integrated over x obtaining:

$$Q = -\frac{kA}{\mu L}\Delta P \tag{2.7c}$$

where L is the length of the sample; $\Delta P/L$ becomes in this way the hydraulic pressure gradient across the solid frame.

It should be noted, however, that Darcy's model is suitable only for low values of Reynolds number; as Re increases, fluid velocity also rises, introducing non-linear effects to the problem. It has been proved now that this is caused by the inertia of the fluid, which greatly rises alongside its velocity. In this issue, Re still represents the ratio of inertial forces and viscous effects; for the cases explored here, however, it can be reformulated as the following:

$$Re = \frac{\rho U \boldsymbol{d}}{\mu} \tag{2.8a}$$

where ρ is the fluid density and $\boldsymbol{d}$ is the internal scale length of the medium (average channel width or average grain diameter [20]); yet, being this length a difficult parameter to estimate for highly disordered media, equation (2.8a) can be rewritten as: [19]

$$Re = \frac{\rho U \sqrt{k}}{\mu} \tag{2.8b}$$

where $\sqrt{k}$ is also called Brinkman length [20]. The correlation $\boldsymbol{d} \sim \boldsymbol{k}^2$ can be obtained from Poiseuille-Hagen equation [21], considering a fluid flow inside a cylindrical tube.

For Reynolds numbers typically higher than 0.5, equation (2.7a) is no longer valid, and a non-linear term must be introduced for the relationship to be corrected. Forchheimer proposed a correction to the formula capable of modelling "non-darcy" flows [22]:

$$\frac{dP}{dx} = -\frac{\mu}{\boldsymbol{k_f}} \cdot U - \beta \rho U^2 \tag{2.9}$$

where β $[m^{-1}]$ is the inertial coefficient (or beta-factor) and k_f the Forchheimer permeability, which is very close to k (for this reason, many authors tend to disregard the difference to simplify the model). Note that equation (2.9) still assumes a stationary flow; turbulent regimes in porous media exist, however they are rare in subsurface problems [19]. In the Forchheimer quadratic regime, fluid flow is dominated by inertia forces, as evidenced by high values of Reynolds number and flow's velocity. Between the Darcy and the Forchheimer regime, it was also observed a cubic transitional state where the inertial effects start to display, and Darcy's law becomes progressively inaccurate.

The coefficient β, similarly to permeability, is related to the morphology of the solid phase, including porosity, pore size and shape. Several correlations [29] have been proposed for β, each one associated with a particular type of medium. Ergun (1952) formula is probably the most famous as it has been used in many fields:

$$\beta = \frac{4.24 \times 10^4}{\varphi^{1.5} k^{0.5}} \tag{2.10}$$

where $[\beta]=m^{-1}$ and $[k]=mD$. This correlation is well suited for porous media formed by granular stackings and packed beds.

Veyskarami et al. (2016) proposed a different equation derived from numerical simulation of a pore network which involves even the tortuosity of the medium:

$$\beta = \frac{6.9031\times10^{-8}\tau^{0.6}}{\varphi^{0.1}k^{1.2404}} \tag{2.11}$$

where $[\beta]=cm^{-1}$ and $[k]=cm^2$. From equation (2.11) it can be seen how porous media with low values of porosity and permeability and high values of tortuosity tend to develop high beta-factors, increasing the effect of fluid inertia during Forchheimer regimes.

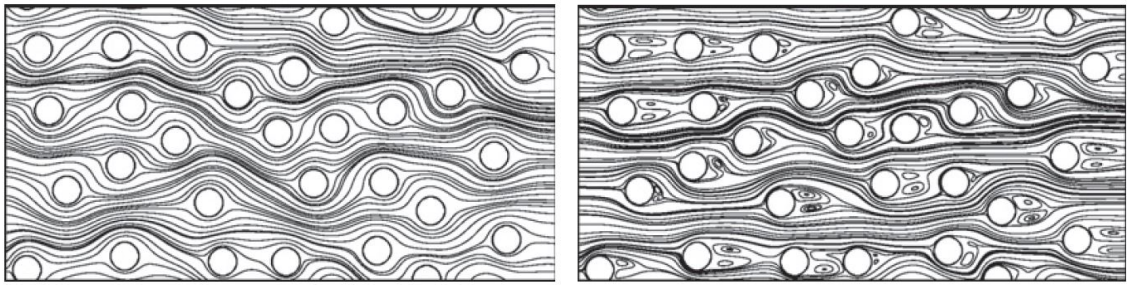

(a) (b)

Figure 2.5: Streamlines for different Re inside a porous media composed of cylinders. Darcy regime, Re=0.02 (a) and Forchheimer regime, Re=30 (b, note the presence of vortexes behind the cylinders and the more homogenous flow). [22]

From the equations previously presented, it is quite clear how the physical quantities associated with the solid phase influence the fluid flow inside its cavities. Still, it is impossible to derive a general constitutive equation capable of relating some of these quantities. This is probably caused by the huge morphological complexity characterizing porous media.

Some semi-empirical solutions have been presented, one of them being the Kozeny-Carman equation. This model developed initially by Kozeny (1927) and then expanded by Carman (1937) provides a relation between media properties and flow resistance in porous materials, linking together porosity and hydraulic tortuosity with permeability. [33]

Classical derivations for the Kozeny-Carman approach (e.g. [24]) start from the general Hagen-Poiseuille law combined with Darcy's average fluid velocity; permeability in the generic case is proven equal to:

$$k = K_{kc} R_h^2 \frac{\varphi}{\tau_h^2} \tag{2.12a}$$

K_{kc} is an empirical geometrical parameter assigned to pore shape and density, while R_h is the hydraulic radius assigned to the medium. It is defined as the ratio between the volume open to the flow and the overall wetted surface area; using the definition of porosity, this becomes:

$$R_h = \frac{\varphi}{S_v(1-\varphi)} \tag{2.12b}$$

where S_v is the specific internal surface area of the material, which is intrinsic to the porous material. Substituting (2.12b) in (2.12a) we obtain:

$$k = \frac{K_{kc}}{S_v^2 \tau_h^2} \left[\frac{\varphi^3}{(1-\varphi)^2} \right] \tag{2.13a}$$

that correlates the static properties of the medium (S_v and φ) with tortuosity and permeability which are fluid dependent. When the porous medium consists of packed spheres of diameter D_p, $S_v = 6/D_p$, $K_{kc} = 2$ and $\tau_h^2 \cong 25/12$ [25] resulting in:

$$k \cong \frac{D_p}{150} \left[\frac{\varphi^3}{(1-\varphi)^2} \right] \tag{2.13b}$$

It should be noted that equation (2.13a) has been derived assuming the fluid flow in the Darcy regime; moreover, specific surface area, tortuosity or grain size are parameters nonexistent in real porous samples, making the applicability of this equation only restricted to a quality-control tool for physical and digital experiments. Still, it can be applied to any typology of porous medium considering a homogenous and isotropic region of study. [34] Equation (2.13a) was further corrected during the years by different authors testing out its applicability; we will list some of these here below, joined by the relative comparison with the original one, confronting them with experimental data (fig, 2.6).

(a) $k \cong C_* \left[\frac{\varphi^{n+1}}{(1-\varphi)^n} \right]$ (b) $k \cong C_c \left[\frac{\varphi^m}{(1-\varphi)} \right]$ (2.14a-b)

Eq. (2.14a) [*Rodriguez et al.,* 2004] and eq. (2.14b) [*Mandelbrot,* 1983; *Sreenivasan,* 1991].

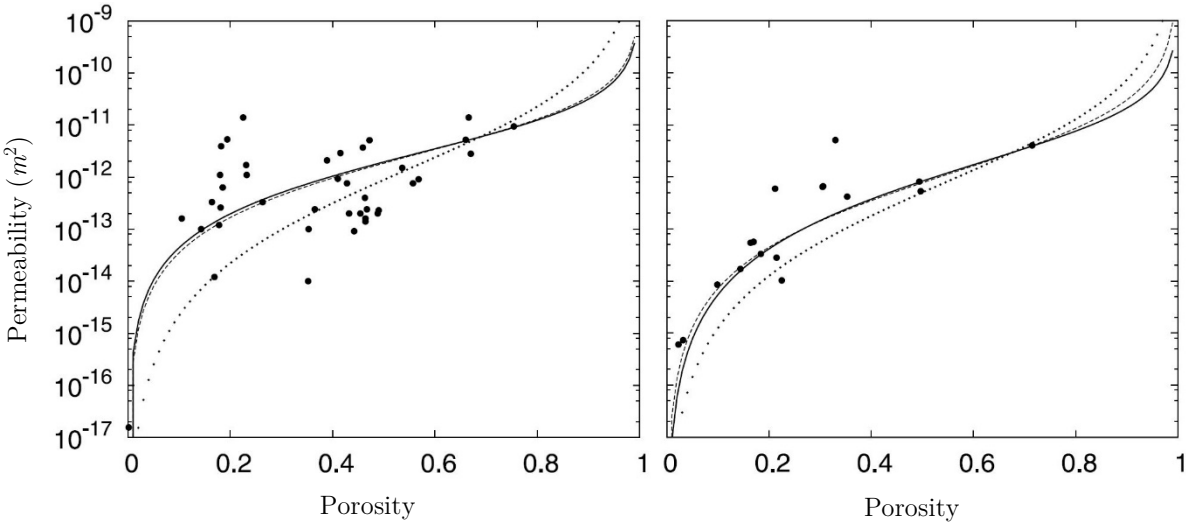

Figure 2.6: Permeability vs. porosity of a vesicular basalt, *Saar and Manga* [1999] (a) and natural eruptive material, *Melnik and Sparks* [2002]. Solid points represent measured values, dotted line eq. (2.13a), solid line eq. (2.14a), dashed line eq. (2.14b). [23]

Let us now at last take briefly into account the mechanical response of the porous media when fluid forces are applied inside of it. The presence of a fluid moving freely inside the cavities of the material modifies ultimately its characteristics.

There are two basics processes which carry out an essential function in the fluid-structure interaction: (1) internal pore pressure and (2) volume variations: an increase in pore pressure causes a dilation of the rock and compression of the solid induces a rise in pore pressure if the fluid is limited from leaving the domain. Indeed, when the compression of the porous skeleton persists, induced pore pressure rises and forces the medium to dissipate through fluid mass transport. This creates further deformation as the pores close and the solid progressively takes place. [26]

The first theory developed which took into account the effect of pore fluid on the deformation of the solid frame was Terzaghi (1923), who suggested a one-dimensional model for the problem of "consolidation". The method was then generalized further until Biot (1935) developed the linear theory of poroelasticity.

The Biot model is based on the assumption of a continuum solid skeleton traversed in its cavities by a moving fluid. When the solid is saturated with fluid (undrained condition) we can evaluate the stresses applied to the matrix by the fluid:

$$\sigma_i^{eff}=\sigma_i - \delta p \tag{2.15}$$

where σ_i is the total stress in the i direction, σ_i^{eff} the effective stress and p average fluid pore pressure combined with δ (Kronecker coefficient). Averaging the stress in a cubic unit, we obtain the average effective stress:

$$\sigma_{avg}^{eff}=\sigma_{avg} - p \tag{2.16}$$

note that equation (2.16) assumes an isotropic and homogenous response of the medium. According to equation (2.16), when the pore pressure gradually decreases, the fluid is withdrawn by the frame, leading to an increase in the average effective stress on the solid. Therefore, the frame is compressed, and void volume reduces.

These effects of stress and fluid pressure on porous media are often neglected as the matrix is regarded approximately as only slightly compressible; therefore, porosity is often assumed as a linear function of fluid pressure in porous media and permeability is generally looked as steady. Still, when large deformations occur and pore pressure collapses, non-linear effects can take hold and φ and k vary consequently. [27] We present two empirical relations proposed by Gorbunov (1973) that describes the non-linear evolution of these quantities:

$$\varphi(p)=\varphi_0 A_\varphi e^{\alpha_\varphi (p-p_0)} \tag{2.17a}$$

$$k(p)=k_0 A_k e^{\alpha_k (p-p_0)} \tag{2.17b}$$

where $A_\varphi, A_k, \alpha_\varphi, \alpha_k$ are empirical coefficients, φ_0, k_0 and p_0 are the initial values for porosity, permeability and pore pressure. [28]

Having properly overviewed now the object of our case of study, let us conclude this chapter introducing the processes and techniques that engage it.

2.3 Hydraulic fracturing

Hydraulic fracturing involves the breakup of a solid medium through the action of an injected fluid. It is usually employed to increase the permeability of sedimentary rocks overlying a reservoir of gas or oil using hydrodynamic forces; in this instance, the method is called 'fracking'. This procedure, applied to extraction areas, can greatly improve the recovery rate of raw material, effectively decreasing the cost connected to the operation. In this way, low or ultra-low permeability reservoirs can be accessed easily via the propagation of resources along with the micro or macro-fractures. The fluid itself is, in this case, composed of water and a viscoelastic additive, which thickens the liquid and facilitates penetration through the soil. To prevent the closing of the newly formed gap, a proppant (typically sand) is added to the mixture. [30],[34],[35],[36],[37]

2.3.1 Description of the process

The process is carried on by injecting an excessive amount of fluid inside a solid or porous substrate; this initiates a fracture inside the support or extends the pre-existing ones.

The investigation of the process was originally developed by applying the theory of poroelasticity to the solid media to describe the effects of volumetric opening for microcracks, fissures, and pores due to the flow. These results through the solid media are represented via pore pressure: in this manner, fluid movement and solid deformation occur simultaneously and affect each other.

Consider the representative volume element (RVE) of a porous support subjected by stresses along its transverse direction; its initial state is isotropic, homogeneous and elastic. It's punctuated by void spaces of different sizes like pores and fissures, which will be saturated by fluid injection. With the increase of the flowrate, pores will be elastically opened and the solid matrix fractured by pore pressure. [31]

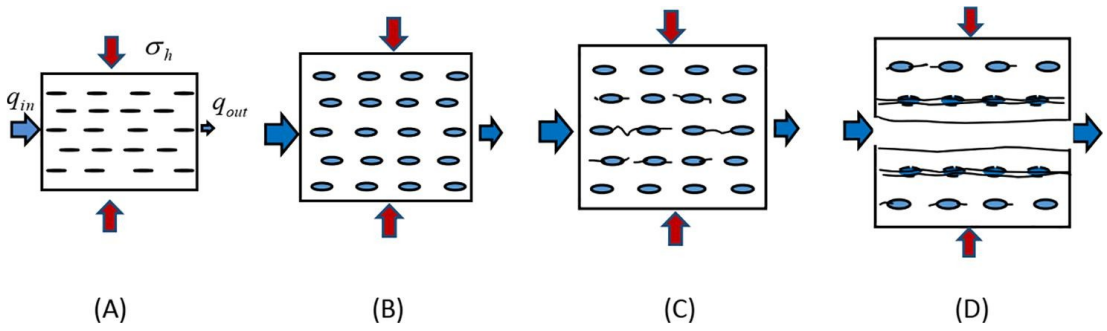

Figure 2.7: The process of hydraulic fracture. In this figure, σ_h represents the minimum compressive principle stress normal to the fracture, and q_{in} and q_{out} represent the flowrate in and out of the RVE, respectively. [31]

This process of hydraulic fracturing can be divided into three stages by four special states, which are:

(A) Initial compression state, where the solid is in compression state under the in-situ stresses. Pore stress is absent as the effective pore pressure is zero; the RVE is slightly deformed due to the compression applied along its transverse direction.

(B) Stress balanced state, where the fluid pressure inside the pores balances the in-situ stresses and cancels out completely every strains.

(C) Critical state, where the breakdown of the porous skeleton is about to occur; the strains almost exceed the value of critic strain separating micro to macrocracks propagation

(D) Fracture opening state, where the fluid pressure equals the compression state and cohesive stresses inside the solid cancels out, resulting in a incomplete or complete fracture.

Correspondingly, the three stages are:

Stage I, from (A) to (B), is the compression relieving stage: the compressive stress is balanced to zero with fluid injection. Stage II, from (B) to (C), is the elastically stretching stage: the solid is stretched to the critical state by the pore pressure. And stage III, from (C) to (D), is the cohesive breakdown stage: the cohesive stress gradually disappears due to the developing fracture and the pore pressure reaches to its minimum.

2.3.2 Types of numerical simulations adopted

Besides mathematical models, some practical experiments have been carried on to describe in-depth its general behaviour. However, for more modern techniques introduced in the fracking process that involve multistage or simultaneous fracturing, these types of solutions reveal themselves as inconclusive and unable to accommodate this new cracking system. This leaves out only numerical simulation as an efficient approach for the subject, allowing us to solve even the most complex situations if set correctly. [30],[31]

Being a coupled problem involving solid deformation and fracture with a liquid phase flowing inside, the numerical solution chosen is required to interface the two parts. This can be done in three different ways, using a continuous, discrete, or hybrid approach. [36]

The typical continuous approach is based on the finite element method; the presence of a developing crack geometry requires however a continuous re-meshing of the studied domain, causing a substantial increase in the computational time required. Moreover, mesh adaptation requires an intermediate 'balancing step' for the evolving field to ensure mass and momentum conservation between the changing elements. The FEM method must also be coupled with a cohesive zone model (XFEM); this enables to represent discontinuities inside the material, simulating successfully the propagation of the crack.

An alternative to XFEM based methods is phase field methods (PFM), which involve a scalar crack field representing intact and broken regions of the RVE. The crack path is then accounted by removing the elements caught up in the field.

As regards the discrete approaches, they are based on the discrete element method (DEM): particles of different sizes and shapes are assembled to represent the porous medium. The deformation of the solid is then rendered applying the displacement of the particle; internal forces are instead expressed by the contact between the points.

Finally, hybrid approaches aim to combine the advantages of the two types of models to quicken the simulation, attempting to maintain physical consistency over the time-steps.

In our case, the deformation and the breakage of the medium will be described implementing an approach comparable to the discrete element method.

2.3.3 Environmental impact

Despite the 'fracking' process will not be further investigated in detail by this research, a brief analysis of its environmental impact will be presented, given the relationship with the subject discussed.

The process of hydraulic fracturing applied to boreholes is considered highly controversial: the act of forcibly inject fluid underneath can lead to a plethora of dire outcomes if not designed properly. [32],[38]

Since its introduction in 1930, almost 2.5 million "frac jobs" had been performed worldwide and at first there were no regulations or procedures generally established to comply. The development of the first simplified models started only in the 1950s when Perkins and Kern proposed the so-called PK model. From then on, newer and more accurate solutions were discovered but still none of them took into account how impactful these methods were if not preceded by a detailed on-site examination. [39]

The situation was presented to the public only at the end of the previous decade when pollution concerns involving water contamination surfaced among reports of methane and diesel emissions, a tremendous waste of water, and induced seismicity.

At the moment, public debate is polarized between the industry lobby on the one hand and the environmental activists on the other, since the aforementioned studies that had been addressed have shown that risks depend mainly on the quality of the jobs surrounding the fracking process, rather than the process itself.

For what concerns the water contamination issue, EPA released in 2016 their final report surveying the subject: there is scientific evidence that hydraulic fracturing can threaten water reserves under certain conditions. These, however, largely depend on the grade of care applied to the task of handling the wastewater

or from the injection of fluid into wells with inadequate mechanical integrity; quoting directly from the report: "spills during the handling of hydraulic fracturing fluids", "injection of hydraulic fracturing fluids directly into groundwater resources" and "disposal or storage of hydraulic fracturing wastewater in unlined pits". It was however impossible to identify the severity of these impacts due to "data gaps and uncertainties" [32].

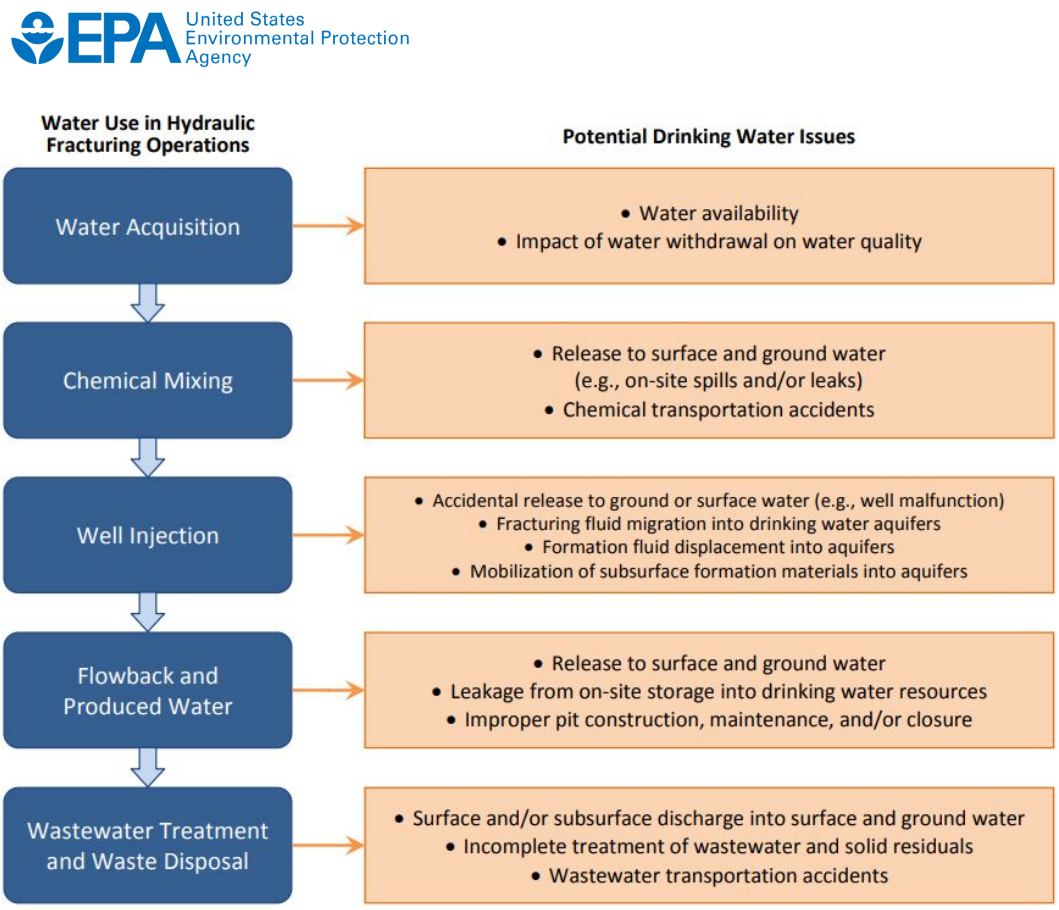

Figure 2.8: Water use and potential concern in hydraulic fracturing operations. [32]

A more seemingly conclusive outcome regards investigations led in Pennsylvania on the concentration of natural gases in shallow groundwater. It was possible to witness how for nearby active gas wells the concentration of CH_4 is significantly higher if compared to the data retrieved for inactive facilities (fig. 2.9). In particular, "methane concentrations were 17-times higher on average (19.2 mg CH_4 L^{-1}) in shallow wells from active drilling and extraction areas than in wells from nonactive areas (1.1 mg CH_4 L^{-1} on average)". Still, we note that there are no

data points for non-active wells within similar distances as the active ones; it is indeed shown by the authors how a greater amount of data would have helped to achieve a more definitive view on the case. [33]

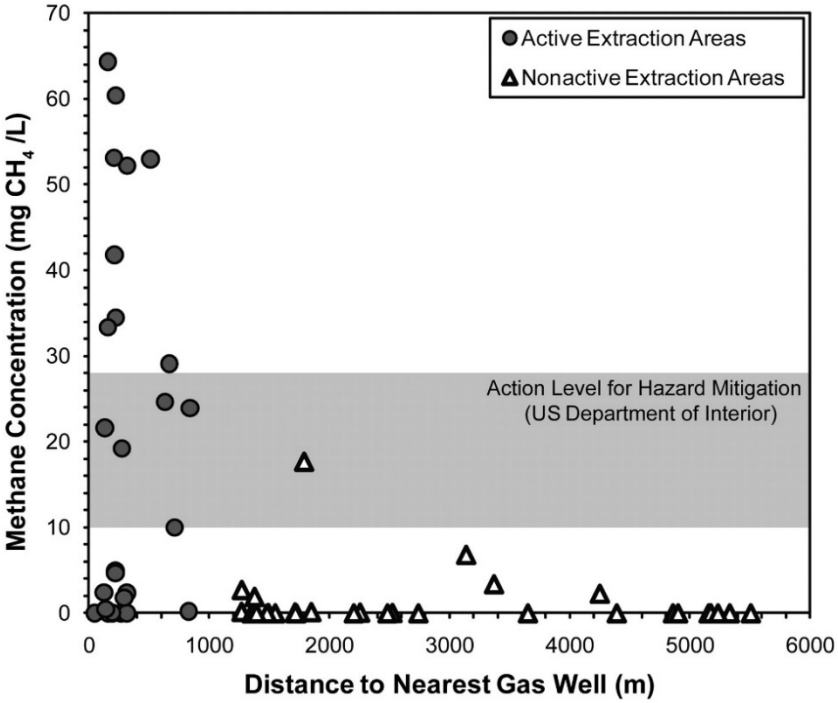

Figure 2.9: Methane concentrations (milligrams of CH_4 L^{-1}) as a function of distance to the nearest gas well from active (closed circles) and nonactive (open triangles) drilling areas. [33]

Nevertheless, all these studies settle on how more regulations are needed to ensure the sustainable future of hydraulic fracturing and gas extraction and to raise public trust in their employment.

Chapter conclusion

We have evaluated how the study of hydraulic fracturing affects several areas of research and how these subjects tend to couple with one another, causing a variety of complex phenomena difficult to approach singularly. In the past various possible solutions were tested to correctly model and simulate the process we discussed, still, none of them stood out for being the most effective: further research is required to properly understand the problem, specifically in the microscopic scale.

Therefore, having overviewed now the subject of our case of study, let us proceed and introduce the methodology we will follow to approach the matter.

Chapter 3

Methodology

The following pages will focus on the methods employed to describe a hydraulic fracturing problem applied to a porous medium. Firstly, a review of the basic numerical procedures adopted to solve a fluid-structure interaction problem will be presented. Navier-Stokes equations and their numerical solution will then follow. Given the laminarity of the fluid flowing inside the material, a direct numerical simulation will be employed. Computational approaches used to handle fluid-structure interface, solid deformations and breakage (immersed boundary methods and the peridynamic theory) will be then introduced.

3.1 FSI implementation

As it was already discussed before, in fluid-structure interaction problems, analytical solutions are almost unattainable as they usually depend on the case studied; thus, only numerical simulations remain employable. We will now proceed to review the basic characteristics surrounding them.

3.1.1 Numerical procedures

We can classify the numerical methods that solve fluid-structure interaction problems in two categories: the monolithic approach and the partitioned approach. [3] These approaches differ in the definition of the algorithm applied to solve the solid and fluid field, specifically in the way the two phases interface together (fig. 3.1).

In the monolithic approach (also called fully coupled), the solid and the fluid phase are managed together, and their dynamic is described using a single equation applied to the same mathematical framework. Fluid and solid are evolved simultaneously via a unified algorithm that includes the interface law between the phases. For this reason, the interfacial conditions are implicit in the procedure and

are solved concurrently at every time step. This strategy assures us a more optimized code, capable of improving the accuracy of the final solution; unfortunately, it also requires higher proficiency and more resources to develop it, given its more specialized nature. It's also limited to simple 2D problems given the higher stiffness of the solid matrix compared to the fluid one. Solid equations are indeed written in Lagrangian formulation, compared to the fluid ones that are written in Eulerian; this increases the order of magnitude of the structure matrix causing the strict conditions for its application [5].

On the other hand, the partitioned approach aims to separate the fluid and the solid equation, treating them as two different computational fields solved independently with their mesh and algorithm. Interfacial conditions are then added to allow communication exchange between the two phases. This allows resorting to the already existing codes or programs that have been already approved and tested in other FSI problems, reducing the overall development time. This procedure offers greater flexibility as it's possible to choose two separate solvers for the fluid and solid structure.

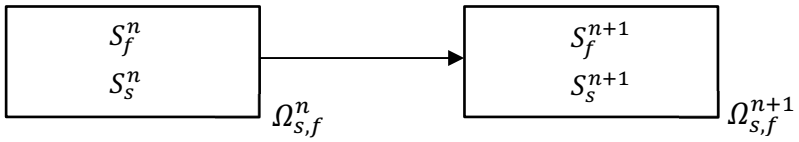

a) Monolithic approach

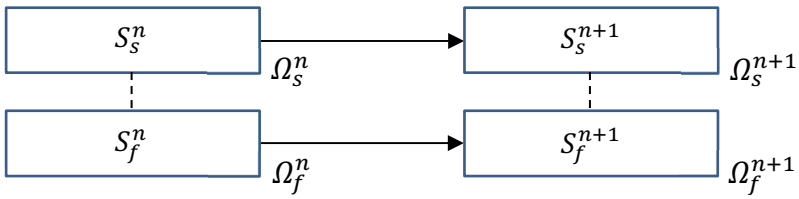

b) Partitioned approach

Figure 3.1: Schematic of the monolithic approach (a) and the partitioned approach (b) for fluid-structure interactions; S_s^* and S_f^* denote the fluid and structure solutions at different timesteps respectively. Ω^* indicates the mathematical framework at different timesteps and for the fluid, the solid or both together.

It is now clear how with this approach the focus moves to the designation of interfacial conditions, as fluid and solid are conceived as separated and need to interact with each other. As for most cases, the solid is expected to move throughout the fluid phase, we do not know a priori the interface location; hence it is required to implement in the code an interface tracking system capable of pinpoint the position of the solid and its quantities. For this reason, coupling errors and instabilities at the interface are some of the issues which affect the most in the accuracy of the simulation. Computational cost is also greatly increased as the use of coupled algorithms requires multiple sub-iterations in the single timestep.

Partitioned solvers carry out the coupling between the solid and fluid phase to completely map the pressure field over the studied domain. It usually demands the conservation of mass, energy and momentum; however, if no shockwaves are produced (the flow is incompressible) continuity and momentum equations are enough. The coupling is valid when the solution converges both in the structural and fluid domain; this will grant consistency for the quantities distribution, conservation of the physics and preservation of solid shapes.

In this case, the degree of coupling can be either loosely coupled or closely coupled, depending on how many times information is exchanged between the two solvers during sub-iterations (fig. 3.2). In loosely coupled models, interfacial operations are carried only at the end of the timestep; for this reason, convergence could only be partial, but this allows us to implement already tested and established solver packages, given their mutual independence. [4]

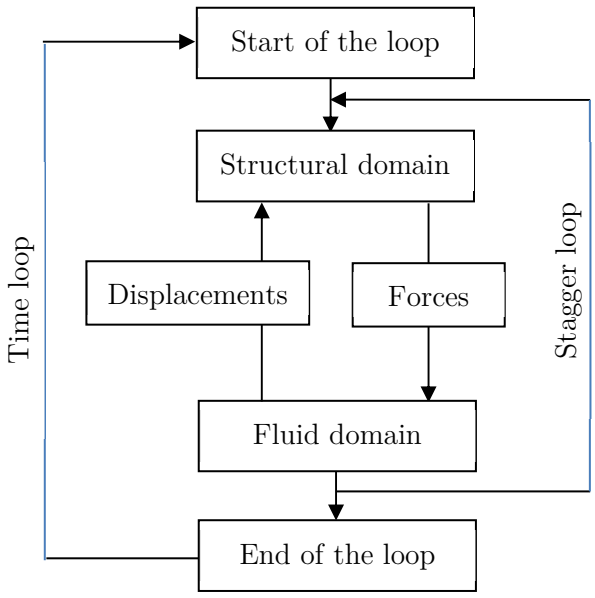

Figure 3.2: Schematic of partitioned solver employing for FSI simulation; for loosely coupled models, stagger loop and time loop coincide, as the convergence check is done once, at the end of the loop. For closely coupled models, the stagger loop is repeated till convergence is reached.

As regards closely coupled models, an interface module is introduced, ensuring that convergence is reciprocally reached between the two solvers at every timestep. At the interface, surface loads and displacement field are mapped from one grid to another, exchanging data at every inner iteration.

The process to solve the two coupled field could be resumed in the following way: [5]

1) Displacement field for the solid phase W_{s+1} is predicted at time t_{s+1} using the previous timestep t_n and mapped over the fluid grid.

2) Fluid grid is updated according to the predicted structure position; fluid equations are then solved in order to obtain pressure values P_{s+1} at time t_{s+1}.

3) Pressure field obtained by fluid solver is mapped over structural grid to get applied loads at t_{s+1}.

4) Structural solver uses these applied forces to get the corrected structural detection $W*_{s+1}$ at t_{s+1}, which is compared to the predicted one at (1).

5) If mutual convergence is achieved, the staggering loop ends and the time advances to its next step t_{n+1}=t_{s+1}; otherwise steps 2-4 are repeated.

When a sufficient number of sub-iterations have been completed, the simulation progresses to the next timestep. This minimizes the presence of coupling errors, rising greatly the computational cost in return.

Since this aspect is highly dependent on how the meshes are defined for the two distinct phases, it could be useful to examine the differences.

3.1.2 Treatment of meshes

Meshes are geometrical subdivisions generated to discretize the studied domain; this allows us to apply an algorithm capable of solving the corresponding field quantities. The main criteria employed to differentiate meshes is the space

regularity of their elements; we can distinguish two basic forms: the structured and the unstructured mesh.

Structured meshes are the most efficient in term of computational speed and convergence time. They are characterized by regular connectivity of their elements, expressing the area or volume domain as a 2D or 3D array, respectively. On the other hand, unstructured meshes are identified by non-constant connectivity and the use of irregular elements; this greatly simplifies the meshing process sacrificing, however, the overall efficiency of the grid. When the mesh is composed of a mixture of these two methods, it's called hybrid. (fig. 3.3) [6]

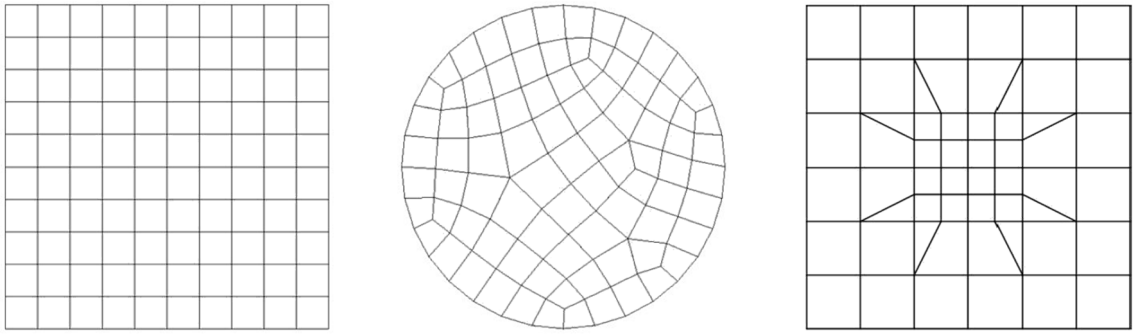

Figure 3.3: Two-dimensional structured (a), unstructured (b) and hybrid mesh (c). Note how in the unstructured quadrilateral mesh interior nodes are shared by varying numbers of elements. [6]

Another general classification influencing fluid-structure problems regards the employment of conforming or non-conforming meshes. A mesh is conforming if all the nodes and edges in the mesh are shared by each of their adjacent elements. [3]

A solution method which implements conforming meshes divides the computational domain into two parts: one occupied by the fluid, defined by the equations of Navier-Stokes, and one occupied by the solid matrix described by stress-strain equations. The interface between the solid and liquid phase is in this way, located along the shape of the mesh; this allows us to directly apply the boundary conditions to the nodes part of the interface. The most consequential downside of this approach resides in the necessity of updating the mesh at every timestep since the solid is subjected by the hydraulic stresses and the interface moves.

Therefore, if a moving interface is present, using a non-conforming method should be considered. This method treats the boundaries of the solid as constraints directly imposed on the model equation, employing an additional term which changes locally. Thus, the solid can freely move over the fluid domain with no re-meshing required whatsoever; as a result, fluid and solid equations are solved independently with their own grid.

The drawback of this approach is related to the perception by the fluid phase of the interface: as long as it isn't marked via mesh shape but only through an extra term in the fluid equation, the boundary loses definition, decreasing the accuracy in the flow representation near the border. Moreover, an interface detection algorithm must be implemented to track the interface throughout the timesteps, locating the nodes in proximity with the solid phase. Hence, to capture correctly the behaviour of the fluid, it's essential to set a higher level of resolution, reducing grid spacing. [3] We will further explore these considerations in the following chapters (in particular, see chapter 3.3 – Immersed boundary methods)

Besides, for grid-based methods, the mesh quality is defined by two fundamental parameters: the mesh aspect ratio and the skewness (fig. 3.4). Both rely on the shape of the grid and thus are related to the deformations that the solid phase is undergoing. Aspect ratio indicates the quality of the elements, as it's equal to the ratio of the shortest length of the element to the longest one. Skewness, on the contrary, defines element quality using its internal angles. When these parameters are ideal, convergence time is minimized, granting an overall increased accuracy. [7]

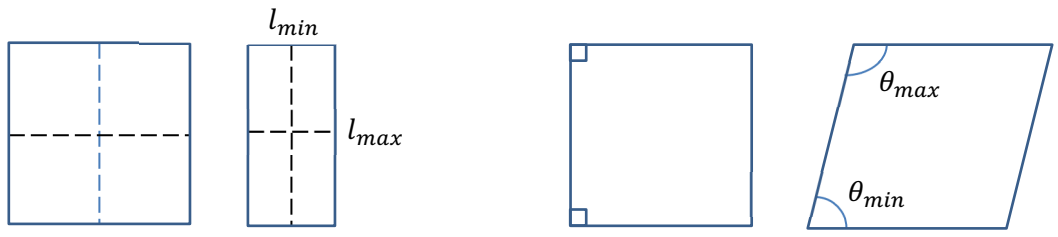

Figure 3.4: Two-dimensional quadrilateral elements undergoing aspect ratio (a) and skewness (b) deformations.

It now seems clear how meshing should not be considered an easy task, especially when the conditions of the problem we need to study appear to be complex. Not

meshing at all could potentially ease the subject, avoiding incurring in numerical problems later on.

The introduction of meshfree approaches tried to address the limitation mentioned above, both for the conforming and non-conforming meshes. They are based on the approximation of the solid or fluid domain using a particle distribution, which can be random or on a cartesian grid. These particles, also called nodes, interact with their neighbours exchanging forces and moving throughout the domain. As a result, the simulation itself becomes Lagrangian since it follows the velocity field of the particles. By eliminating the structure of the mesh, we can achieve better results in problems involving large deformations, crack propagation and intricate geometries; in these situations, it becomes very difficult to maintain connectivity between the elements and this can potentially lead to numerical errors. [4],[8]

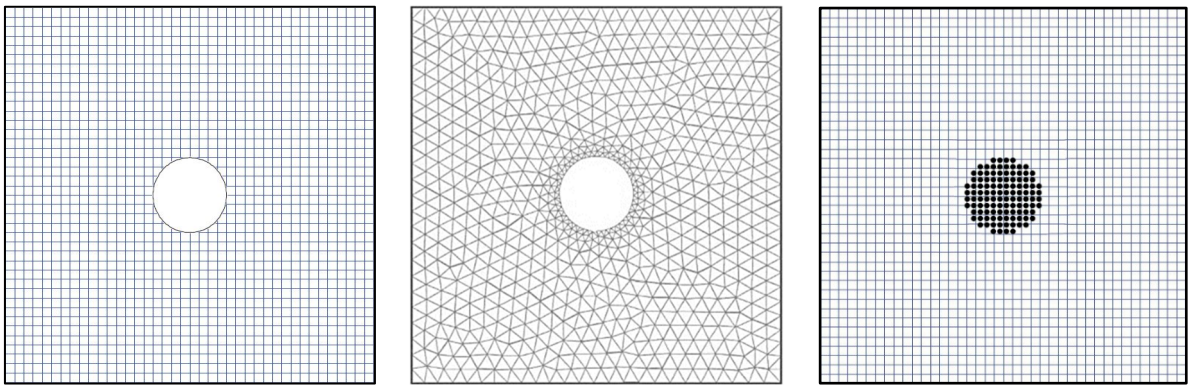

Figure 3.5: Two-dimensional conforming (a), non-conforming (b) and mesh-free configuration (for the solid phase) (c). [3]

Furthermore, it's possible to enhance the accuracy of the simulation by increasing the density of nodes; typically, these are in those areas which are subjected to the largest amount of stress. This kind of flexibility is not available in mesh-based methods and implementing an algorithm of mesh refinement is not always an easy task. On the other hand, employing a particle-based model greatly increases the computational effort required to run the algorithm, given that every single node must be tracked and interacts with its neighbours; a higher quantity of

nodes also must be used to achieve the same level of accuracy of mesh using simulations. [5]

Also, there aren't many software solutions capable of generating mesh-free configurations; their availability is very low and the necessity to develop a stable and efficient code is still present at the moment. [4]

The focus of every FSI analysis still lies however in the way interface is managed. Every exchange of information between the two phases such as applied loads, displacements and body interactions, takes place at the interface. It's handled differently depending on the method in use: in body-conforming meshes, we have already seen how interface motion has to be tracked to enforce the boundary conditions and transfer field quantities. It's also possible to implement a "composite grid"[9] (fig. 3.6a); in this approach, sub-meshes are overlapped to the main mesh in the areas close to the object's border. The sub-mesh, being defined in a separate local frame, can ease the enforcing of boundary conditions, however, the computational cost may increase since interpolations are needed to link the different meshes.

For non-conforming methods, the approach instead can be further characterized as cartesian and immersed boundary methods. The boundary is immersed in the background flow, and for this reason, it may cut the cell underneath. This can negatively alter the conservation through the border, affecting and lowering the fidelity of the simulation. The boundary topology is then represented through a process of cell interpolation: this spreads the solid edge over a few cell-width reducing the effect caused by the discretized domain. Errors on the fluid distribution can be large if the scale of the flow field evolutions is coupled with the scale of the smeared border.

Lastly, meshless-FSI implementation can be either meshed-meshfree or completely meshfree-meshfree. These formulations can be further classified by boundary conforming or non-conforming whether the node distribution follows the shape of the interface or not. The nodal cloud can also be regular or irregular if the points are arranged on a cartesian grid or randomly distributed, respectively (fig.3.6b). [5]

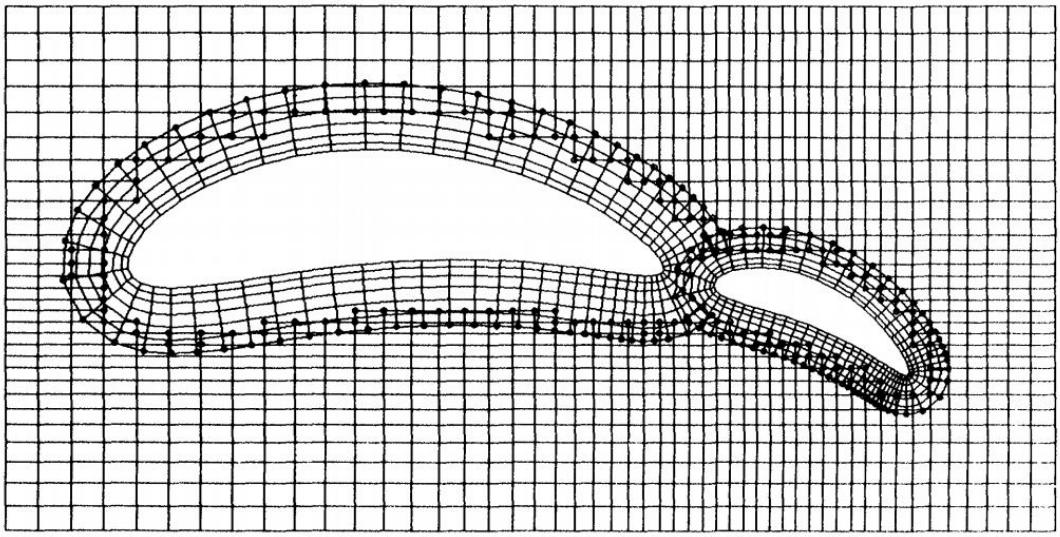

(a)

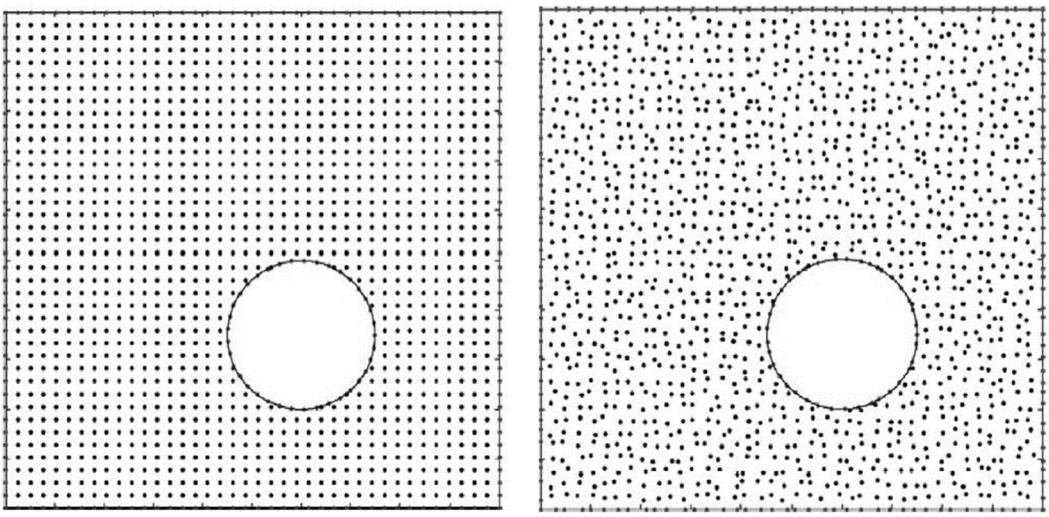

(b)

Figure 3.6: Two-dimensional conforming structured multigrid (a) and mesh-free regular and non-regular configuration (b). [9],[4]

Non-conforming meshes and its method attached will be further discussed in full in the following chapters, as, together with the mesh-free technique, they will be employed to face the problem presented. Let us now proceed exposing the core of the numerical analysis applied to the fluid phase that are Navier-Stokes equations.

3.2 Navier-Stokes equations

Computational fluid dynamic (CFD) is a branch of fluid dynamics which seeks to solve fluid motion through the use of algorithms and computational tools. Fluid motion is described by a set of differential equations that are called Navier-Stokes equations. These relations mathematically express the conservation of mass and momentum for a viscous fluid that evolves in time and space; usually, they can be complemented by an equation of state (energy balance equation) which link pressure, temperature and density together. We can write them as [40],[43]:

$$\frac{\partial \rho}{\partial t} = - \frac{\partial \rho u_j}{\partial x_j} \tag{3.1a}$$

$$\frac{\partial \rho u_i}{\partial t} = - \frac{\partial}{\partial x_j}\left(\rho u_i u_j + p\delta_{ij}\right) + \frac{\partial \sigma_{ij}}{\partial x_j} \tag{3.1b}$$

$$\frac{\partial \rho E}{\partial t} = - \frac{\partial}{\partial x_j}\left((\rho E + p) u_j\right) + \frac{\partial}{\partial x_j}\left(\lambda \frac{\partial T}{\partial x_j}\right) + \frac{\partial (\mu d_{ij} u_i)}{\partial x_j} \tag{3.1c}$$

where ρ indicates fluid density, p pressure, T temperature, $\{u_i\}_{i=1}^{3}$ the three velocity components, E total energy, λ mass diffusivity and μ fluid viscosity. We can also define d_{ij} as viscous stress tensor:

$$d_{ij} = \left(\frac{\partial u_i}{\partial x_j} + \frac{\partial u_j}{\partial x_i} - \frac{2}{3}\frac{\partial u_s}{\partial x_s}\right) \tag{3.2}$$

The set of equations (3.1a-c) consist of 5 equations in total and 7 variables; for this reason, they must be coupled with a constitutive model for both the fluid and the internal energy. However, if the fluid is compressible, then ρ, μ and λ can be considered constant and equations (3.1a-c) reduce in the following way:

$$\frac{\partial u_j}{\partial x_j} = 0 \tag{3.3a}$$

$$\frac{\partial u_i}{\partial t} = - u_j \frac{\partial u_i}{\partial x_j} + \frac{\partial p\delta_{ij}}{\partial x_j} + \frac{\mu}{\rho}\frac{\partial^2 u_i}{\partial x_i x_j} \tag{3.3b}$$

$$\frac{\partial T}{\partial t} + u_i \frac{\partial T}{\partial x_j} = \lambda \frac{\partial^2 T}{\partial x_i x_j} \tag{3.3c}$$

It is clear from equations (3.3a-b) that the model is already self-consistent and does not require the energy balance equation to be solved. We can rewrite (3.3a-b) in their non-dimensional form implementing the Reynolds number:

$$\frac{\partial u'_j}{\partial x'_j} = 0 \tag{3.4a}$$

$$\frac{\partial u'_i}{\partial t} = - \, u_j \frac{\partial u'_i}{\partial x'_j} + \frac{\partial p' \delta_{ij}}{\partial x'_j} + \frac{1}{Re} \frac{\partial^2 u'_i}{\partial x'_i x'_j} \tag{3.4b}$$

where the superscript (‘) indicates non-dimensional quantities. From equation (3.4b) it can be easily seen that the diffusive term is non-linear; for this reason, any convective flow is characterized by the non-linearity effect contained in the momentum equation. Hence, no analytical solution was found yet, and only numerical solutions are able to tackle the problem. As it was presented in the previous pages, a discretization of the fluid domain is requested and a resolutive method for equations (3.4) has to be specified. As long as the scope of interest of this study will focus only on incompressible fluid flows, given the low compressibility of a liquid fluid (e.g. water-based mixtures), the numerical methods explored will be described only taking into account this condition. Let us now present the basic numerical approach that will be applied to solve fluid motion.

3.2.1 Direct numerical simulation

The most intuitive approach for solving Navier-Stokes equations consists of discretizing the fluid domain and directly apply equations (3.4) without introducing any turbulence approximation to simplify the computing process. This method is called direct numerical simulation, as fluid equations are solved directly (Orzag, Steven A. 1970 [44]), unlike the turbulence-models based techniques. It is, for this reason, the most fundamental and precise simulation strategy; it requires, however, the highest computational workload for the causes that will be presented now.

Considering a generic fluid flow, turbulence manifests kinetic dissipation phenomena which can be described by a specific dimensional scale. This scale, usually identified as the Kolmogorov's scale, represents the fundamental dimension of eddy formation; because of that, the cell spacing of the mesh employed must be comparable to this dimension to correctly solve the fluid motion and represent turbulence structures. [40],[42],[43]

From Kolmogorov’s theory (1941), we can evaluate the kinetic energy dissipation rate ε as:

$$\varepsilon \propto \frac{U^3}{L} \tag{3.5}$$

where U is the velocity scale of the flow and L is scale length for larger turbulent structures. From ε we can denote Kolmogorov's scale η as:

$$\eta \propto \frac{\upsilon^3}{\varepsilon^{1/4}} \tag{3.6}$$

with υ the kinematic viscosity of the fluid.

Since the number of grid nodes along the generic direction x can be defined as $N_x = L/\Delta x$ and, as motivated above, $\Delta x \propto \eta$, we can determine the total number of nodes to properly solve the fluid domain:

$$N_p \propto N_x^3 \propto \left(\frac{L}{\eta}\right)^3 \propto \left(\frac{L^4 U^3}{L\upsilon^3}\right)^{3/4} \propto Re^{9/4} \tag{3.7}$$

If we introduce also the Kolmogorov's velocity scale as $u_\eta \propto (\upsilon\varepsilon)^{1/4}$ and the corresponding time scale $\tau_\eta \propto \eta / u_\eta \propto (\upsilon/\varepsilon)^{1/2}$ we obtain:

$$T_{tot} \propto N_p \cdot \frac{U}{L} \propto Re^{11/4} \approx Re^3 \tag{3.8}$$

T_{tot} indicates the total computational time for a generic fluid domain. It has been shown, however, how channel flow tend to deviate from this relation due to wall effects; the effective computational time changes to $Re^{3.4}$ [42], as it has been proved by the simulations performed in the past.

It is clear for this reason, that fluid regime and Reynolds number hugely influence the computational cost of a direct simulation. When Re rises, the flow tends to develop turbulent structures which dissipate kinetic energy at a scale level defined by K41 theory. The higher is Re and the higher are the number of nodes requested to correctly capture these eddies and solve the fluid.

However, as long as the case of interest will involve a laminar flow at low Reynolds numbers ($Re \approx$ 1-10), the applicability of a direct numerical simulation results more reasonable: inertia effects and vortexes formations, even if present, will be marginal and the dissipative phenomena minor.

As regards the computational process, let us evaluate briefly the typical approaches followed for solving incompressible flows. Observing equations (3.4), it

can be noted how pressure is not directly related to the fluid velocity, being defined by its constitutive law. It is, however, associated with velocity as a boundary condition, ensuring that the velocity field maintains its solenoidal property at every timestep. [41],[43]

This relation is also known as the Poisson's equation and can be written as:

$$\nabla^2 p' = -\nabla \cdot \boldsymbol{h}\,, \quad h_i = \frac{\partial u'_i u'_j}{\partial x'_j} \tag{3.9}$$

and it can be implemented into the solutions steps typically in two ways: pressure-correction or pressure-projection method.

As long as the pressure field influences instantaneously the velocity field due to the enforcement of mass conservation throughout the fluid domain, it is necessary for them to be solved together. This is impossible from a numerical point of view, as this coupling effect causes the algorithm to be implicit.

Pressure correction method provides a solution to this issue, dividing the integrational step into two sub-steps following a predictor-corrector approach logic. The first sub-step assumes a velocity field $u*$ on the basis of the current velocity and pressure field; a predicted pressure field is then computed via the Poisson's equation (3.9). The second sub-step then proceeds to correct the velocity field via the predicted pressure field $p*$; $p*$ is also updated consequently. [45]

Integrating equation (3.4b) we can summarize the method with the following steps (superscript (') is suppressed from now on to simplify the notation): [43]

1. Starting from the velocity and pressure field $\boldsymbol{u^n}$ and $\boldsymbol{p^n}$, we can compute the predicted velocity field:

$$u^* = u^n + \triangle t(\boldsymbol{C}^n + \boldsymbol{D}^n - \nabla p^n) \tag{3.10}$$

   where $\boldsymbol{C}^n$ and $\boldsymbol{D}^n$ are the convective and diffusive term in the integrated equation.

2. Pressure field is then predicted in the following way:

$$\nabla^2 p^* = \frac{\nabla \cdot u^*}{\triangle t} \tag{3.11}$$

3. Lastly, we can correct the velocity and pressure field u^{n+1} and p^{n+1} with:

$$u^{n+1} = u^n + \triangle t \nabla p^* \tag{3.12a}$$

$$p^{n+1} = p^n + p* \tag{3.12b}$$

Step 1 to 3 are repeated for every iteration performed.

Pressure projection algorithm is somewhat similar, as is too based on a prediction-correction logic. The velocity field $u*$ is however computed from u^n without imposing the pressure condition. A correction scalar field is determined instead, solving Poisson's law with $u*$; velocity field is then corrected through it and pressure is subsequently updated. Effectively the entire process consists of searching a velocity field that does not necessarily respect the solenoidal condition, only to adjust it later; the correction performed by the scalar field represents a projection of the field into the null divergence domain.

Let us now proceed evaluating the implementation of the fluid computing algorithm to the mesh grid.

3.3 Immersed boundary methods

The term "immersed boundary method" referred originally a numerical approach proposed by Peskin (1972) to describe anatomical phenomena regarding cardiac mechanics related to blood flow. In order to solve efficiently the complex geometry represented by the heart cavities, a structured non-conforming Cartesian grid was employed, and the flow equations were properly corrected to impose the effect of the boundary. [46]

This method potentially solves the rising complexity of most industrial applications, related to the presence of moving boundaries, intricated geometries and solid deformations. Regeneration and mesh warping are in this way prevented, as stated before. [50],[51]

3.3.1 Description of the method

Originally, simulation of fluid-structure interaction simulation was developed following the so-called Arbitrary Lagrangian-Eulerian (ALE), in which the mesh is

updated at every time step in order to ensure boundary application throughout the process and a precise interface resolution. As stated above, any ALE method has to be considered impractical, especially if the intention is to perform a DNS analysis which is already very resource-consuming.

Let us consider a solid body immersed in a fluid flow (fig. 3.7a). Conventionally a structured or non-structured conformal mesh is generated in two steps: first, a surface covering the boundaries of the grid is generated, then the interface nodes are employed to generate a mesh which covers the entire fluid domain, leaving out the solid body. In this way, the conformation of the mesh allows us to identify easily the appearance of the body, ensuring an effective application of the wall conditions.

Now let us evaluate the employment of a non-conformal Cartesian mesh (fig. 3.7b). In this case, it still exists a surface grid, as some nodes are positioned on the interface of the body. The Cartesian grid which covers the fluid domain, however, is generated without consideration on the surface of the body. In this manner, the solid body cuts through the grid elements, preventing traditional incorporation of the boundary conditions.

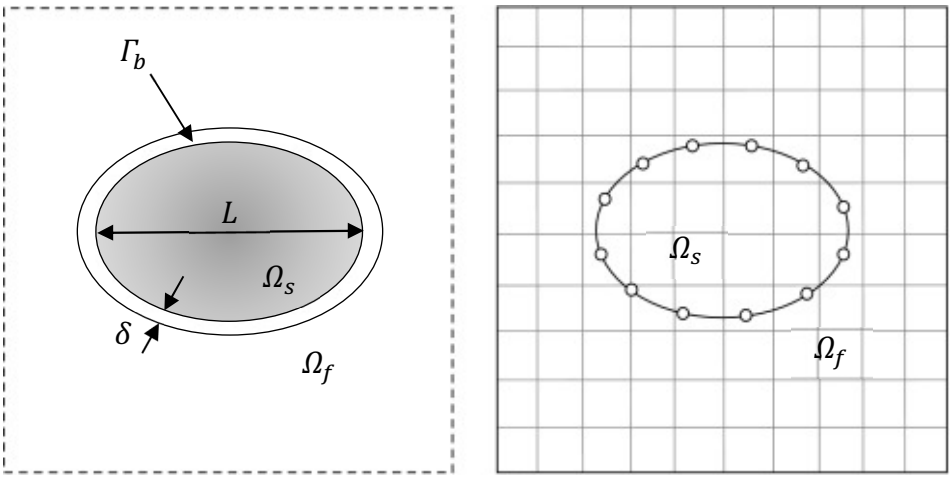

Figure 3.7: Generic solid body immersed in a fluid flow (a). The body is defined by its occupied volume Ω_s and surface Γ_b. Its characteristic length is L and δ is the thickness of the boundary layer. Schematic of body immersed in a cartesian grid (b). [46]

Due to this non-conformal nature of the mesh, the implementation of the wall conditions requires a local modification of the fluid flow equations. This allows us to recreate the effects of the solid surface on the fluid, using additional loadings in the vicinity of the boundary.

Yet, it should be noted that the imposition of the boundary conditions is not straightforward in an immersed boundary approach. Moreover, the consequences of this surface treatment should be considered, as accuracy and quantities conservation are not automatically assured. Also, the use of non-conformal structural meshes features an important downside that is the impossibility to control the grid resolution in the proximity of the body.

Indeed, it can be shown that the size of a Cartesian grid tends to rise faster than its corresponding traditional one, conformal to the body. Nevertheless, the computational cost could still be lower, as part of the nodes are inside the solid body, so fluid equations are not solved there. It was also mentioned before that structured grid requires less computational resources and converge faster to the solution, being grid transformation operations not necessary.

Still, the primary advantage of any immersed boundary method consists of the simplification of the grid generation algorithm. Usually, all body-conformal meshes require a formulation process which advances gradually and requires, for most of the time, further inputs and correction by the user. Re-meshing and mesh refinement are common operations performed when these type of space discretizations are employed. Moreover, the higher is the geometry complexity (curved profiles, intricate cavities and thin surfaces) the more tedious and iterative becomes the overall operation.

For example, structured grids are handled by decomposing the geometry volume into elementary subdomains: this approach reduces the complexity of the entire geometry, introducing however further computational steps; grid quality can also deteriorate due to interface incompatibilities. The use of unstructured grid can help, yet here, too, mesh quality can rapidly decrease with increasing morphological complexity.

On the other hand, when carrying out a simulation on a non-conformal mesh, the shape of the studied geometry does not seem to influence the quality of the

method, as grid quality and complexity are completely unaffected by its form. As also stated before, an advantage of the immersed boundary approaches reveals when dealing with moving boundaries: the grid, in this case, is stationary, ensuring simplicity and robustness to the solution strategy. [46]

Having properly discussed the features which characterize the current approach, let us proceed and review its implementation.

3.3.2 Numerical implementation

The original method introduced by Peskin was later improved by Uhlmann (2005), who proposed an efficient algorithm capable of effectively tackle FSI problems. The approach makes use of two superimposed different grids: a fixed uniform Eulerian grid which covers the entire fluid domain and a uniform Lagrangian grid attached to the moving body. Navier-Stokes equations are solved in the Eulerian grid, while Newton's laws are usually associated with the Lagrangian one.

The computing is carried on initially employing the Lagrangian force distribution. These are then applied to obtain the induced forces on the immersed particles; the computing requirement is based on the assumption that, on the surface of the body, the predicted velocity of the iterative scheme is equal to the local fluid velocity. It should be noted, however, that the two grid do not perfectly match and elements of the Eulerian grid overlap Lagrangian nodes; interpolation and force spreading are then required in order to properly manage force distribution between the meshes. [47]

Let us start with the implementation of the local boundary conditions since it's what distinguishes one method from another. Consider the application of non-dimensional Navier-Stokes equations (equations 3.4); the momentum equations is changed as the following:

$$\frac{\partial u'_i}{\partial t} = - u_j \frac{\partial u'_i}{\partial x'_j} + \frac{\partial p' \delta_{ij}}{\partial x'_j} + \frac{1}{Re} \frac{\partial^2 u'_i}{\partial x'_i x'_j} + f_i \tag{3.13}$$

f_i is the i-component of the forcing function (also called source term), which can be divided between momentum and pressure force. Equation (3.13) is solved for the entire fluid domain Ω_f, together with equation (3.4a). This approached is usually

defined as the "continuous force approach", as equation (3.13) is discretized and solved with the forcing function already incorporated. In the "discrete force approach" however, $\boldsymbol{f}$ is added after a preliminary discretization in which the velocity field is predicted and then corrected near the boundary surfaces. [46]

Let us evaluate briefly the solution steps followed by Uhlmann's approach, which belongs to the second class of methods described above. [47] The discrete (or direct-forcing) approach, is, in this case, embedded a pressure-correction scheme and solved with Crack-Nicholson algorithm. In the discrete form the scheme starts with:

$$\boldsymbol{u}^{*} = \boldsymbol{u}^{n} + \frac{\Delta t}{\rho_f}\left(-\nabla p^{\,\mathrm{n-1/2}} + \boldsymbol{RHS}^{\,\mathrm{n+1/2}}\right) \tag{3.14a}$$

where $\boldsymbol{u}^{*}$ is the first predicted velocity field, computed from the previous iteration $\boldsymbol{u}^{n}$; $\boldsymbol{RHS}$ stands for the right-hand side of integrated Navier-Stokes momentum equation. The source term $\boldsymbol{f}$ is then introduced in order to compute the first correction of the velocity field:

$$\boldsymbol{u}^{**} = \boldsymbol{u}^{*} + \Delta t \boldsymbol{f}^{\mathrm{n+1/2}} \tag{3.14b}$$

$\boldsymbol{u}^{**}$ is then employed to compute the pressure field for the correction sub-step:

$$\nabla^2 p^{*} = \frac{\rho_f}{\Delta t}\nabla \cdot \boldsymbol{u}^{**} \tag{3.14c}$$

The velocity and pressure field are ultimately corrected and updated in this fashion:

$$\boldsymbol{u}^{\mathrm{n+1}} = \boldsymbol{u}^{**} - \frac{\Delta t}{\rho_f}\nabla p^{*} \tag{3.14d}$$

$$p^{\,\mathrm{n+1}} = p^{\,\mathrm{n-1/2}} - p^{*} \tag{3.14e}$$

The source factor $\boldsymbol{f}$ in equation (3.14b) is computed via a three-steps process that involves information commuting between the two grids. The steps are the following: [47]

(1) *Interpolation* of the predicted velocity field $\boldsymbol{u}^{*}$ from the Eulerian to the Lagrangian field:

$$\boldsymbol{U}_l^{*} = \sum_{ijk} \boldsymbol{u}_{ijk}^{*} \delta_d\left(\boldsymbol{x}_{ijk} - \boldsymbol{X}_l^{n}\right)\Delta x \Delta y \Delta z \tag{3.15a}$$

where $\boldsymbol{U}_l^*$ is the predicted velocity of the Lagrangian node l, $\boldsymbol{x}_{ijk}$ are the node Eulerian coordinates, $\boldsymbol{X}_l^n$ the Lagrangian ones at the current timestep and δ_d the Dirac's delta function (fig. 3.8).

The regularized Dirac delta function proposed by Roma *et al.* [52] is defined in the following way:

$$\delta_d\,(x\text{-}x_o) = \delta_d^*\,(x\text{-}x_o)\;\delta_d^*\,(y\text{-}y_o)\;\delta_d^*\,(z\text{-}z_o)$$

$$\delta_d^*\,(s\text{-}s_o) = \frac{1}{h}\,\Phi\left(\frac{s\text{-}s_o}{h}\right) \quad , \quad \text{where } h \text{ is the Eulerian grid spacing.}$$

$$\Phi(t) = \begin{cases} \frac{1}{3}\left(1+\sqrt{1-3t^2}\right), & t \le 0.5, \\ \frac{1}{6}\left(5-3|t|-\sqrt{1-3(1-|t|)^2}\right), & 0.5 < |t| \le 1.5, \\ 0, & |t| > 1.5. \end{cases}$$

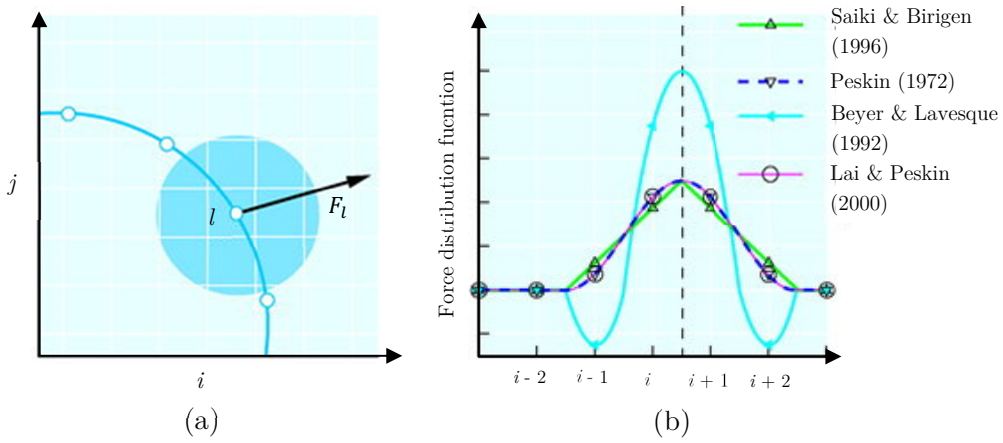

Figure 3.8: (a) Transfer of forcing F_l from Lagrangian boundary point X_l to surrounding Eulerian fluid nodes (shaded region signifies the extent of the force distribution). (b) Distribution functions employed in various studies. [46]

(2) *Computation* of the forcing term on the Lagrangian grid:

$$\boldsymbol{F}_l^{n+1/2} = \frac{\boldsymbol{U}_P(\boldsymbol{X}_l^n)\text{-}\boldsymbol{U}_l^*}{\Delta t} \tag{3.15b}$$

where $\boldsymbol{U}_P(\boldsymbol{X}_l^n)$ is the particle velocity associated to the Lagrangian coordinates $\boldsymbol{X}_l^n$ at the current timestep.

(3) *Spreading* of the Lagrangian force to the Eulerian grid:

$$\boldsymbol{f}_l^{n+1/2} = \sum_l \boldsymbol{F}_l^{n+1/2} \delta_d(\boldsymbol{x}_{ijk} - \boldsymbol{X}_l^n) \Delta V_l \tag{3.15c}$$

where ΔV_l is the volume of Lagrangian grid cells.

Steps (3.15a-c) are executed immediately after equation (3.14a) in order to compute the value of the source term for equation (3.14b).

It should be noted also that, to increase computational efficiency, the forcing process is not applied to the interior nodes of the solid particles, but only to the ones located at the solid-fluid interface. The generation process employed for creating the Lagrangian nodes could vary. [47]

The Dirac delta function, introduced in equation (3.15a), ensures that the total fluid force and the action of the particles applied onto each other are preserved during interpolation and spreading. This is effective however only when the Eulerian grid spacing is uniform in every coordinate direction (Peskin, 2002).

As already stated before, Eulerian grids are based on a Cartesian grid so every cell has to be considered cubical ($\Delta x = \Delta y = \Delta z$). Moreover, since the Lagrangian and the Eulerian grid are related in order to guarantee an efficient information exchange between the two, it is optimal for their resolution to match each other. In a similar fashion, even the Lagrangian cells have to be considered equally spaced and nodes distribution must be as uniform as possible.

So, summarizing, the volume ΔV_l of the Lagrangian grid must respect the following requirements: (1) ΔV_l should be as close as possible to Δx^3, (2) the number of Lagrangian point distributed over the body surface should be integer, (3) the radial thickness of the Lagrangian grid should be equal to Δx.

If these conditions are ensured, the particles interface is smoothed from the fluid point of view; this also provides an additional advantage for suppressing high-frequency fluctuations of the force values acting on the solid body. During the interpolation process, oscillations can generate from variations in the predicted velocity, especially when the Lagrangian grid moves and changes its orientation relative to the Eulerian grid. Breugem [47] dubbed this phenomenon as *grid locking*, given the dependency on the wavelength of the oscillations; if the dimensions of the Eulerian grid cells is comparable to the fluctuation's wavelength, then the overall effect is amplified. The use of the Dirac delta function can help decrease these

spurious variations: Uhlmann [53] showed that setting Dirac delta width of $3\Delta x$ is effective in suppressing the phenomenon while keeping the smoothing area compact and localized.

Peskin noted, however, how usually the velocity field near the solid boundary presents a jump along the normal direction of the wall due to the presence of the solid phase. This irregularity in the field proves to be troublesome when interpolating the velocity as the accuracy of the solution decreases. This is a significant downside of the smoothing process which cannot be corrected unless we resort to a sharp representation of the interface [50], which is equally undesired as it will probably amplify grid locking. [47]

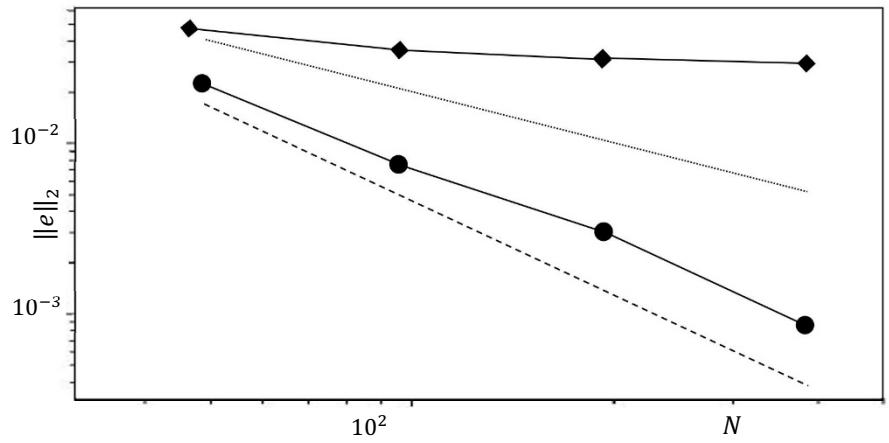

Figure 3.9: L2-norm error of the axial velocity component vs number of grid points; circles, linear interpolation process; squares, stepwise (sharp) geometry. Dashed line: 2nd order trend; dotted line 1st order trend. [50]

In figure (3.9) we can indeed observe how the norm error computed employing the linear interpolation method decrease faster than the 1st order slope, almost reaching a 2nd order trend. For this reason, a stepwise geometry representation is not recommended. The results are not so surprising, as any linear interpolation is usually accurate to second order. [50] Breugem proposed some procedural corrections which can increase the overall accuracy; they will be explored in the following pages as a conclusion of the presented subject (chap. 3.3.3).

Finally, let us complete the numerical overview of the method reporting the generical relations followed by the solid phase; the motion of a rigid body immersed in a fluid is described by Newton-Euler equations [48] as they express its translational and rotational equilibrium over time.

$$[M]\frac{dU}{dt} = F^{ext}\ , \quad U = \frac{dX}{dt} \tag{3.16a}$$

$$[I]\frac{d\omega}{dt} = M^{ext}\ , \quad \omega = \frac{d\Theta}{dt} \tag{3.16b}$$

where U and X are the velocity and position of the barycenter of the body, ω and Θ its angular velocity and position; M and I are the mass and the moment of inertia tensor of the entire immersed body. Equations (3.16a-b) and the modified Navier-Stokes equations form a system of differential equations which are coupled around the interface of the solid particles, ensuring the condition of no-slip and no-penetration on the fluid flow:

$$\boldsymbol{u} = \boldsymbol{U}_p(\boldsymbol{X}), \qquad \forall \boldsymbol{X} \in \Gamma_b \tag{3.17}$$

Newton-Euler implementation will not be furtherly explored as solid mechanics will be then taken into account by the peridynamics theory (chap. 3.3).

3.3.3 Improvements of the method

As stated before, field irregularity at the solid border tends to decrease the overall accuracy of the solution, as multiple effects, such as grid locking, overlapping of the Eulerian and Lagrangian grid and interface representation, influence negatively the interpolation and spreading processes. To mitigate this effect, different improvements to the original method have been proposed; we will proceed to report two of these improvements: the *multidirect forcing* scheme and the *inward retraction* of the Lagrangian grid.

- *Multidirect forcing scheme:*

The first consequence encountered when using a regularized delta function for interpolation and spreading operation lies in the generation of a diffuse distribution of the IBM force around the solid interface. As long as delta functions have a finite range of application, forcing loads are spread within a radius defined by the amplitude that has been set. This could form overlap areas between the nearby Lagrangian nodes which are distributed around the body surface. Figure (3.4a) illustrates the force distribution on the Eulerian nodes that are involved in the forcing operation; the two circles show the range associated with the delta functions applied to the two interfacial Lagrangian nodes. This would ultimately mean that

the velocity forcing at one Lagrangian grid point is perturbed by the forcing needed to determine the velocity of its next one. As a consequence, the distribution of the force could be inaccurate, leading to potentially bad velocity enforcement.

The solution proposed by Luo (2007) and Kriebitzsch (2009) consists of determining iteratively the forcing loads that enforce the considered Lagrangian node; their collective action is then combined to ensure that $U^{**} \approx U_p$. In this way, the source factor $\boldsymbol{f}$ is computed iteratively, integrating a loop between the steps (3.14b) and (3.14c), immediately after the steps (3.15a-c):

$$\boldsymbol{U}_l^{**,\,s\text{-}1} = \sum_{ijk} u_{ijk}^{**,s\text{-}1}\, \delta_d(\boldsymbol{x}_{ijk}\text{-}\boldsymbol{X}_l^n)\Delta x \Delta y \Delta z \tag{3.18a}$$

$$\boldsymbol{F}_l^{\,n+1/2,\,s} = \boldsymbol{F}_l^{\,n+1/2,\,s\text{-}1} + \frac{\boldsymbol{U}_P(\boldsymbol{X}_l^n)\text{-}\boldsymbol{U}_l^{**,s\text{-}1}}{\Delta t} \tag{3.18b}$$

$$\boldsymbol{f}_l^{\,n+1/2,\,s} = \sum_l \boldsymbol{F}_l^{\,n+1/2,\,s}\, \delta_d(\boldsymbol{x}_{ijk}\text{-}\boldsymbol{X}_l^{\,n})\Delta V_l \tag{3.18c}$$

$$\boldsymbol{u}^{**,\,s} = \boldsymbol{u}^{*} + \Delta t \boldsymbol{f}_l^{\,n+1/2,\,s} \tag{3.18d}$$

where the index $s \in [1{:}N_s]$ and N_s is the total number of forcing iterations and can be set at will. [47] Obviously, the higher is the number of iterations the higher is the accuracy granted by the process, but at the same time, the computational efficiency decreases. It can be seen that steps (3.18a-c) are analogous to the steps (3.15a-c) presented before; this is because the cycle still follows the *interpolation-computation-spreading* scheme that has been previously reviewed.

- *Inward retraction of the Lagrangian grid:*

The second consequence related to the use of the regularized delta function is associated with misperception by the fluid of the solid outer surface. The solid interface is perceived as a porous thin shell: this surrounding envelope has an apparent width dependent on the radius chosen for the Dirac function. (fig. 3.4b).

This clearly affects the fluid flow since the volume of the immersed body is perceived slightly bigger, introducing in this way, an additional drag. It has been proved, however, that a laminar flow close to a porous wall tends to decrease the overall drag. Still, the predominant effect is the former, so, when the Lagrangian grid is generated and the effective solid border is subtly scaled up, we need to compensate by retracting towards the interior the entire grid.

As long as the perceived width of the body scales with the width of the delta function, so should scale the optimal retraction distance. Usually, this width is associated with the grid spacing $\triangle x$; this means that in the limit of $\triangle x \to 0$ the retraction becomes zero as Dirac radius is also null. The optimal retraction distance is determined from simulations, by comparing the expected drag force to the one obtained.

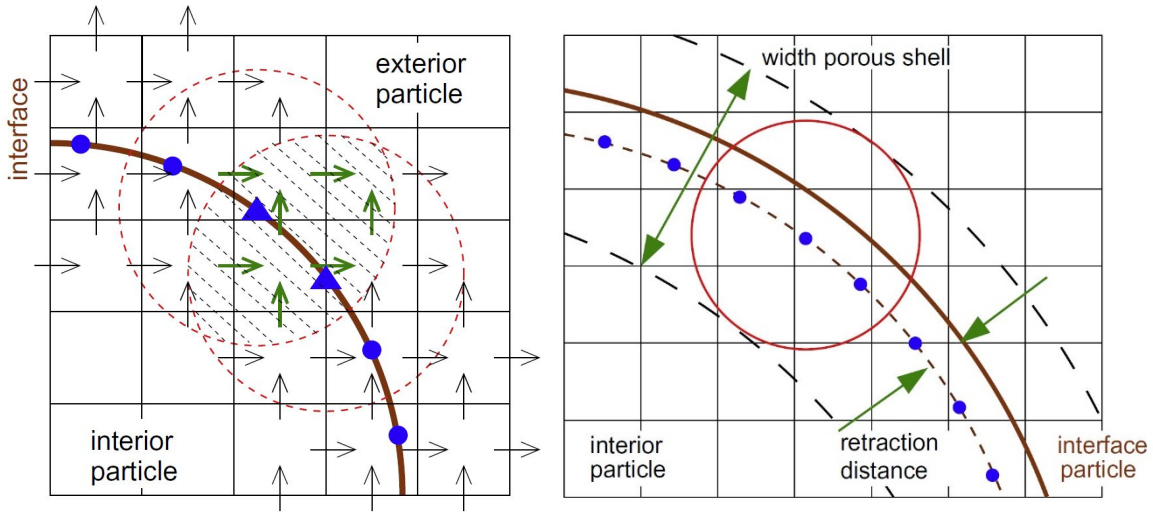

Figure 3.10: (a) Illustration of the diffuse distribution of the IBM force around the interface of a particle. Lagrangian grid points are indicated with dots; the arrows indicate the force distribution over the Eulerian nodes. The circles identify the Dirac delta's range applied to the Lagrangian points designated by triangles. (b) Illustration of the shell surrounding a solid particle. Retracted Lagrangian grid points are indicated with dots; the solid line defines the effective interface position. The circle describes the area of influence of the regularized Dirac delta function. [47]

Effects of both *multidirect* scheme and inward grid retraction are presented in figure (3.10), when applied to a single immersed sphere of diameter D. [47]

To conclude the numerical review of the method, let us report the minimum timestep derived by Wessling (2001) to ensure computational stability. For a third order Runge-Kutta integration scheme coupled with the central-differencing scheme, Von Neumann stability criterion gives:

$$\triangle t_{\min} \leq min\left(\frac{1.65}{12}\frac{\triangle x^2}{\upsilon}, \frac{\sqrt{3}\triangle x}{\sum_{i=1}^{3}|u_i^q|}\right) \tag{3.19}$$

It should also be noted that NS equations are advanced in time from one timestep to the next one knowing the particles velocities and positions at the current

timestep. This process is indicated as *fully explicit* coupling of the Navier-Stokes and Newton-Euler equations [47]; Hu (2001) pointed out that this coupling could potentially cause numerical instabilities when the solid-fluid density ratio reaches values lower than 1. This event, however, will not be a problem for us, as the scope of our research will involve density ratios $\rho_s / \rho_f > 1$.

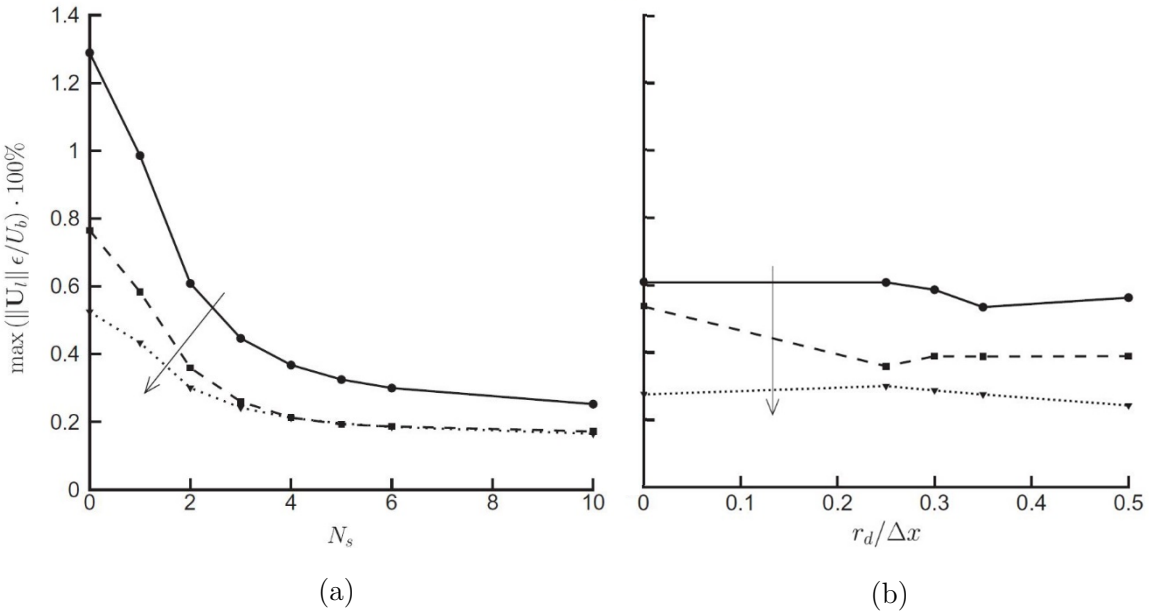

(a) (b)

Figure 3.11: (a) Plot of the maximum error in the norm of the Lagrangian velocity $\boldsymbol{U}_l$ as a function of the number of force iterations $\boldsymbol{N_s}$;the retraction distance is maintained constant. (b) Plot of the maximum error in the norm of the Lagrangian velocity $\boldsymbol{U}_l$ as a function of non-dimensional retraction distance $\boldsymbol{r_d/\Delta x}$; the number of force iterations is maintained constant. The error is given in percentage of the velocity of the body mass centre $\boldsymbol{U}_b$. Grid resolution is gradually increased: solid line, D/Δx=16; dashed line, D/Δx=24; dotted line, D/Δx=36. [47]

3.4 Peridynamics

Classical continuum mechanics, despite being effective for dealing with the physics of most of the solid materials, will always be incapable of modelling damage and fracture phenomena. The main obstacle is related to the mathematical definition of the theory, as it assumes that when a solid undergoes deformations, it remains continuous. In this way, when a discontinuity arises, the spatial derivatives which formulate the model become meaningless and are unable to describe the singularity that has been generated. [55],[56]

In chapter 2.3.2 we reviewed some employed numerical methods which have been implemented in order to describe the crack propagation. However, being these usually based on the continuum mechanics, they still inherit the difficulty of modelling fractures and large deformations. They also require the presence of a pre-determined crack geometry that initiates the phenomenon, together with additional relations that describe its propagation in velocity and direction. [55]

These restrictions were recently overcome by Silling (2000) introducing the non-local theory of peridynamics; the equations of motion are rearranged introducing an integral operator into the relation. This guarantees that the equations remain valid even when a discontinuity emerges in the solid. Moreover, since the level of damage of the material is controlled by the response described by peridynamics relations, fracture and crack events are spontaneous and do not require additional numerical techniques any longer.

Let us begin our review of the peridynamics theory starting with its fundamental formulation.

3.4.1 Fundamentals of peridynamics

Several peridynamics model have been developed during the recent years; we will review only the bond-based formulation (Dipasquale [2014]; Silling [2010]; Ha [2010]) as it will be the one employed afterwards. In peridynamics, the solid body $\mathcal{B}$ is assumed to be composed of material points located at their reference position $\boldsymbol{X}_0$ (from now on referred as point $\boldsymbol{X}_0$) and treated in a Lagrangian manner. The interaction of $\boldsymbol{X}_0$ with its neighbours is related to the parameter δ, called peridynamic horizon, which also defines the family $\mathcal{H}_{\mathcal{X}_0}$ of the considered particle: [54]

$$\mathcal{H}_{\mathcal{X}_0} = \left\{ X_0^{'} \in \mathcal{B},\ \left\| X_0^{'} - X_0 \right\| < \delta \right\} \tag{3.20}$$

where $\boldsymbol{X}_0^{'}$ is the generic point belonging to the family of $\boldsymbol{X}_0$ at his reference position. The Lagrangian equation of motion of a generic peridynamic particle is obtained via linear momentum balance: [2]

$$\rho_s \frac{d^2 \boldsymbol{X}(\boldsymbol{X}_0,t)}{dt^2} = \int_{\mathcal{H}_{\mathcal{X}_0}} f\left[\boldsymbol{X}(\boldsymbol{X}_0,t), \boldsymbol{X}^{'}\left(\boldsymbol{X}_0^{'},t\right)\right] dV_{\boldsymbol{X}_0^{'}} + \boldsymbol{F}(\boldsymbol{X}_0,t) \quad , \quad \forall \boldsymbol{X}_0^{'} \in \mathcal{H}_{\mathcal{X}_0} \tag{3.21}$$

where $\boldsymbol{F}(\boldsymbol{X}_0,t)$ is the external force density per unit volume and $dV_{\boldsymbol{X}_0'}$ is the infinitesimal volume associated to the generic point $\boldsymbol{X}_0'$. f expresses the *pairwise force density function*, whose physical unit is $[f] = [N/m^6]$. In order to define f, we have to introduce the following quantities:

$$\xi = \boldsymbol{X}_0' - \boldsymbol{X}_0 \tag{3.22a}$$

$$\eta = \left(\boldsymbol{X}' - \boldsymbol{X}_0'\right) - \left(\boldsymbol{X} - \boldsymbol{X}_0\right) \tag{3.22b}$$

Note that $\boldsymbol{X}$ and $\boldsymbol{X}'$ indicate the position at the time t of the reference points $\boldsymbol{X}_0, \boldsymbol{X}_0'$. In this way ξ is the relative distance between the points $\boldsymbol{X}_0$ and $\boldsymbol{X}_0'$ and η is their relative displacement at the time t; $(\xi+\eta)$ becomes in this way the deformed bond length. A basic representation of the peridynamic-Lagrangian structure and of ξ and η is illustrated in figure (3.12).

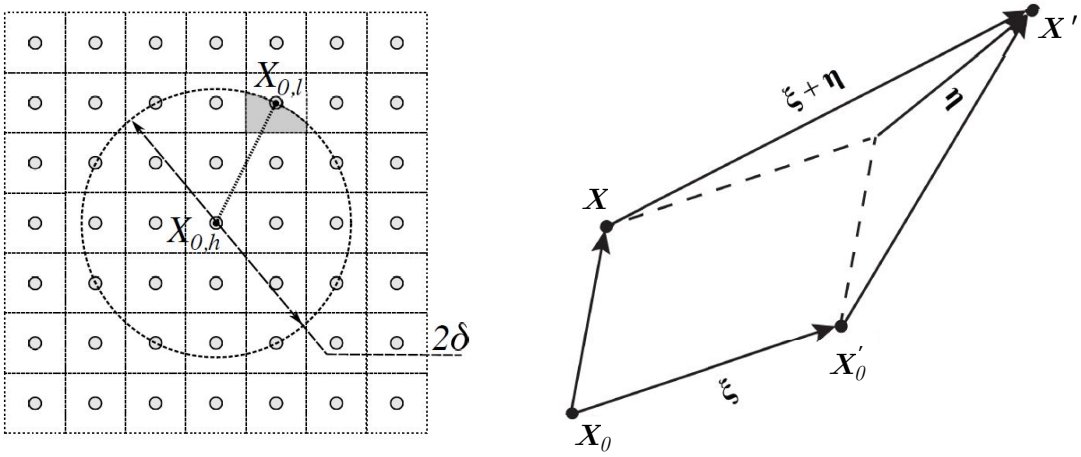

(a) (b)

Figure 3.12: (a) 2D schematic of a solid medium discretized with uniform a Lagrangian-peridynamic grid. The circle indicates the space of influence of the particle $\boldsymbol{X}_{0,h}$; the radius of the circle corresponds to the peridynamic horizon δ; $\boldsymbol{X}_{0,l}$ represents the family of nodes influenced by $\boldsymbol{X}_{0,h}$. (b) Relative position ξ and relative displacement η of points $\boldsymbol{X}_0$ and $\boldsymbol{X}_0'$. [54],[55]

We can define the following expression for the pairwise force function:

$$f(\xi,\eta) = c_0\,\lambda(s)\,s\frac{\xi+\eta}{\|\xi+\eta\|} \tag{3.23}$$

where s is the bond stretch:

$$s(\xi,\eta) = \frac{\|\xi+\eta\| - \|\xi\|}{\|\xi\|} \tag{3.24}$$

The parameter c_0 is identified as the *bond micromodulus* or *bond stiffness*; it can be assumed either constant or time-dependent. This naturally modifies the material response, generating both linear and non-linear behaviours. When the bond stiffness is constant the material represented becomes a linear elastic material until the failure condition is met. [56] Crack formation is treated through the parameter $\lambda(s)$ which is defined as the following:

$$\lambda(s) = \begin{cases} 1, & s \leq s_0 \quad \forall t \geq 0, \\ 0, & \text{otherwise.} \end{cases} \tag{3.25}$$

when the bond stretch exceeds the maximum value, the pairwise interaction is cancelled and from that time forward the particle involved is neglected. In this way, the rupture of bonds is able to represent effectively the crack propagation mechanism, without the need of introducing any additional models. Bond micromodulus and maximum bond stretch are the fundamental quantities that characterize a bond-based peridynamic model; they can be expressed through constitutive relations using the macroscopic mechanical properties of the material.

Starting with the bond stiffness, c_0 can be expressed as the following:

$$c_0 = \begin{cases} \frac{9E}{\pi t \delta^3} & \text{for 2D plane stress problems,} \\ \frac{48E}{5\pi t \delta^3} & \text{for 2D plane strain problems,} \\ \frac{12E}{\pi \delta^4} & \text{for 3D problems,} \end{cases} \tag{3.26}$$

where E is the Young's modulus of the material and t is the thickness of the 2D body (plate). Similarly, we can evaluate the limit bond stretch with:

$$s_0 = \begin{cases} \sqrt{\frac{4\pi G_0}{9E\delta}} & \text{for 2D plane stress problems,} \\ \sqrt{\frac{5\pi G_0}{12E\delta}} & \text{for 2D plane strain problems,} \\ \sqrt{\frac{5G_0}{6E\delta}} & \text{for 3D problems,} \end{cases} \tag{3.27}$$

where G_0 is the *energy release rate* of the material (Irwin, 1957), that is the rate at which potential energy is converted (developing heat, for example) during crack opening. It can be expressed as the decrease of total potential energy versus

the increase of fracture area. In Irwin's theory, the crack propagates when the energy release rate reaches its critical value, called *fracture toughness.* [2],[57] The crack case here considered corresponds to the mode I.

It should be noted also that the coefficients here presented are valid only for an elastic isotropic material usually identified as *prototype microelastic brittle model* (PMB); Poisson's ratio of the material is assumed to be equal to 1/4 for 3D and plane strain cases and 1/3 for 2D plane stress. This represents the main limitation associated with the bond-based model. Note, however, that although the reference state of the peridynamic material is isotropic, crack propagation will eventually develop anisotropy. [57],[58] The limitation associated to the Poisson's ratio is overcome adopting a state-based peridynamic model; here, the mutual interactions between material points are dependent on the collective action of all the particles inside the horizon. [56] This however greatly amplifies the computational cost, as the number of bonds considered per iteration is amplified. State-based models will not be described by this review as they will not be applied in the final algorithm, falling outside the scope of this research.

3.4.2 Numerical discretization

The solid domain is discretized with a uniform Lagrangian grid and the peridynamic particles are represented with nodes of finite volume ΔV_l, which interacts mutually between each other. In this case, the peridynamic horizon becomes $\delta = m/\Delta_s$, where Δ_s is the mean grid spacing of the solid and m is a user-defined parameter (it's usually set to 2 or 3). We can then rewrite equation (3.21) for a generic Lagrangian node $\boldsymbol{X}_h$ as the following:

$$\rho_s \frac{d^2 \boldsymbol{X_h}}{dt^2} = \sum_{l=1}^{N_h} \left(c_0 \lambda_{h,l} s_{h,l} \frac{\xi_{h,l}+\eta_{h,l}}{\left\| \xi_{h,l}+\eta_{h,l} \right\|} \alpha_{h,l} \Delta V_l\right) + \boldsymbol{D}_h + \boldsymbol{F}_h \tag{3.28}$$

where N_h is the number of nodes included in the family of $\boldsymbol{X_h}$, $\boldsymbol{F}_h$ the external force applied on $\boldsymbol{X_h}$ and $\boldsymbol{D}_h$ an additional term introducing an internal damping effect. In particular, $\boldsymbol{F}_h$ is the sum of the hydrodynamic loads $\boldsymbol{B}_h$ and solid-solid contact forces $\boldsymbol{C}_h$; the damping term $\boldsymbol{D}_h$ is defined in this manner:

$$\boldsymbol{D}_h = -k_d \sum_{l=1}^{N_h} \left(U_l - U_h\right) \cdot \frac{\xi_{h,l}+\eta_{h,l}}{\left\| \xi_{h,l}+\eta_{h,l} \right\|} \alpha_{h,l} \Delta V_l \tag{3.29}$$

with k_d the internal damping coefficient $[N \cdot s/m^7]$. This additional term produces internal damping forces that do not affect lower-frequencies oscillations but only modes associated to the higher frequencies, suppressing the sub-horizon motions thus improving the overall stability. [2] Further explaining on the computation of this forces will be done in the following chapter (chap. 4.1.2).

The numerical integration computed in equations (3.28-3.29) is also improved introducing the parameter $\alpha_{h,l}$, which accounts for the effective volume partition associated to the peridynamic particle $\boldsymbol{X_l}$ paired with $\boldsymbol{X_h}$. Considering the schematic in figure (3.6a) we can define:

$$\alpha_{h,l} = \frac{\triangle V_{l,h}^{\boldsymbol{in}}}{\triangle V_{l,h}^{\boldsymbol{out}} + \triangle V_{l,h}^{\boldsymbol{in}}} \tag{3.30}$$

where $\triangle V_{l,h}^{\boldsymbol{in}}$ is the volume of the particle $\boldsymbol{X_l}$ included in the horizon of $\boldsymbol{X_h}$, while $\triangle V_{l,h}^{\boldsymbol{out}}$ is the excluded portion. [54]

Implementing a third-order Runge-Kutta scheme, we can solve equation (3.28) in the following way:

$$\boldsymbol{X}_h^r = \boldsymbol{X}_h^{r\text{-}1} + \triangle t_p (\alpha_r \boldsymbol{U}_h^{r\text{-}1} + \beta_r \boldsymbol{U}_h^{r\text{-}2} - \gamma_r \boldsymbol{U}_h^{r\text{-}3}) \tag{3.31a}$$

$$\boldsymbol{U}_h^r = \boldsymbol{U}_h^{r\text{-}1} + \frac{\triangle t_p}{\rho_s} (\alpha_r PRHS_h^{r\text{-}1} + \beta_r PRHS_h^{r\text{-}2} - \gamma_r PRHS_h^{r\text{-}3}) \tag{3.31b}$$

where r is the Runge-Kutta integration step, $r \in [1{:}3]$, $\triangle t_p$ is the peridynamic timestep and $PRHS$ is the right-hand side of equation (3.28); α_r, β_r, and γ_r are the Rung-Kutta coefficients for the third-order scheme. In this case the solver is explicit, as the state of the system computed is obtained from the previous timestep.

It is also possible to formulate a scalar field representing the damage condition of the material through the distribution of the $\lambda(s)$ value across the Lagrangian-peridynamic grid. For a generic peridynamic node $\boldsymbol{X_h}$, we can define the damage level as: [54],[56],[58]

$$\boldsymbol{\Phi}_h = \frac{broken\ bonds}{initial\ bonds} = \frac{\sum_{l=1}^{N} \lambda_{h,l}\, \alpha_{h,l}\, \triangle V_l}{\sum_{l=1}^{N} \alpha_{h,l}\, \triangle V_l} \tag{3.32}$$

where N is the number of interacting nodes included in the horizon of $\boldsymbol{X_h}$.

It can be noted from figure (3.13b-c), how cracks tend to propagate easier in the horizontal direction, as the number of bonds that have to be broken are less than the ones ruptured when crack path is diagonal. This arise an issue that must be taken into account when dealing with crack propagation and its direction: crack path is grid dependent. [56]

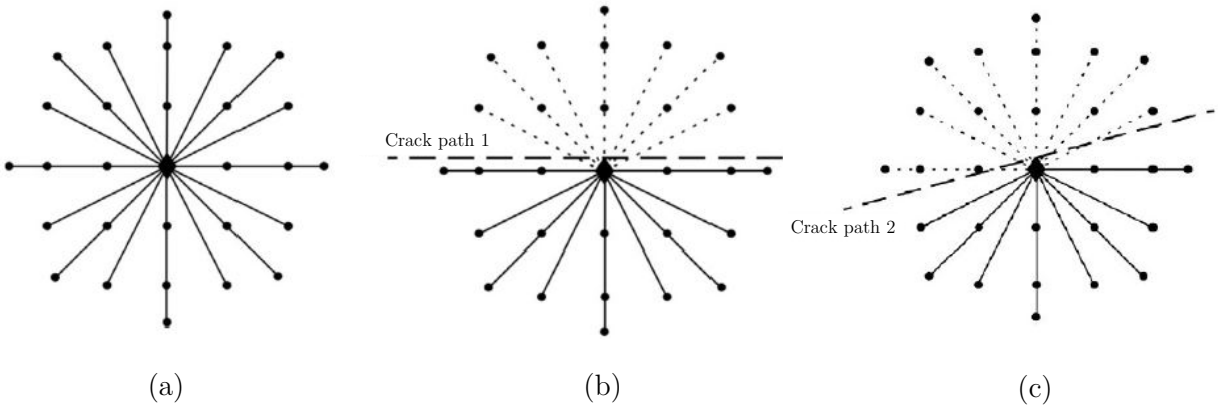

Figure 3.13: Schematic of the damage level definition. (a) undamaged condition for the bonds of a generic node; (b) damaged condition and crack propagation, case 1; (c) damaged condition and crack propagation, case 2. Note how the number of bonds broken in the second case is higher. [56]

This effect is common in many finite-element methods which implement discontinuities treatment, as mesh presence tends to constrain the path the fracture moves along. In peridynamics the effect is similar, as the discrete distribution of bonds between the nodes establishes a set of predetermined direction which must be followed by the crack. A solution to reduce this effect is to increase grid resolution, extending in this way the number of bonds included in the particle horizon; this also corresponds to an increase of the m factor. In figure 3.14 we can appreciate the described effect:

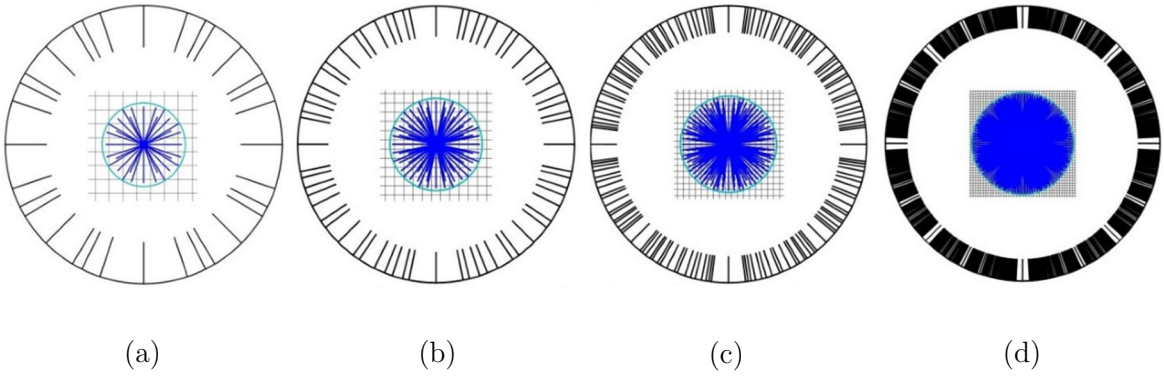

Figure 3.14: Schematic of the bond direction for different values of the m factor. (a) m=3; (b) m=5; (c) m=8; (d) m=20. [57]

It is evident that increasing m or the grid resolution cannot be done indefinitely, as the computational cost hugely rises when the number of bonds and peridynamics particles increases. An effective solution could be implementing an algorithm of grid refinement (i.e. [56],[60],[61]), adding nodes in proximity of the crack tip in order to mitigate the effect of grid dependency; this strategy will not be applied to the present research due to the high geometrical complexity of the model studied.

Another limitation related to the peridynamic theory we should briefly evaluate is the boundary conditions treatment and the surface effect. Essentially, when the fundamentals peridynamic parameters associated to the PMB material are derived, it is assumed that the family of the generic node $\boldsymbol{X_h}$ is fully included in the solid domain. This, however, is not true for the nodes close to the solid border, as part of the particles expected to be present inside the horizon does not exist, being outside the body domain (fig. 3.15). The horizon of the border particle takes a truncated shape, causing in this way an inaccurate determination of the PMB quantities, such as the bond micromodulus c_0.

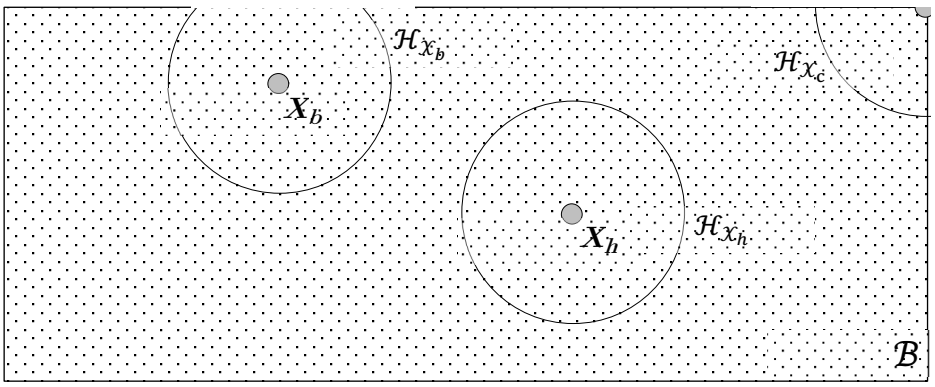

Figure 3.15: Material point $\boldsymbol{X_h}$,$\boldsymbol{X_b}$ and $\boldsymbol{X_c}$ in a 2D domain; $\boldsymbol{X_b}$ and $\boldsymbol{X_c}$ present a truncated family domain being located near the external surface.

The missing family does not contribute to the overall deformation energy of the body; when for example the domain in figure (3.15) is loaded and stretches, the deformation energy density near the solid boundaries is lower than the bulk. This is caused by the lesser number of bonds which characterizes boundary nodes. The

main consequence related to this phenomenon is that the boundaries of the body modeled with the peridynamic approach appear to be artificially softer than the rest of the material as the local elastic modulus decreases; this effect is known as *soft boundary effect* or *skin effect.* [55],[59]

Some studies (Kilic & Madenci, 2010) were carried in order to address this effect and mitigate it, however the correction factor that was applied to c_0 failed to represent non-homogenous materials. A complete solution is yet to be found. [59]

Lastly, let us evaluate a plausible timestep capable of effectively describing the phenomenon; a popular approach found in literature [62] to estimate the maximum critical timestep is to employ the Courant-Friedrichs-Lewy (CFL) method:

$$\Delta t_{p,min} = \frac{\Delta_s}{c_w} \tag{3.33}$$

$$c_w = \sqrt{\frac{K}{\rho_s}} \tag{3.34}$$

where c_w is the wave speed that propagates inside the solid medium and K is its bulk modulus, which for a homogenous isotropic material (PMB) is equal to:

$$K = \frac{E}{3(1\text{-}2\nu)} \tag{3.35}$$

Thus, the critical timestep is:

$$\Delta \mathrm{t}_{\mathrm{p,min}} = \Delta_s \sqrt{\frac{\rho_s}{K}} \tag{3.36}$$

It is essential to ensure that $\Delta t_p \leq \Delta t_{p,min}$, as higher values of the timestep could create an aliasing effect, preventing a proper observation and solution of the crack propagation phenomenon.

Chapter conclusion

Now that we have reviewed the main methods that will be involved for the present research, showing respectively their upsides and downsides, we will present the test-case studied together with its solving process. The coupling of the peridynamic solver with the IBM approach will be discussed in the following chapter, with reference to the consideration performed in the previous sections.

Chapter 4

Definition of the problem

This chapter will provide a description of the solver employed to lead the FSI analysis and its relative process. The reference methods will be the ones introduced in the previous chapter; the coupling of the fluid and solid solver will be presented together with the computation process of internal and external forces. The generation of the geometry and its configuration will be also reported.

4.1 CaNS-ExPS

CaNS-ExPS [64] is a double precision parallelized Fortran code developed specifically for solving fluid-structure interaction problems. It is capable of running DNS simulations coupled with a peridynamic solid solver, employing an IBM module to handle interface conditions. The code follows the partitioned approach logic, using a non-conformal uniform Eulerian mesh to discretize the fluid domain and a Lagrangian grid to characterize the solid medium. The solid and fluid solvers are two-way coupled, meaning that the two phases interact at every iteration and are solved concurrently. The validation and testing of its modules has already been done successfully [2].

4.1.1 DNS and PD module coupling

Fluid and solid solver are coupled together through an IBM module, which interfaces the Eulerian and Lagrangian grid, allowing the two phases to interact with each other. The DNS module was developed starting from the open source solver CaNS [63], expanding it through the implementation of an IBM module capable of detecting and tracking an immersed body in the fluid domain.

Time integration, in this case, is performed by a low-storage third order Runge-Kutta algorithm while spatial integration by finite differences method, using an efficient FFT-based solver. [63] The fluid domain is discretized by a fixed, uniform,

non-conformal, staggered mesh grid; every element is of cubical shape and of volume $\triangle x^3$. Boundary conditions for the fluid field are enforced through the use of ghost nodes located outside the computational domain; velocity and pressure inflow/outflow conditions can be imposed through Dirichlet and Neumann conditions, as well as periodicity. No-penetration and no-slip conditions are enforced through the discrete-forcing approach presented in chapter 3.2.2.

The solution of the solid medium is instead carried on through an explicit peridynamic solver (ExPS) [64] that performs time integration of equation (3.28). The body is discretized by a set of Lagrangian points arranged in a uniform equally-spaced grid; the grid moves with the solid-fluid interface, assuring at every timestep that each node of the grid coincide with the position of the peridynamic particle. In first approximation, the volume of the generic peridynamic particle is as well $\triangle x^3$.

The numerical algorithm is implemented in FORTRAN90/95, with a Message-Passage Interface (MPI) extension to allow parallel processing; the geometry is decomposed in pencil-like computational subdomains in order to parallelize the process efficiently. [63]

The scheme followed by the two solvers can be summarized in this way:

(1) A first prediction of the velocity field is performed (3.14a), integrating Navier-Stokes equations over a time interval Δt, with no consideration about the fluid-solid interface.

(2) No-slip and no-penetration conditions enforcement are carried on by the IBM module, following a multidirect forcing scheme (chap. 3.2.3).

(3) Pressure and velocity fields are updated to the next timestep through a pressure-correction scheme similar to (3.14b-3.14e). The position of the solid-fluid interface is still fixed at the initial timestep.

(4) The Lagrangian equations presented in the scheme (3.31a-b) are then advanced over the same time interval Δt through sub-steps of $\Delta t_p = r\Delta t$; $r < 1$ to ensure numerical stability. Finally, solid-fluid interface location is updated in time.

The fluid and solid solver are treated independently, working in parallel through a closely coupled partitioned approach (chap. 3.1.1). However, they still need to communicate in order to correctly update the interface location and apply the surface loads. The approach followed is two-way coupled because the loads computed through the IBM module are then employed by the peridynamic solver to compute the motion of the solid particles, which in turn, will influence fluid's motion in the next iteration.

As long as the solid and fluid solver cannot run at the same time, the peridynamic solver is called with a higher frequency, using shorter timesteps (stagger loops). In this way, solid bodies are assumed to evolve through quasistatic states; this is true, however, only when time intervals and body deformations are small. To solve this problem, an additional damping factor for the velocities of the particles is introduced as already presented in equations (3.28-29).

The choice of the parameter k_d naturally affects the final solution; it should be noted, however, that only higher frequencies modes will be damped. This will not represent a problem in our case, as long as acoustic phenomena are neglected by the intended simulation given the incompressibility configuration.

4.1.2 Dimensional analysis

Another important consideration that has to be accounted in order to ensure the correct coupling of the solvers regards the dimensions assigned to the respective quantities. Navier-Stokes equations are handled via the imposition of the Reynolds number, so the fluid phase is solved in a non-dimensional form. On the other hand, the peridynamics has to be solved in a dimensional form; in this way when the IBM module computes the loads, these are adjusted by a proper scaling factor.

The IBM loading scaling factor f^* can be determined by leading a dimensional analysis on the complete IBM-NS equation [65]:

$$f^* = \rho_f \cdot (U^2/L) \tag{4.3}$$

Where U and L are the characteristic length and velocity scale of the flow, as already explained in (chap. 3.1.2). In this way, the force transmission between the IBM and PD modules is managed employing the following relation:

$$\boldsymbol{F}_{PD} = \boldsymbol{f}_{IBM} \cdot f^{*} \tag{4.4}$$

Similarly, the displacement applied to the Lagrangian grid is handled in this way:

$$\Delta \boldsymbol{x}_h = \boldsymbol{X}_h \,/\, L \tag{4.5}$$

where $\Delta \boldsymbol{x}_h$ is the effective displacement of the generic Lagrangian node h over the time interval Δt. In this way, the dimensional displacements of the PD nodes are transferred as non-dimensional displacements in the Eulerian framework, ensuring a proper detection of the solid-fluid interface for the fluid next iteration.

We can further look into the problem by performing a dimensional analysis of the discretized peridynamic equation; if we rewrite equation (4.1) and highlight the characteristic dimensions for every quantity, we obtain:

$$\rho_s \frac{d^2 \boldsymbol{X_h}}{dt^2} \left[\frac{U^2}{L}\right] = \sum_{l=1}^{N_h} (f\, \alpha_{h,l} \Delta V_l) \left[\frac{E}{L}\right] + \boldsymbol{D}_h\, \rho_s \left[\frac{U^2}{L}\right] + f^{*} \boldsymbol{f}_{IBM,h} \tag{4.6}$$

where the damping term for the absolute velocities is indicated with $\boldsymbol{D}_{a,h}$ and the PD force has been replaced with the notation (4.4). We can proceed by regrouping the characteristic dimensions in the following way:

$$\frac{d^2 \boldsymbol{X_h}}{dt^2} = \sum_{l=1}^{N_h} (f\, \alpha_{h,l} \Delta V_l) \left[\frac{E}{\rho_s U^2}\right] + \boldsymbol{D}_h + \left[\frac{\rho_f}{\rho_s}\right] \boldsymbol{f}_{IBM,h} \tag{4.7}$$

We can identify two different dimensional group in equation (4.7) that, likewise the Reynolds number for equation (3.4), control the response of the peridynamic module. Therefore, similarity for the peridynamic module is assured when these quantities remain constant. In this way, when dealing with FSI problems, the case studied remains unchanged as long as the following dimensional groups are kept constant:

$$Re = \frac{\rho_f\, UL}{\mu} \quad , \quad \zeta = \frac{E}{\rho_s U^2} \quad , \quad \psi = \frac{\rho_f}{\rho_s} \tag{4.8}$$

In figure 4.1 we report the flowchart of the complete coupled algorithm.

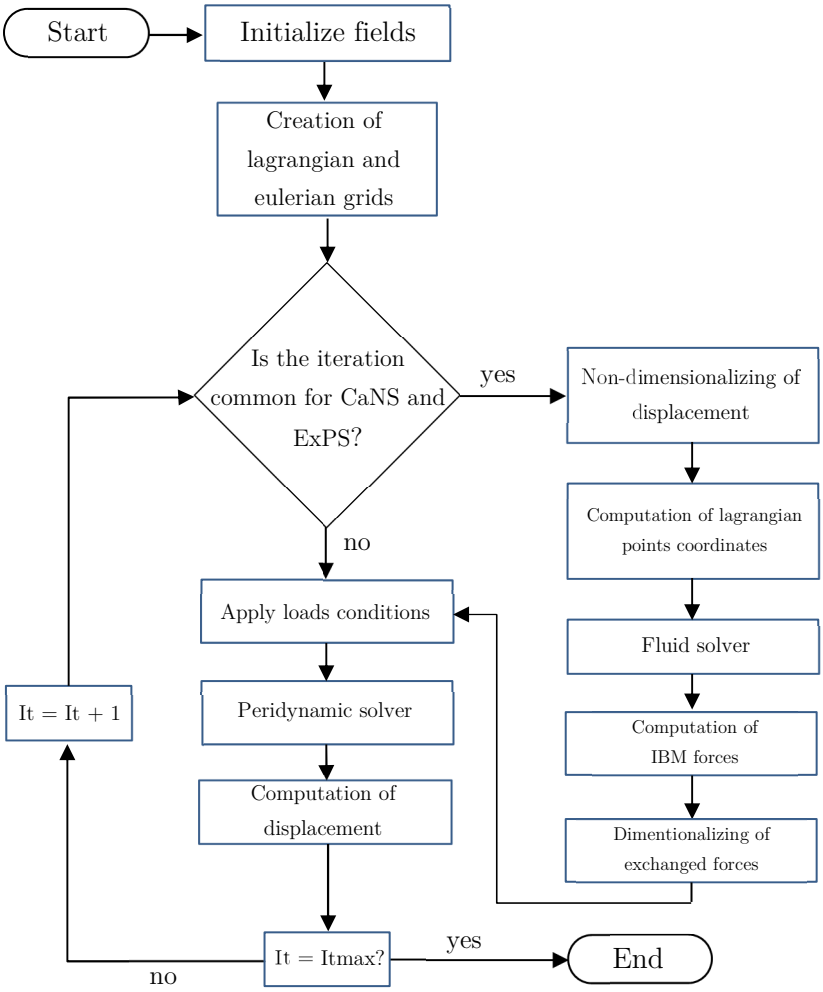

Figure 4.1: Flowchart scheme of the algorithm. [65],[66]

4.1.3 Interface handling and forces computation

In order to describe correctly the interaction between the solid structure and the fluid, the interface must be opportunely tracked through time; this include not only the borders of the solid immersed in the fluid but also the fragments that have been removed from the surface and are free to roam in the domain. In CaNS-ExPS interface detection is performed through an additional algorithm [2] that locates in the Lagrangian framework a set of Lagrangian markers; these markers consist in a subset of peridynamic nodes that compose the solid body and are named *interfacial particles.* As long as markers are also peridynamic particles, their tracking in time is effectively performed by the solid solver that integrates in time their velocity.

Their numerical detection is achieved through a geometrical criterion that compares the number of neighbours nodes for every peridynamic particle.

Once the interface has been located, external and internal forces are then applied. Let us evaluate the process to compute solid-solid contact forces $\boldsymbol{C_h}$ and hydrodynamic loads $\boldsymbol{B_h}$.

The solid-solid contact forces are computed as a pairwise force interaction between peridynamics particles that are located inside a cut-off distance r_c; given a couple of interfacial peridynamic particles $\boldsymbol{X_h}$ and $\boldsymbol{X_l}$, the short-range force on $\boldsymbol{X_h}$ due to contact with $\boldsymbol{X_l}$ is:

$$\boldsymbol{C}_{h,l} = max\left\{k_c\left[\left(\frac{r_c}{r_{h,l}}\right)^{n_c} - 1\right], 0\right\} \cdot \frac{\boldsymbol{X_l - X_h}}{\|\boldsymbol{X_l - X_h}\|} \tag{4.2a}$$

where $r_{h,l}$ is the distance between $\boldsymbol{X_h}$ and $\boldsymbol{X_l}$, n_c is the force exponent and k_c is the short-range force constant. [2] These parameters represent the fundamental quantities that characterizes the contact model; according to Silling & Macek (2007) these parameters can be set in the following way:

$$\boldsymbol{C}_{h,l} = max\left\{15\,c_0\left[\left(\frac{\Delta_s}{r_{h,l}}\right) - 1\right], 0\right\} \cdot \frac{\boldsymbol{X_l - X_h}}{\|\boldsymbol{X_l - X_h}\|} \tag{4.2b}$$

Using a *nearest-neighbour-search* (NNS) algorithm, the contact force is applied to the interfacial particles located inside the cut-off distance.

On the other hand, for what concerns the computing of the hydrodynamic stresses, normal-probe method has been adopted. [2] The reaction of the fluid on the solid surfaces is determined by evaluating the pressure gradient and viscous stresses in proximity of the interface. This requires, however, the computation of the normal vector to the surface, which, for an interfacial particle can be approximated using the distances of interaction between the particles and its neighbours. The tangent and bi-normal vectors are computed accordingly. A local orthogonal coordinate system is then defined, according to the normal and tangent vectors; in correspondence of each Lagrangian interfacial position $\boldsymbol{X_h}$, a probe of length $l = 2\Delta x$ is defined along the local normal vector (fig. 4.2). [54]

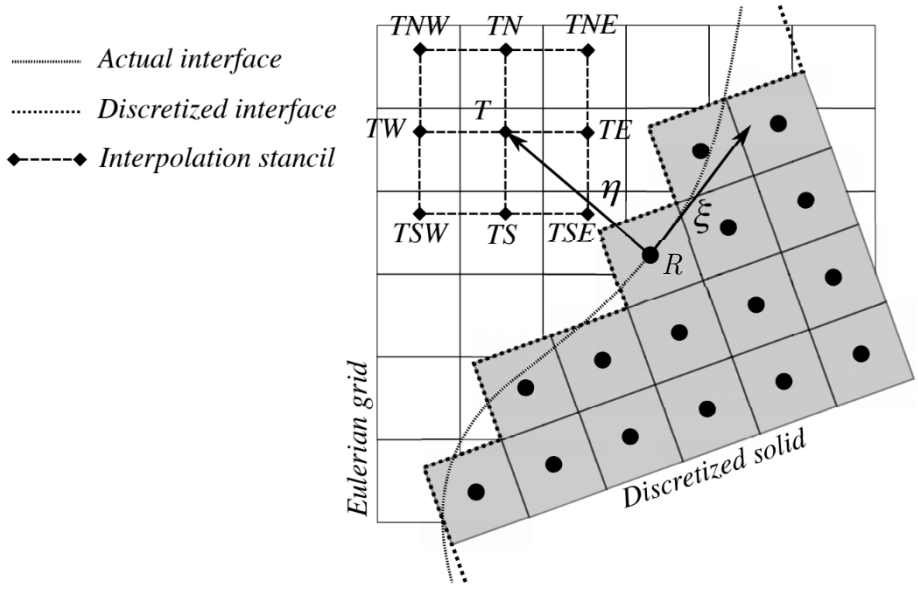

Figure 4.2: 2D schematic of the normal probe method adopted to compute the hydraulic stresses on the fluid-solid interface. The figure illustrates the stencil used to compute the velocity and pressure gradients at the normal probe tip; it is shown also the curvilinear local frame of reference defined by the tangent and normal vector to the solid surface. [54]

The fluid pressure is obtained at the probe root R by interpolation of the pressure field at the probe tip T, using a computational stencil (fig. 4.1); similarly, the viscous shear stress at R is determined by interpolation of the Eulerian velocity in T. Once the overall stress is computed, we can express it in the global framework of reference, and we can finally compute $\boldsymbol{B_h}$ as:

$$\boldsymbol{B}_h = -\tau_h \frac{A_h}{\triangle_s^3} \tag{4.3}$$

where τ_h is the overall viscous stress and A_h is the specific surface area involved by the stress.

Having properly introduced the algorithm that will be employed and the relative followed steps, let us finally proceed to outline the problem involved in the present research.

4.2 Problem configuration

The subject of the proposed analysis will be a pore-scale DNS simulation of a non-convex random porous medium immersed in a laminar fluid flow. The study will focus on the process of hydraulic fracturing of the material with the purpose of

determining a simple mathematical model which could provide information on the quantities involved.

4.2.1 Computational domain configuration

The computational domain will include the fluid domain as a channel of dimensions $2d \times 1d \times 1d$ in streamwise, spanwise and wall-normal directions, together with the solid domain, represented by an RVE of dimensions $1d \times 1d \times 0.75d$; d indicates the generic dimension associated to the domain length size. The resolution for both the Eulerian and Lagrangian grid is set to $\Delta_s = \Delta_f = 1d/64$, obtaining a distribution of $64 \times 64 \times 128$ fluid nodes; the number of peridynamics nodes N_p can be computed instead by using the definition of porosity (eq. 2.1):

$$N_p = (1 - \varphi)\, N_{tot} \tag{4.4}$$

where $N_{tot} = 64 \times 64 \times 48$.

The boundary conditions enforced for the channel flow are an inflow condition at $x = 0$ which imposes a 3D Poiseuille profile for initial velocity profile, a pressure outflow at $x = 2$ and wall conditions for the y-wise and z-wise border domain. The solid body is generated in the domain $[0.25\ ;\ 1.0] \times [0\ ;\ 1] \times [0\ ;\ 1]$; the frame is bounded to the channel by constraining the outer Lagrangian points to the lateral, lower and upper walls, imposing:

$$U_x = U_y = U_z = 0 \tag{4.5}$$

The peridynamic horizon is set to $2\Delta_s$.

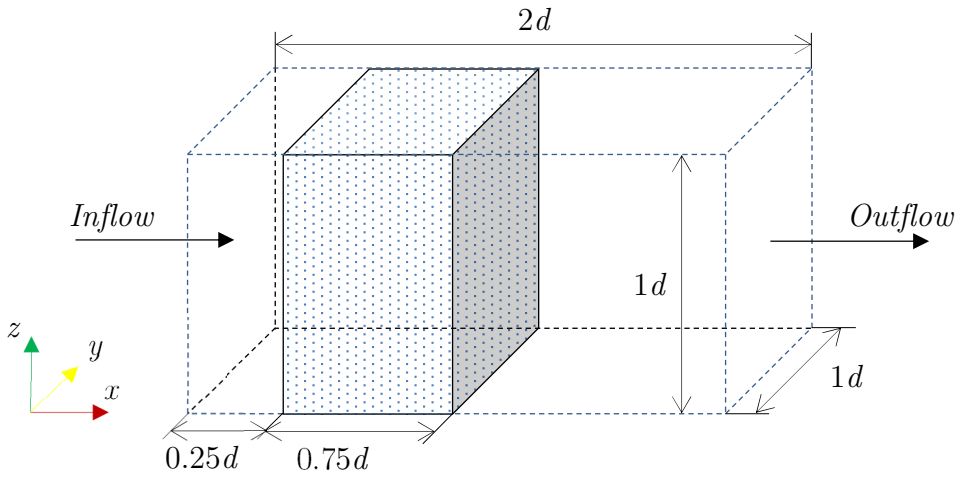

Figure 4.3: 3D schematic of the computational domain; the shaded area indicates the solid domain, the blank area the fluid domain.

4.2.2 Geometry generation

The generation of the porous medium geometry is handled through a separate algorithm that proceeds to create non-convex cavities inside a user-defined domain. The process is carried on by generating a random distribution of spheres of fixed minimum radius; a validating cycle makes sure that:

(1) The centres of the spheres created belong to the defined solid domain.

(2) The spheres do not overlap over a fixed limit.

The solid domain is progressively packed with spheres until a predefined target of porosity is reached. Afterwards, the distributed spheres are employed to create the effective final geometry by Boolean subtraction of the bulk total domain with the random distribution of bodies. At the end of the cycle, a smoothing filter is implemented in order to eliminate isolated particles or disconnected portions of the body. Figure 4.5 presents an example of the final result.

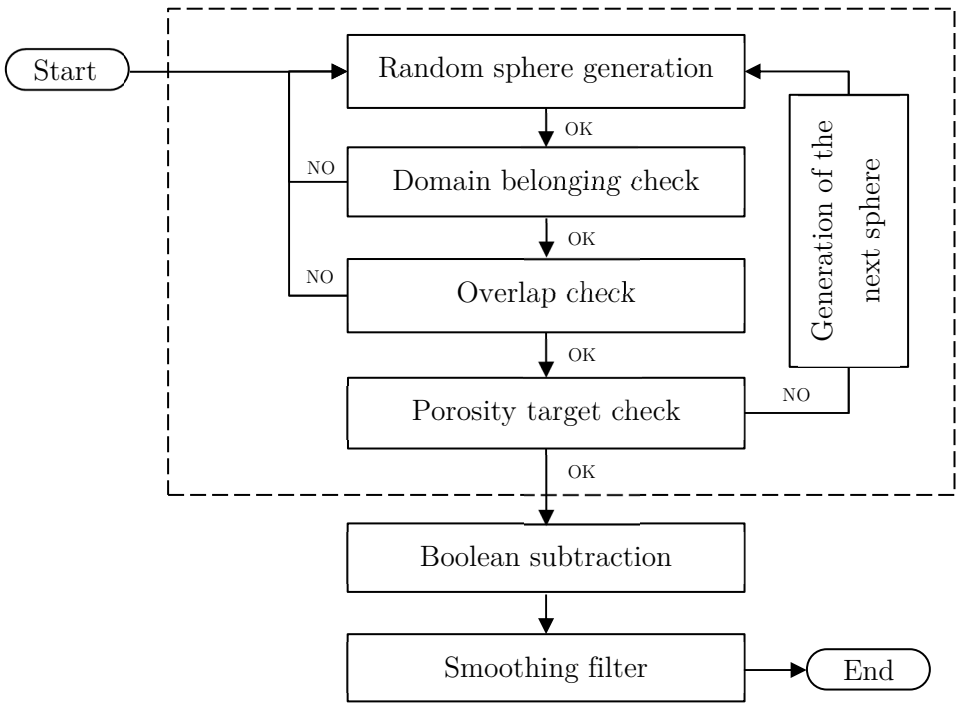

Figure 4.4: Flowchart scheme of the porous medium generation algorithm.

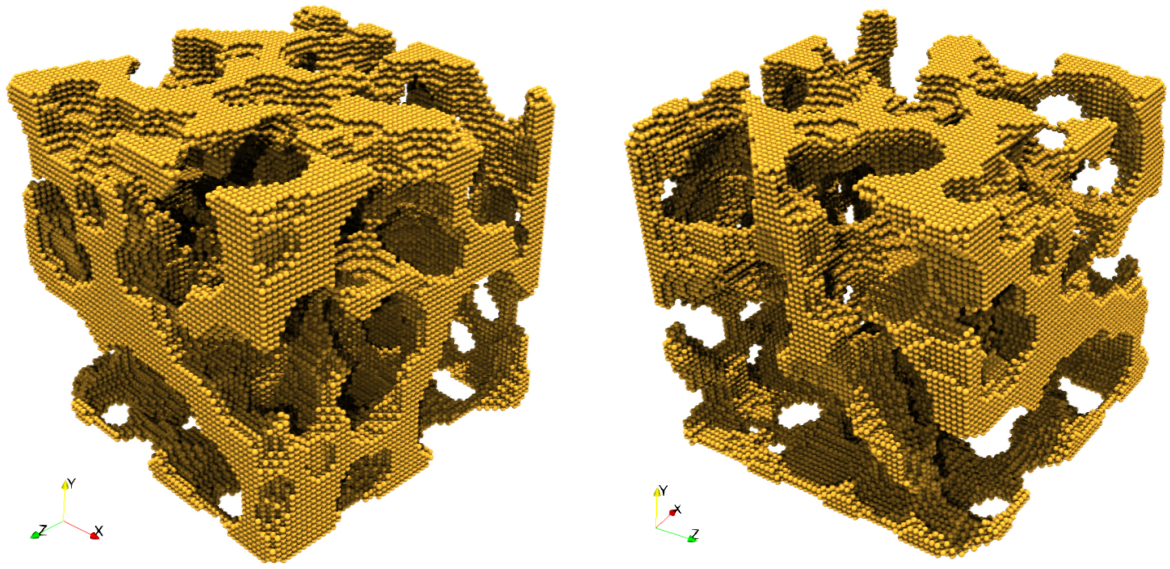

Figure 4.5: 3D render of an example of the geometrical configuration. The porosity value is equal to 0.7; in this case the solid domain is cubical unit-cell.

We report the final configuration adopted for the computational domain; the porosity target value has been set to 0.7:

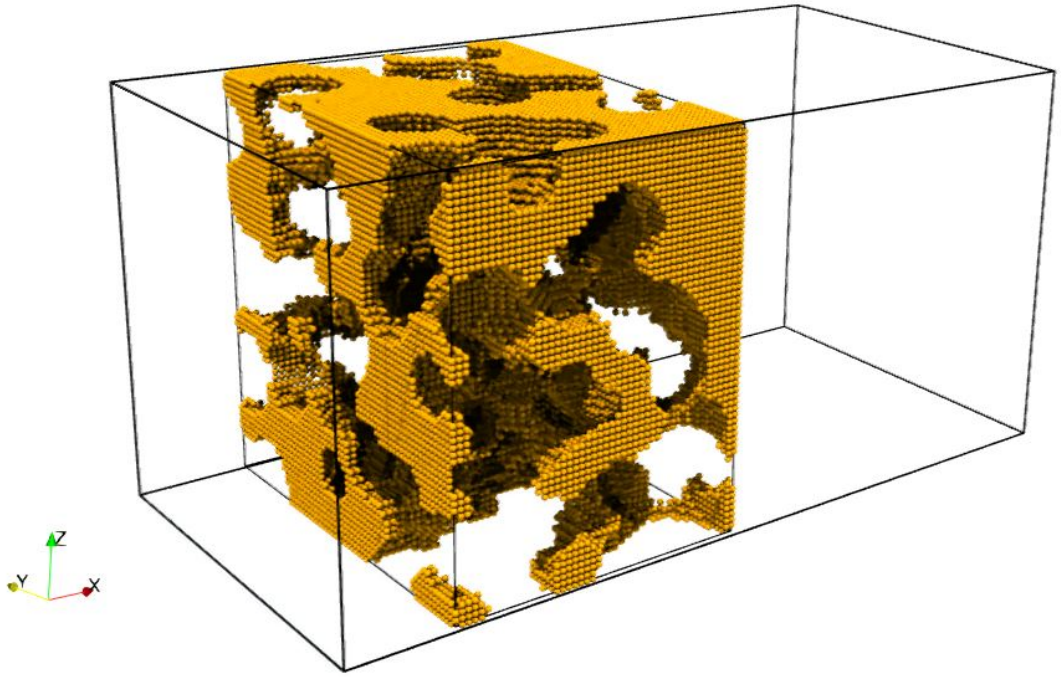

Figure 4.6: 3D render of the adopted computational domain with the final geometrical configuration. The fluid computational domain is indicated by the outer black outline.

4.2.3 Definition of the capillary model

Despite the precision and the amount of information collected from a direct numerical simulation, the definition and application of an equivalent model for the porous medium behaviour could still provide valuable data on the subject. In this way, it would be possible to predict the system response without resorting to expensive numerical analysis, saving a huge amount of computational time and resources.

Several models were introduced over the course of time; the first was the Kozeny-Carman (1937, 1956) bundle-of-tubes model, while one of the latest is the Yu & Cheng model (2001), which resorted to the fractal characteristics presented by porous media. Still, none of them was applied for describing a time-evolving process as they were employed only to evaluate the geometrical characteristics of the solid frame.

For this reason, a simple mathematical model is proposed, with the intention of capturing the fluid and solid interaction throughout the hydraulic fracturing process. The model proposed will be a modification of the one introduced originally by Kozeny (1927): to describe the percolation process of the fluid flow through the medium, we can simplify the internal geometry as a bundle of channels of constant area and length longer than the bulk. We report in figure (4.7) the schematic of the model:

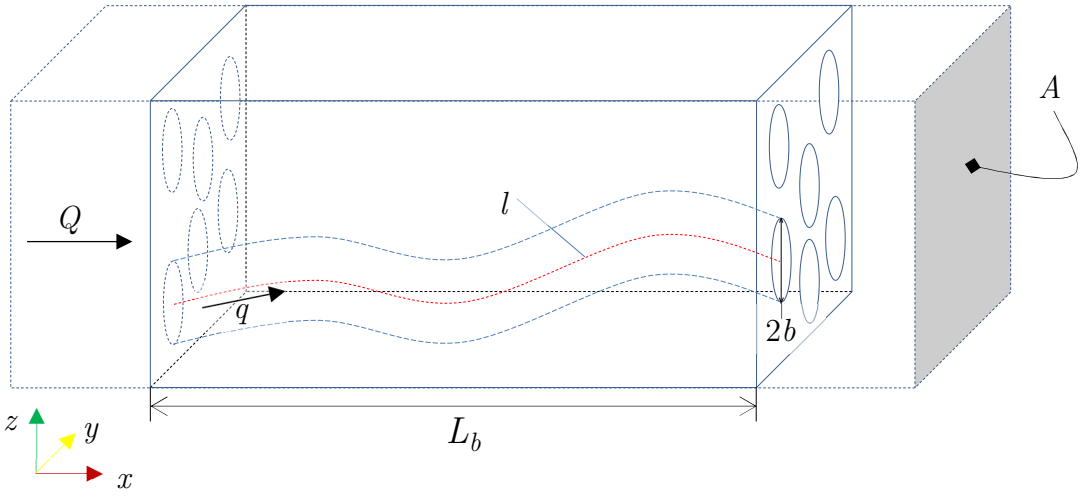

Figure 4.7: Schematic of the capillary model adopted to represent the porous medium behaviour. A is the bulk cross-section, L the bulk length, l the capillary length and b is the channel radius.

For the case presented, porosity can be expressed in the following way:

$$\varphi = \frac{V_t}{V_t + V_s} \tag{4.6}$$

where V_t is the is the void volume occupied by the capillary tubes and V_t the one occupied by the solid frame. In particular V_t and its internal surface can be expressed as:

$$V_t = n \cdot \pi b^2 l\,, \quad S_v = n \cdot 2\pi b l \tag{4.7}$$

where n is the generic number of capillary tubes inside the solid frame and b is the channel radius together with its length l. Substituting V_t in equation (4.6) and dividing both members by S_v we obtain:

$$b = \frac{2V_s}{S_v}\left(\frac{\varphi}{1-\varphi}\right) \tag{4.8}$$

Equation (4.8) is purely a geometrical consideration and can be applied for every morphological configuration of the porous medium; b in this way represents the mean pore radius of the structure and can be employed to determine the mean flow rate inside the capillary tube. For the case studied, the solid frame volume V_s and the specific surface area S_v can be approximated in the following way:

$$V_s \cong N_p \cdot \Delta_s^3 \tag{4.9a}$$

$$S_v \cong N_{interface} \cdot \sqrt{2}\Delta_s^2 \tag{4.9b}$$

where $N_{interface}$ is the number of interfacial nodes.

Applying the well-known Hagen-Poiseuille equation, we obtain:

$$q = \frac{\pi b^4}{8\mu} \cdot \frac{\Delta p}{l} \tag{4.10a}$$

where Δp is the pressure drop computed between the entrance and the exit of the tube. We can rewrite equation (4.8a) using the definition of tortuosity ($\tau = l / L_b$) obtaining:

$$q = \frac{\pi b^4}{8\mu\tau} \cdot \frac{\Delta p}{L_b} \tag{4.10b}$$

From equation (4.9b) we can compute the total flow rate that travels through the entire medium with $Q = n \cdot q$. The factor n can be easily suppressed by expressing porosity as:

$$\varphi = \frac{n \cdot \pi b^2 l}{A\, L_b} = \frac{n \cdot \pi b^2 \tau}{A} \tag{4.11}$$

In this way, we finally obtain:

$$Q = \varphi \cdot \frac{b^2 A}{8\mu\tau^2} \cdot \frac{\Delta p}{L_b} \tag{4.12}$$

which can be seen as a modified version of the Darcy's equation, where the term $\varphi \cdot \frac{b^2}{8\tau^2}$ represents the permeability of the porous medium. Equation (4.12) can be non-dimensionalized through the use of the proper quantity scales:

$$Q^*[U][L^2] = \varphi \cdot \frac{b^{*2}[L^2] A^*[L^2]}{8\mu\tau^2\ L_b^*[\mathrm{L}]} \cdot \Delta p^* \cdot \rho_f[U^2] \tag{4.13a}$$

$$Q^* = \varphi Re \cdot \frac{b^{*2} A^*}{8\tau^2} \cdot \frac{\Delta p^*}{L_b^*} \tag{4.13b}$$

where the (*) superscript indicates the dimensionless quantity. Note how in equation (4.13b) the fluid viscosity μ is associated to the Reynolds number, as long as the pressure drop is non-dimensional. Again $\varphi \cdot \frac{b^{*2}}{8\tau^2}$ is the non-dimensional permeability.

Chapter conclusion

Now that the effective modalities of the analysis have been properly introduced, let us proceed to expose the results obtained from the performed simulations, together with the evaluations carried out implementing the capillary model.

Chapter 5

Results

This chapter will present the results obtained from the performed simulations together with the evaluations obtained employing the capillary model; in particular, it will be discussed the effectiveness of the model in describing the evolution of a porous material subjected to hydraulic fracturing. A total of five DNSs have been conducted, with the intent of studying the effect of solid fracturing and crack propagation by varying the energy release rate of the material. The non-dimensional parameters set for the different analysis are the following:

Re	10.0
ζ	$0.333 \cdot 10^{5}$
ψ	3.0
ν	0.25

DNS	R1	R2	R5	R10	R15
G_0/EL	$1 \cdot 10^{-6}$	$2 \cdot 10^{-6}$	$5 \cdot 10^{-6}$	$1 \cdot 10^{-5}$	$\mathbf{1.5} \cdot 10^{-5}$

Table 5.1: Physical parameters of the simulations expressed in non-dimensional units; starting from the top, bulk Reynolds number $Re = \rho_f UL/\mu$, $\zeta = E/\rho_s U^2$, density ratio $\psi = \rho_s / \rho_f$ and Poisson's ratio. At the bottom: corresponding non-dimensional energy release rate for each simulation.

The time-step employed for every simulation has been set to $\Delta t/\tilde{t} \cong 1.35 \cdot 10^{-4}$, where $\tilde{t} = U/L$ is the reference time scale of the fluid. The initialization of the simulation is performed over the time range $t/\tilde{t} \in [0, 1.35]$; in this phase, only the fluid solver is enabled until the flow reaches a stationary state. The solid frame is then let deform, enabling the peridynamic module but keeping the bond break-up deactivated; the correspondent time range is $t/\tilde{t} \in [1.35, 2.55]$. Finally, for $t/\tilde{t} \in [2.55, 3.35]$ the bond break-up is enabled, allowing crack propagation.

Let us now proceed to review in-depth the simulation R5 (table 5.1).

5.1 DNS review

We present the results obtained from the R5 simulation ($G_0/EL = 5 \cdot 10^{-6}$); both the fluid and solid phase will be discussed, reviewing properly every simulation phase; note that the first two phases are the same for every DNS performed, as G_0 influences only the last 6000 iterations.

5.1.1 Flow initialization

The fluid phase is evolved through the porous material for 10000 iterations until it reaches a stationary state. At the end of the initialization phase, the simulated fluid flow inside the porous material is laminar, as expected from the low Reynolds number that has been imposed.

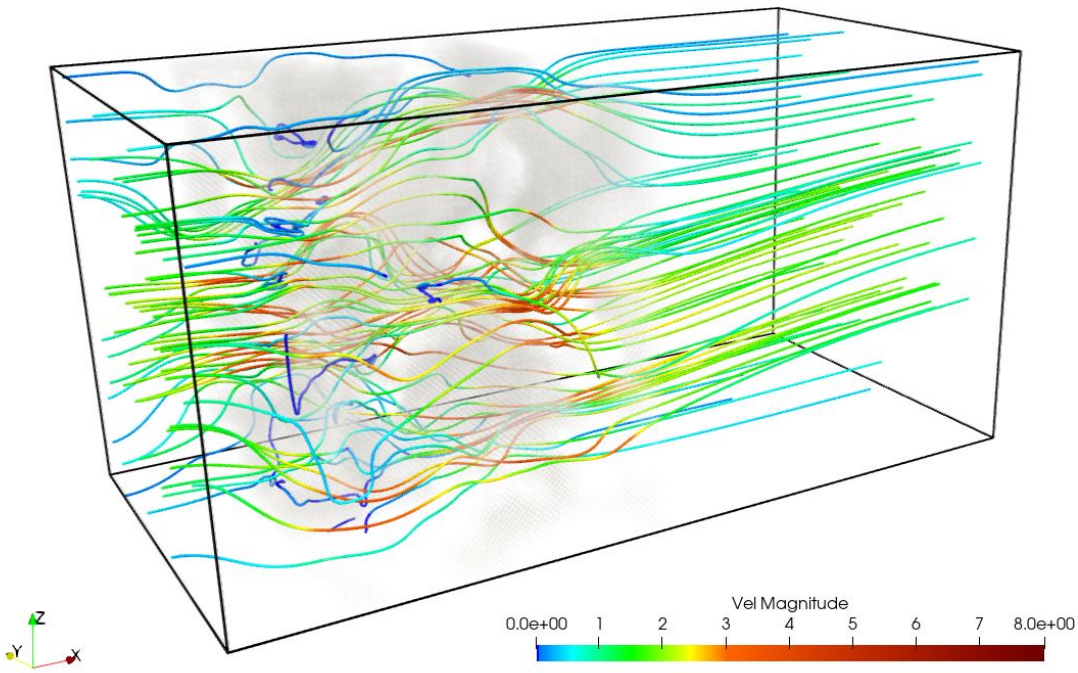

Figure 5.1: Plot of flow streamlines at the end of the initialization phase; $t/\bar{t} = 1.35$. The streamlines are coloured according to the magnitude of the non-dimensional flow velocity. The solid phase is plotted with a lower opacity in order to ease the visualization.

We can distinguish, however, some isolated eddies in particular regions of the solid. Despite the low Reynolds number, inertial effects are present in the cavities of the body due to the geometrical complexity encountered by the flow.

As long as these recirculation areas are associated to low-velocity flows, their effect can be generally neglected; the flow can be easily assumed in the Darcy's regime, given the high viscosity of the fluid phase and the low flow rate enforced as inflow condition. Still, there are some areas where the flow accelerates: these regions are associated to a sudden increase of the internal pore radius as well as to the outlets of the fluid at the end of the porous material.

We can also evaluate the pressure field distribution at $t/\tilde{t}$=1.35 (It = 10000):

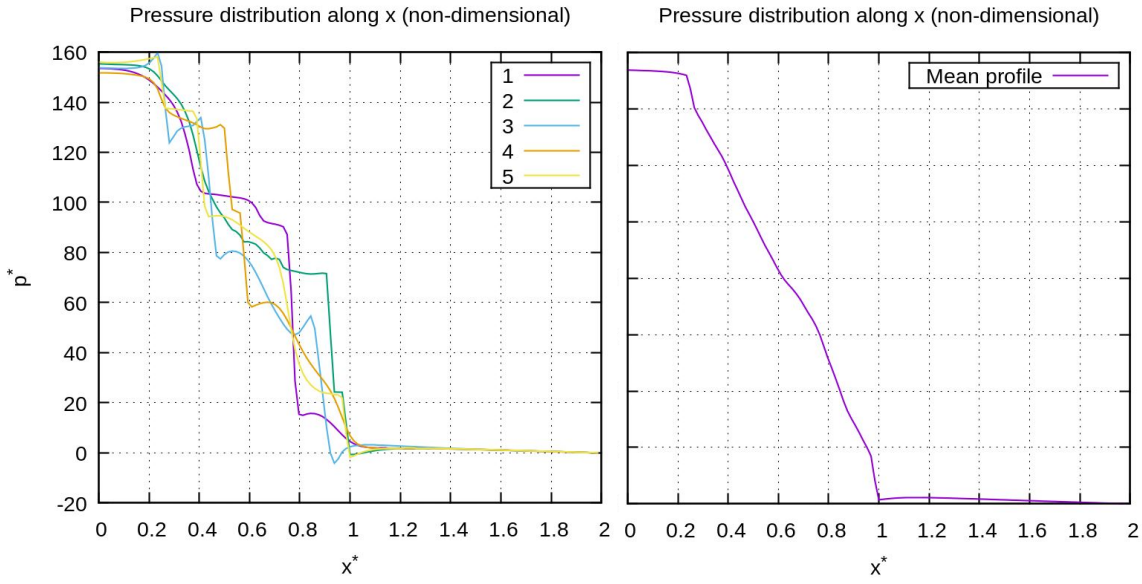

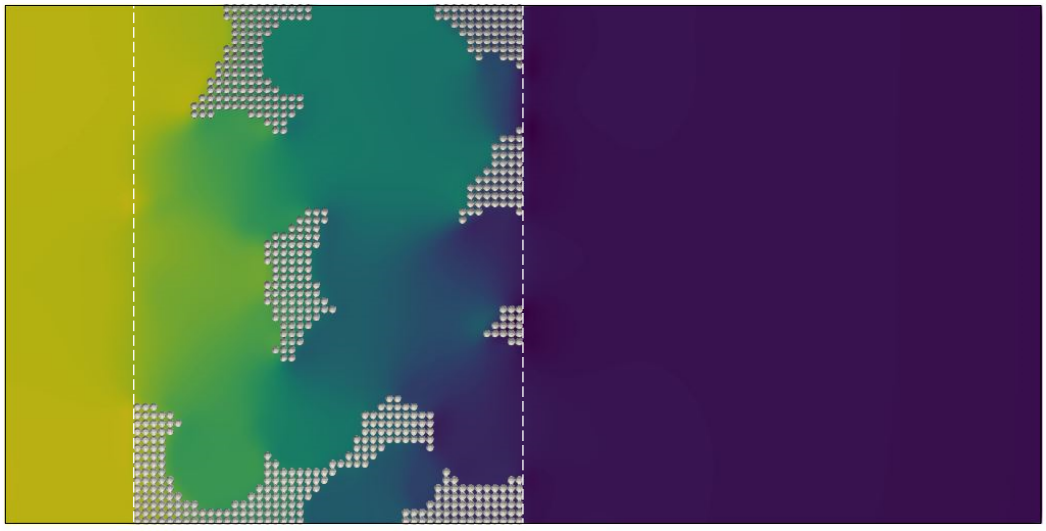

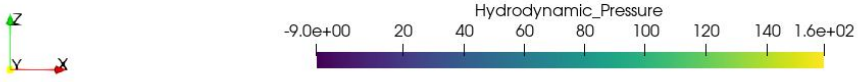

Figure 5.2: Top panel: distribution of the non-dimensional pressure along the x direction $t/\tilde{t}$ = 1.35; the scalar field is evaluated for several y-z fixed position, varying the x. The mean pressure profile is also reported. Bottom panel: contour of the non-dimensional pressure field at $t/\tilde{t}$= 1.35 on the Y-normal mid-surface.

Examining the results represented in (fig. 5.2), we can see how the pressure distribution along the x direction is quite dependent on the location considered for the computing. This is expected, given the overall geometrical complexity of the solid body; the fluid encounters different solid conformations while moving through the medium along the streamwise direction and this obviously affects the pressure distribution. The continuous widening and narrowing of the internal porous cavities generates sudden increases and decreases of the local pressure, together with the effect of solid walls that produce stagnation regions; this effect can be further appreciated examining the pressure contour at a fixed surface.

However, if we manage to compute the mean pressure distribution along x, we can immediately evaluate that the overall pressure decrease is almost linear and the pressure gradient along the streamwise direction appears fairly constant. For the case presented we can esteem the mean pressure gradient as: $\Delta p^*/\Delta L \cong$ - 200

In figure (5.3) pressure gradient distributions are reported:

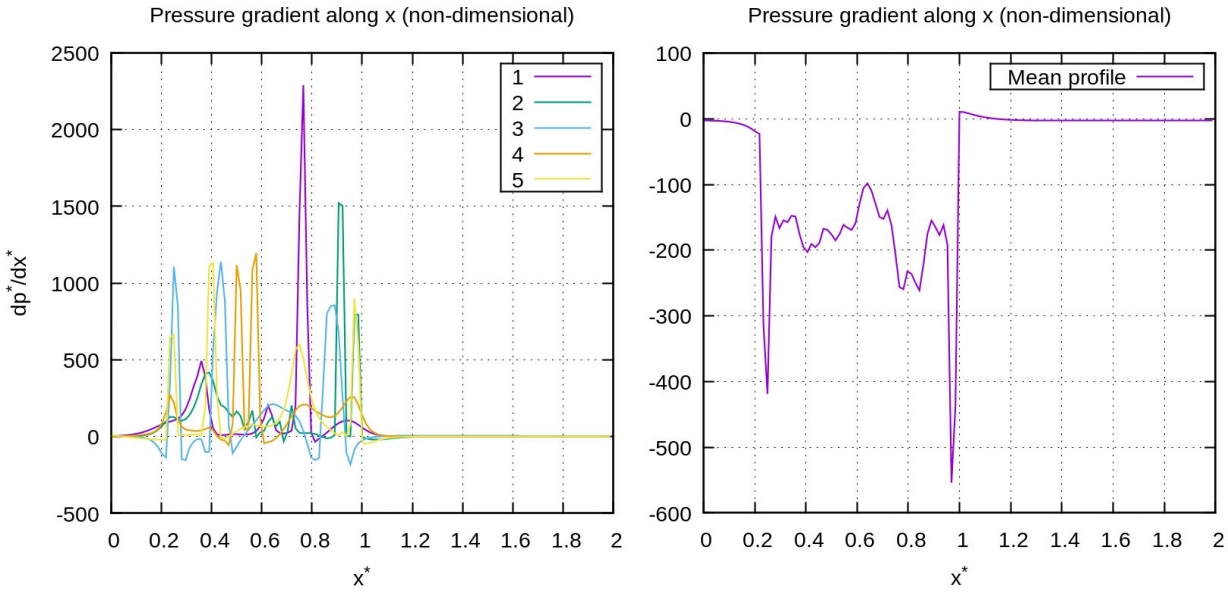

Figure 5.3: Distribution of the non-dimensional pressure gradient along the x direction $t/\tilde{t}$ = 1.35; the scalar field is evaluated for several y-z fixed position, varying the x. The mean pressure gradient profile is also reported.

Again, we can see how pressure gradient distributions along the x direction are dependent on the selected point of evaluation; sudden rises in the pressure gradient indicate the presence of stagnation and low-velocity regions inside the domain. If we evaluate the mean profile, however, the overall tendency settles around $dp^*/dx^* \cong -200$, as predicted by the mean pressure drop. Still, the fluctuations around the mean value are not negligible and could affect the general response of the system; in particular, the gradient distribution dives in proximity of the inlet and spikes at the outlet of the porous material, indicating a concentration of local perturbances. These are caused, at first, by the sudden presence of the solid body and, at last, by the abrupt flow discharge in a wider streamtube.

5.1.2 Solid initialization

Similarly to what has been done with the fluid, before turning on the bond break-up, is essential to gradually accustom the solid frame to the flow and to the applied pressure. For this reason, the simulation is carried on by performing 9000 iterations with the same timestep previously employed, releasing the particles and activating together with the fluid solver also the peridynamic solver; crack propagation is absent since the solid particles are kept connected for now.

This phase greatly stabilizes the computational process and prevents that the immediate release of the solid particles could cause numerical errors capable of leading into a computational divergence. This effect is further avoided implementing an additional damping term which is related to the particle absolute velocities.

We report two different iteration performed in this phase, $t/\tilde{t} = 2.0$ and $t/\tilde{t} = 2.55$. Let us evaluate firstly the displacement field associated to the peridynamics particles. In figure (5.4) we report the surface contours for the front and back region of the porous material, at different timesteps. Starting with the front, it can be easily seen how the displacement field of the inlet and of the wall cavities tends to follow the 3D Poiseuille inflow condition enforced at the beginning. The core regions of the material are those subjected to the biggest deformations, being the most distant from the lateral bounded walls, while, on the contrary, the material near the borders appears stiffer. Nevertheless, the largest displacements manifest at the outlet of the material, unlike what one might think from the pressure distribution.

This will be even more evident later when the fracturing process will be reviewed. In this case, the effect is further amplified by the geometry of the material, as strips of the solid connected mildly to the frame tends to be teared easily.

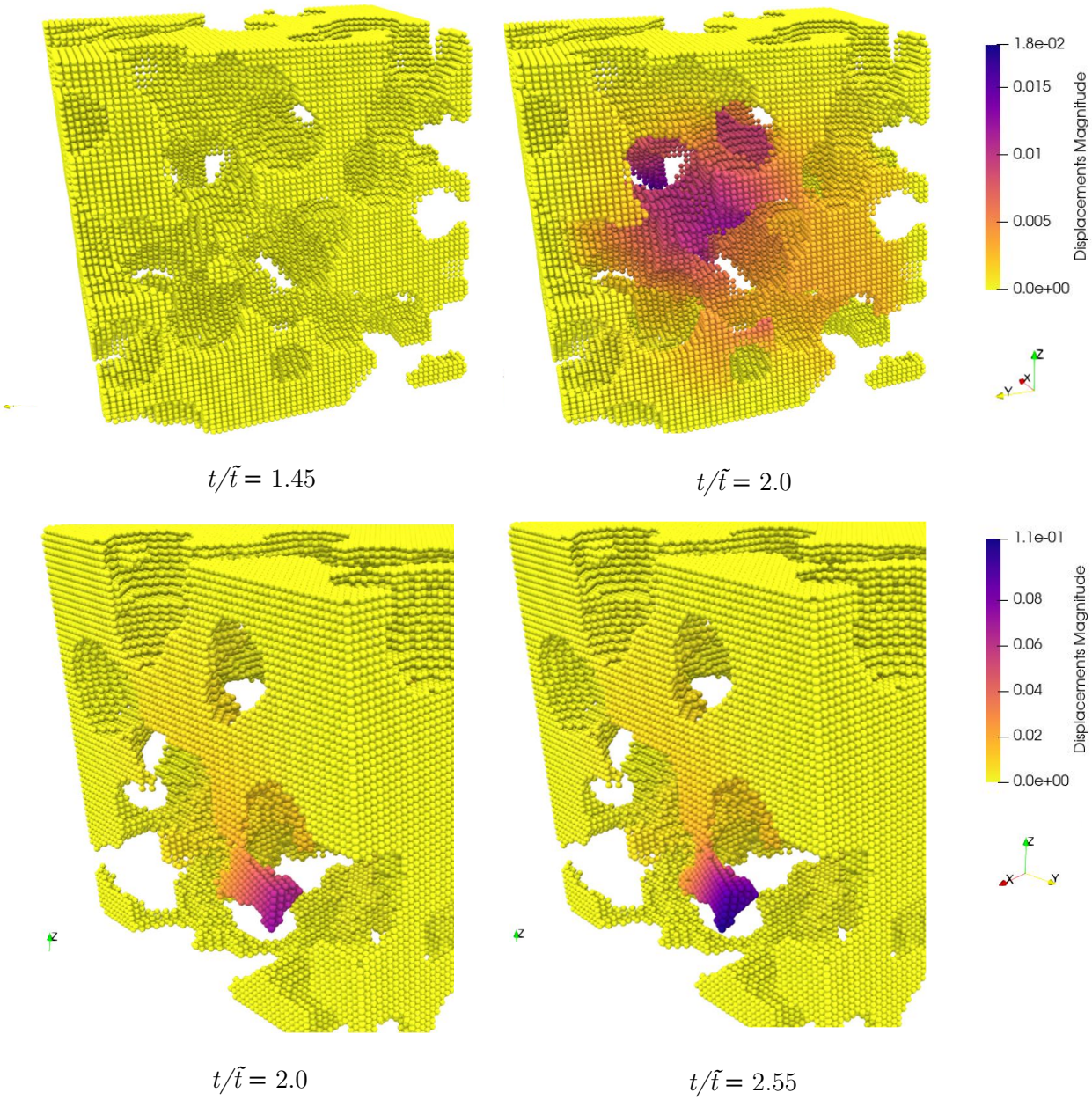

Figure 5.4: Surface contours of the non-dimensional displacement field on different regions of the solid body. Top panel: particle displacements at the inlet and inside the medium; bottom panel: particle displacements at the outlet of the medium.

The phenomenon can be further explored by studying the force density distribution: (fig. 5.4)

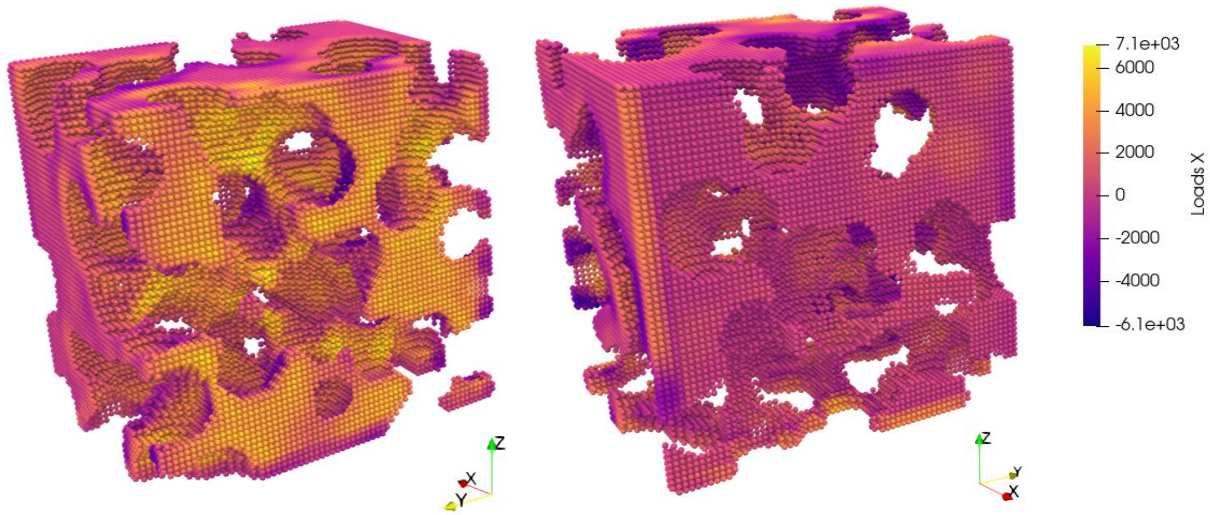

Figure 5.4: Surface contours of the non-dimensional x-wise IBM-force density field on the solid frame at $t/\tilde{t}$ =2.0; left: inlet view; right: outlet view.

As expected, force density distribution is maximum on the front surface of the body and minimum on its back surface. When moving inside the cavities, however, the computed force becomes negative along the internal solid walls that are opposite to the fluid flow; in particular, this can be seen observing the porous frame from the rear. This effect is caused by the internal pore-pressure that accumulates when the porous medium reaches a state of saturation. This pressure counterbalances moderately the fluid force acting along the positive x-axis, stabilizing the overall impact caused by the flow. However, this is not true for the walls on the backside: at the outlet of the porous frame pore-pressure immediately drops to zero, as we have already seen in figure (5.2); this justifies the scale difference in the displacement field that was noted in figure (5.3) and furtherly gives reasons to the fracturing process that will be reviews later. It is still unclear whether this effect is influenced by the proximity of the pressure outlet condition or not.

In figure (5.5) we can observe from another point of view the same phenomenon. The PDF distribution associated to the force density along x appears slightly asymmetrical on the positive side: even though negative forces along x are present, the overall fluid response is reasonably streamwise. The overall effect could be further examined by evaluating the total probability assigned to negative force density. This can be obtained with the relative CDF distribution; again, the plot is asymmetrical and the related probability for negative force density is around 0.4.

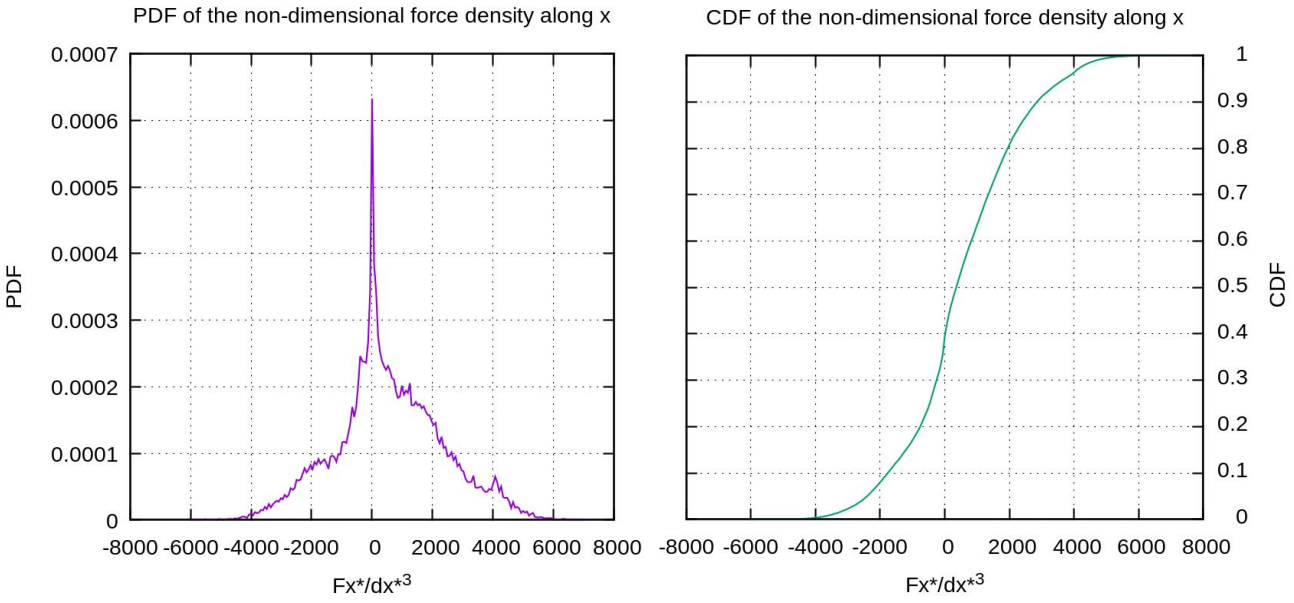

Figure 5.5: Probability density function and cumulative density function of the non-dimensional force density distribution at $t/\tilde{t}$ =2.0.

As regards to force density distributions along the y and z axes, assuming that the solid frame is associated to a isotropic-homogenous body (given that the random process that generates it is isotropic), we should obtain two symmetrical PDF distributions corresponding to a null resultant in both y and z directions. In figure (5.6) we see that this is fairly true for both cases:

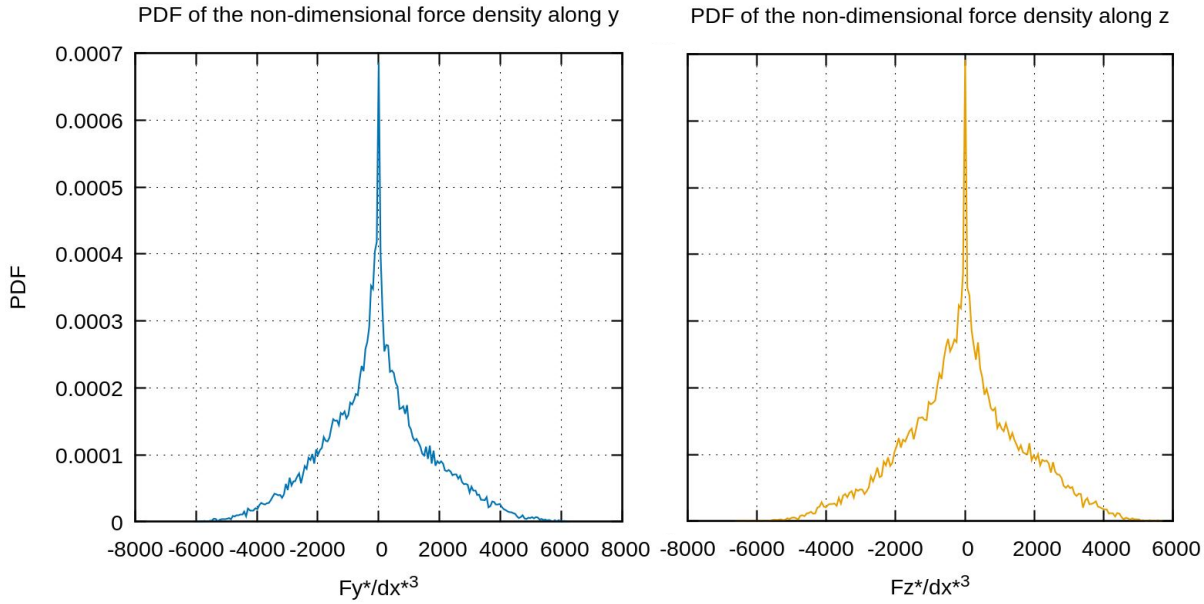

Figure 5.6: Probability density function and cumulative density function of the non-dimensional force density distribution at $t/\tilde{t}$ =2.0. Note that boundary points have been suppressed in order to cancel the effects caused by reaction forces.

5.1.3 Hydraulic fracturing

Now that the initialization process applied to the simulation has been reviewed, let us move on to evaluate the results obtained activating the bond break-up. The interval that will be considered is $t/\tilde{t} \in [2.55, 3.35]$ with a total of 6000 iterations. The value set for the energy release rate is associated to the non-dimensional ratio $G_0/EL = 5 \cdot 10^{-6}$ that has been considered optimal for reviewing the crack propagation and the related fracturing process.

Let us start by reporting in figure (5.7) and (5.8) the initial phases of the process, in particular the crack formation and subsequent development; this can be done by observing the contour surfaces associated to the damage factor (eq. 3.32):

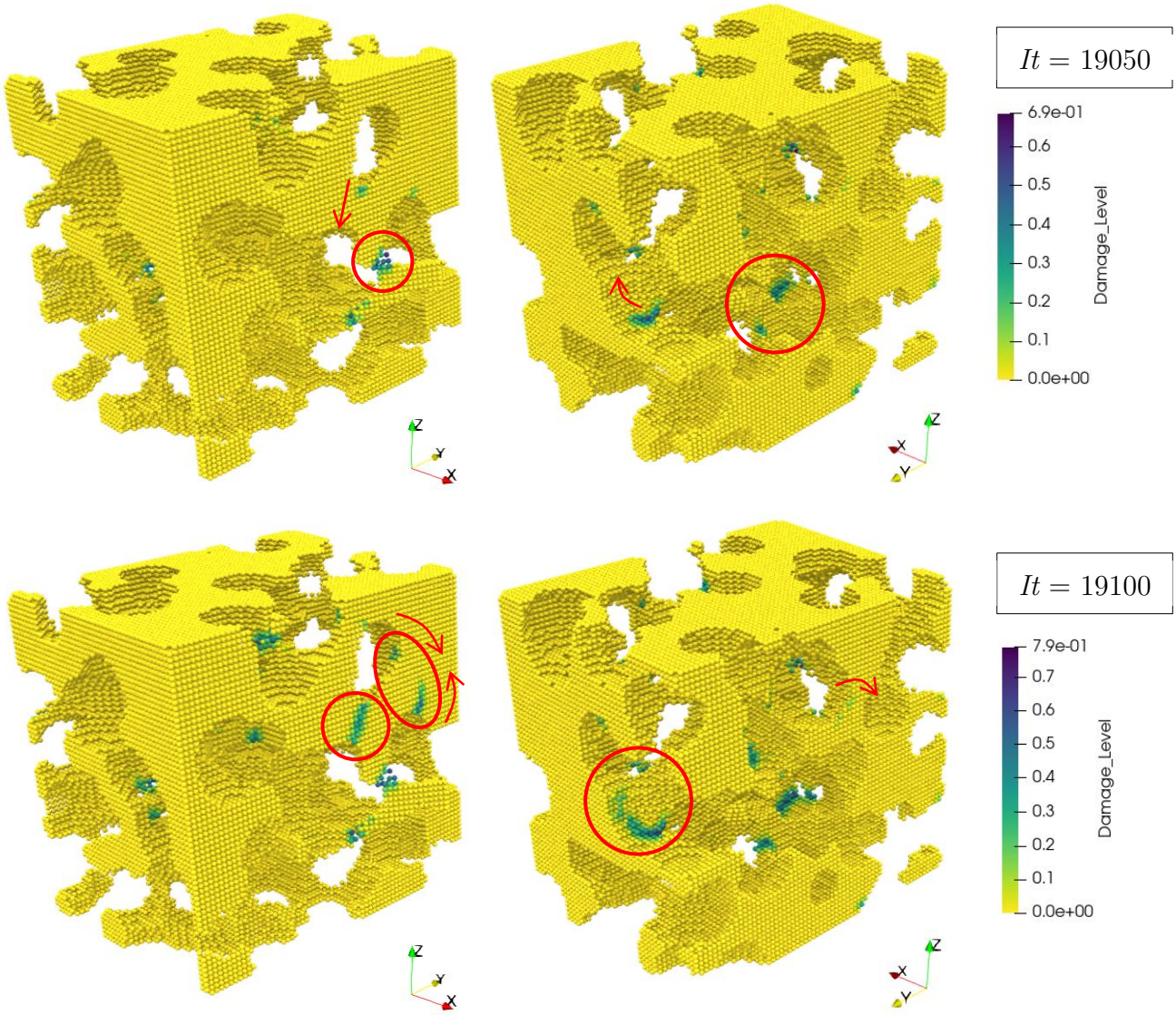

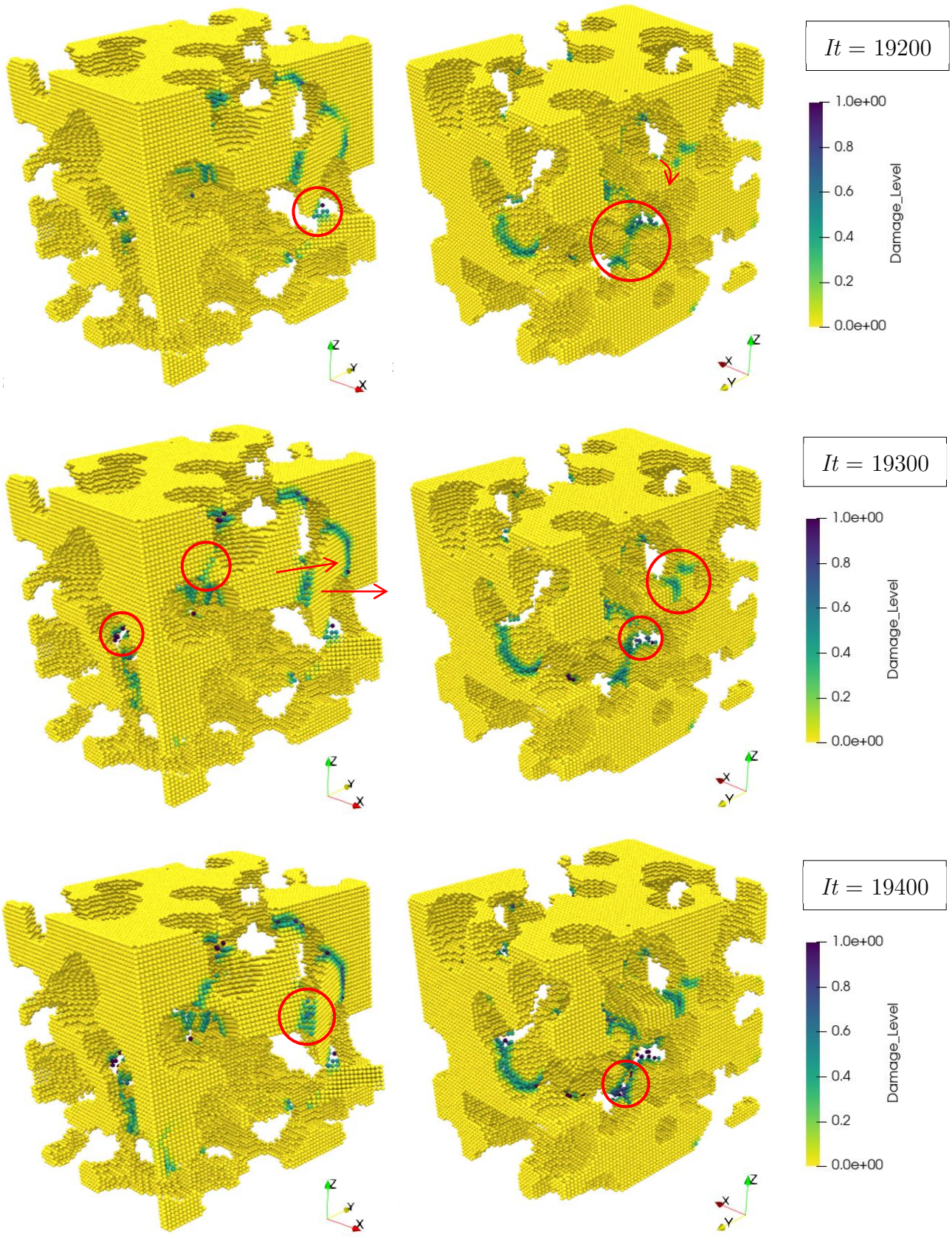

Figure 5.7: Damage factor distributions on the surface of the body to indicate crack propagation; the process is observed from two opposite views to ease the visualization.

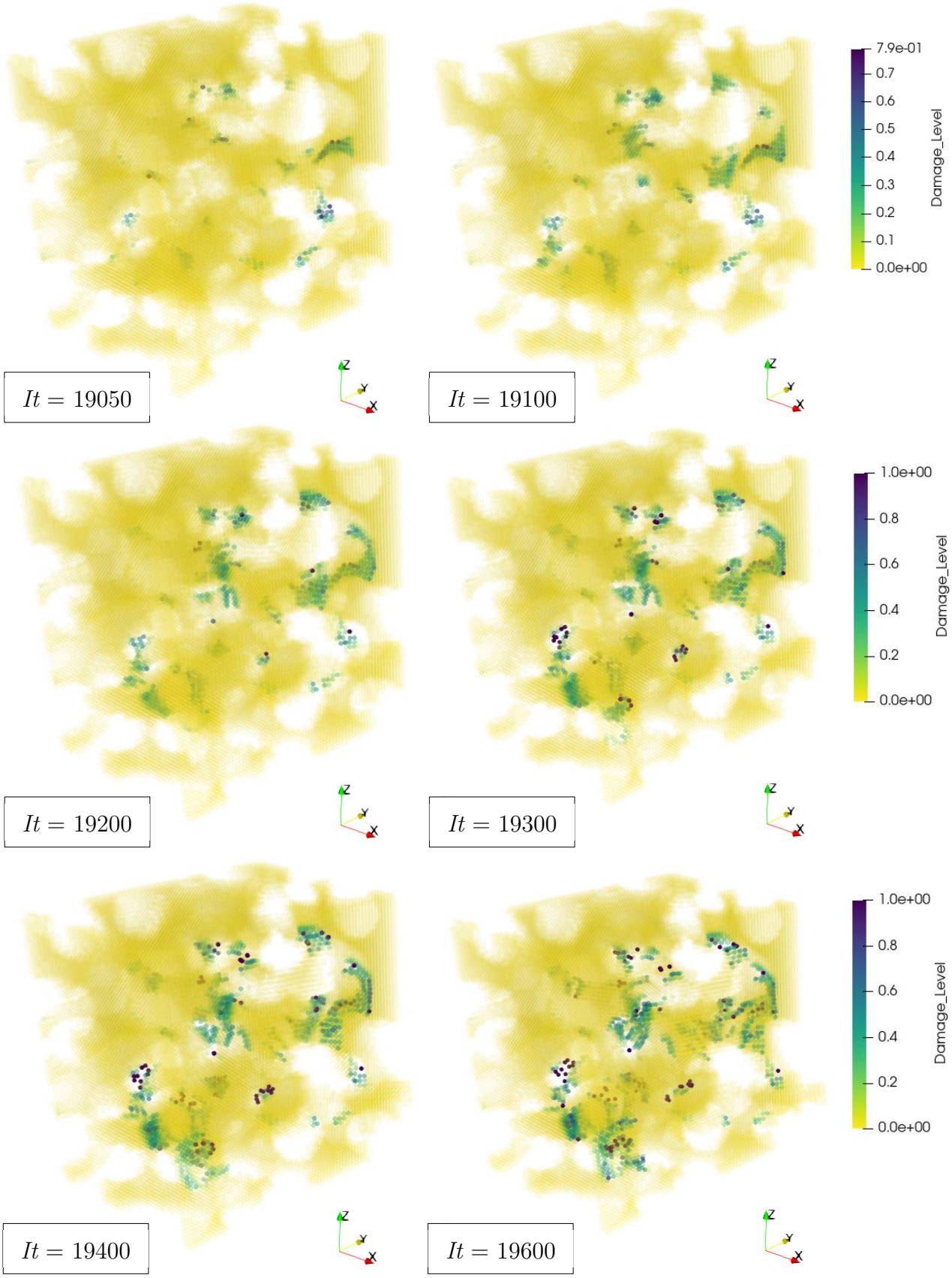

Figure 5.8: Damage factor distributions on the surface of the body to indicate crack propagation; the opacity of the undamaged material has been decreased to ease visualization.

Starting with iteration 19050, we can see how material damage is localized in particular at the backside of the frame, where a strip of the solid that has been deformed in the past iterations is almost already ripped off. A front view reveals instead that some crack are rapidly propagating along the internal connecting walls of the cavities. After 50 iterations ($t^* = 7.35 \cdot 10^{-3}$) the maximum material damage rises from 0.7 to 0.8 and cracks furtherly propagate; we can observe how damage tends to advance along perpendicular directions to the void volume, connecting pores together. This is in agreement with the considerations of fracture mechanics, where cracks are assumed to develop along the directions where the material is weaker (i.e. from one hole of a plate to another). In our case, we can see how cracks indeed spread from two opposite directions, starting from one pore and connecting to the other, mutually closing the gap of the material wall that separates pores' space (chap. 2.3.1, fig. 2.13).

At iteration 19200 damage level reaches 1.0 and the material finally breaks on the tightest corner that attached the solid strip to the porous frame; at the same time, the back walls are further warped and pushed outwards, causing even more stretching on the bonds that maintained the backside joined. The back frame ultimately collapses at iteration 19400: cracks are completely open and the central core of the material detaches from the front wall. As we have already evaluated in the previous pages, we note how internal pore pressure delays the rupture of frontal and core structures, despite those being subjected to the highest values of hydraulic pressure.

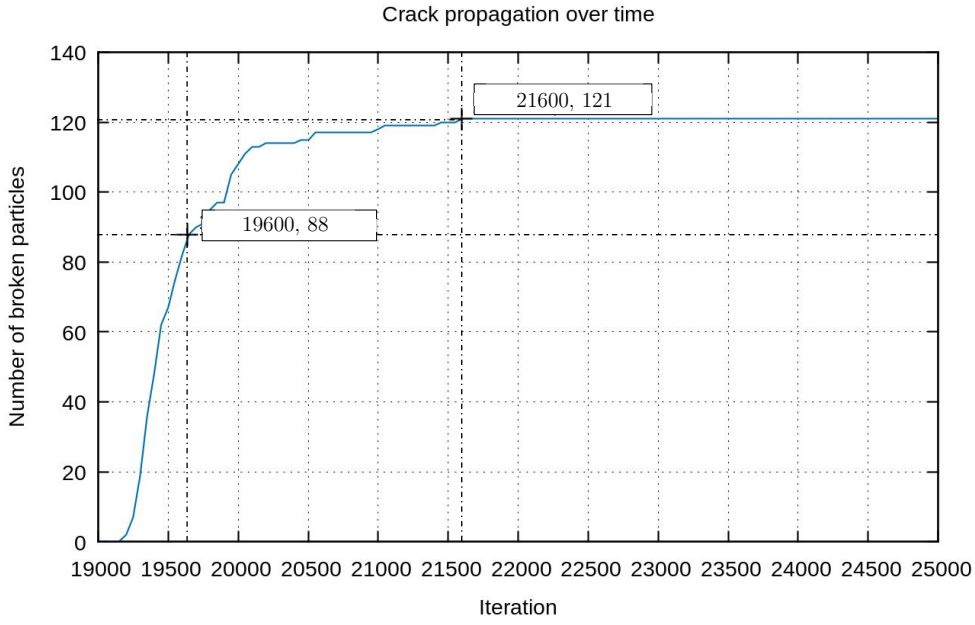

Figure 5.9: Number of broken particles over the time $t/\tilde{t} \in [2.55, 3.35]$. Iteration 19600 and 21600 are highlighted to compare the velocity of the process.

The hydraulic fracturing process starts, in this way, from the backside of the porous medium, pulling away fragments of the outlet which in turn drag along the material at the core. After iteration 19600, the number of broken bonds does not significantly rises, as the main solid fragments have already been formed and cracks does not propagate any more (fig. 5.9). The material continues to be damaged but the rate decreases, as the inlet pressure now only pushes the fragments downstream, reducing in this way the stretching of internal walls. The damage process after iteration 19600 becomes more similar to an erosion process, where fluid flow gradually wears out internal walls, dragging single solid particles through the outflow. At $t/\tilde{t} = 2.85$ (iteration 21600) the number of broken particles reaches its maximum and the process stabilizes; the flow in the porous medium is again stationary.

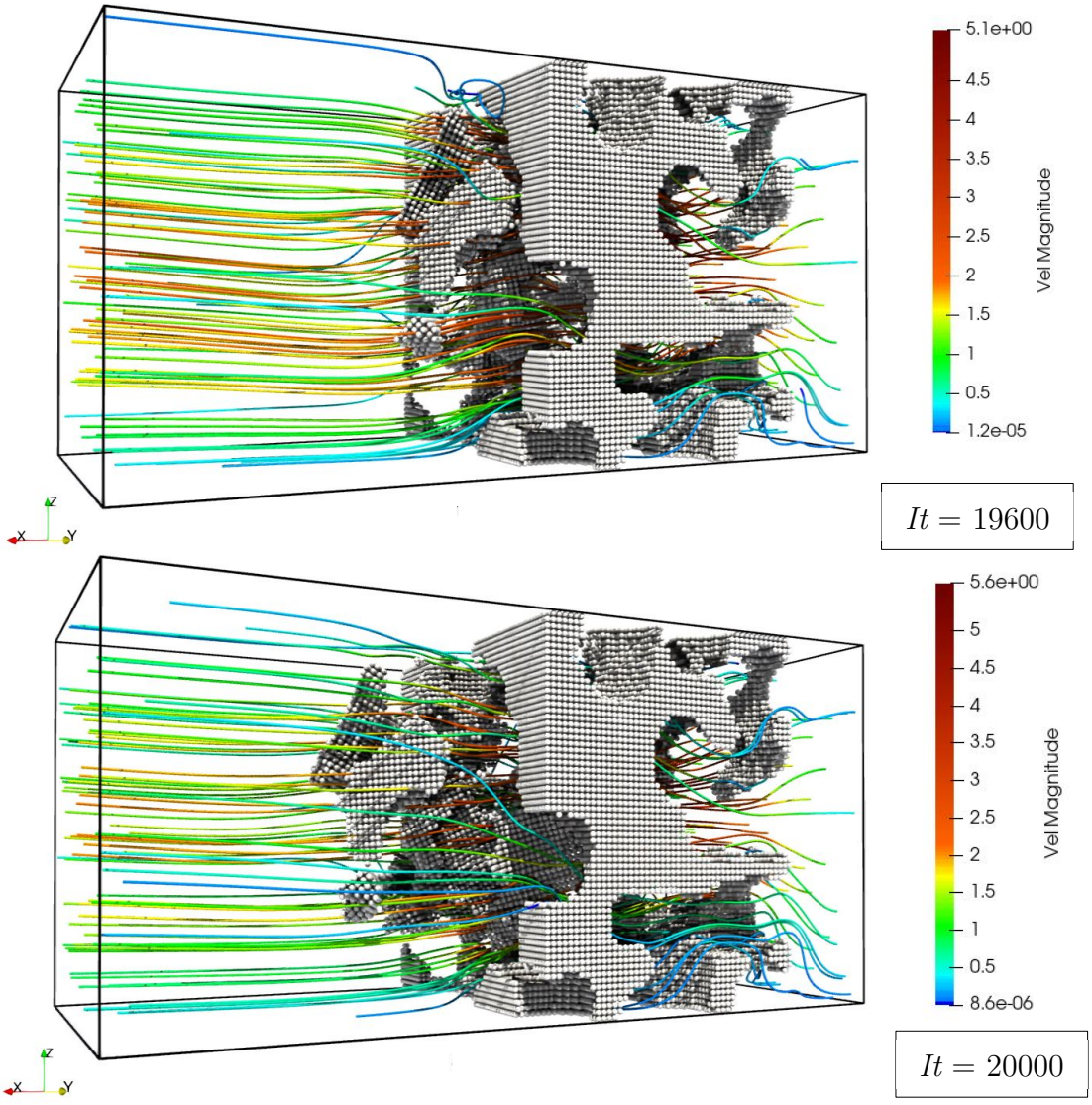

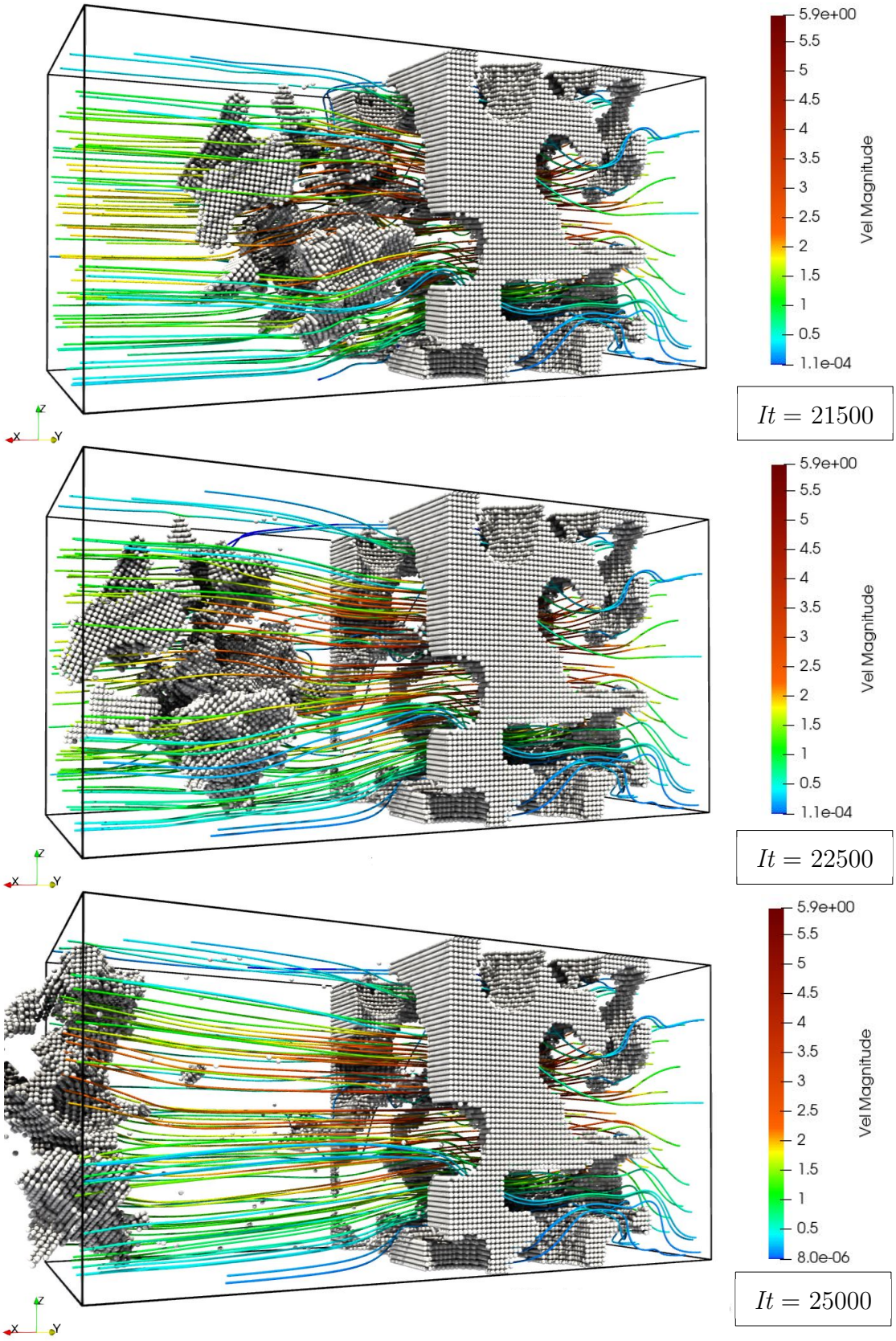

Figure 5.10: Hydraulic fracturing process; plot of flow streamlines, coloured according to the magnitude of the non-dimensional flow velocity together with a 3D render of the porous medium.

In figure (5.10) are reported 3D renders of the porous material when macroscopical effects related to the fracturing process are visible. As stated before, we can see how fluid flow gradually hollows out the solid frame, dragging downstream fragments that have been formed in the previous iterations. After iteration 21500, all the fragments have completely left the original solid domain ($x^* \in [0.25, 1.0]$); the fluid field and the damaged solid reaches a new stationary condition which is maintained until the end of the simulation. In figure (5.11) is reported the final configuration of the damaged porous medium.

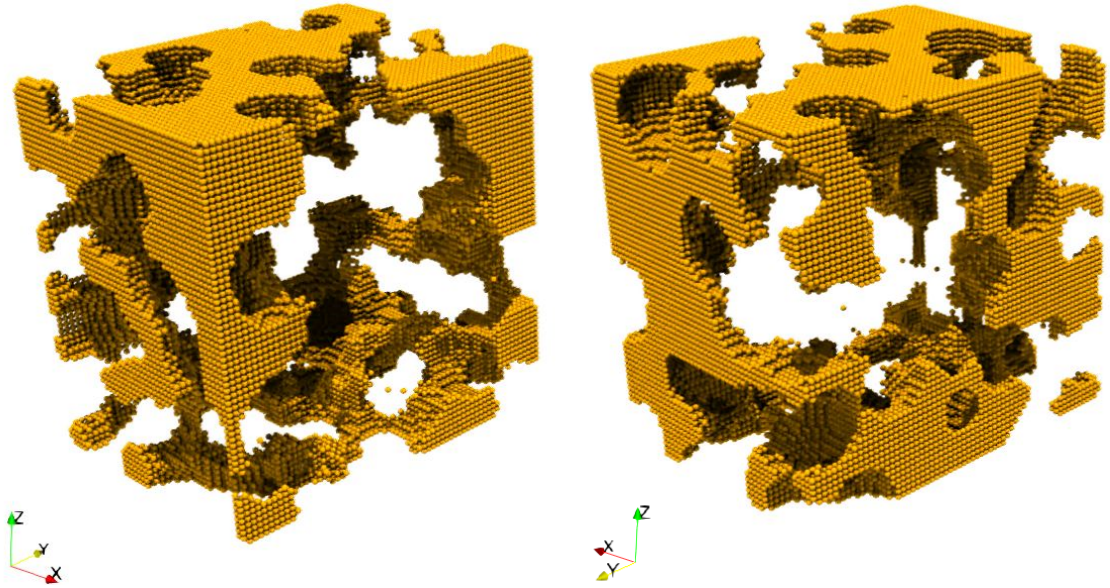

Figure 5.11: 3D render of the porous medium employed for the DNS analysis at end of the simulation.

5.2 Comparison of the cases

We present the results obtained by varying the setting of the energy release rate (see table 5.1) in order to evaluate different fracturing conditions. The non-dimensional ratio G_0/EL has been set to a minimum of $1 \cdot 10^{-6}$ (R1), where the entire porous structure shatters due to the hydraulic pressure, and to a maximum of $1.5 \cdot 10^{-5}$ (R15), where the solid frame remains globally intact; higher values of G_0 could not be evaluated as the simulation diverge due to large quasi-instantaneous deformations. In figure (5.12) are reported the final configuration of the damage porous structure for each individual case:

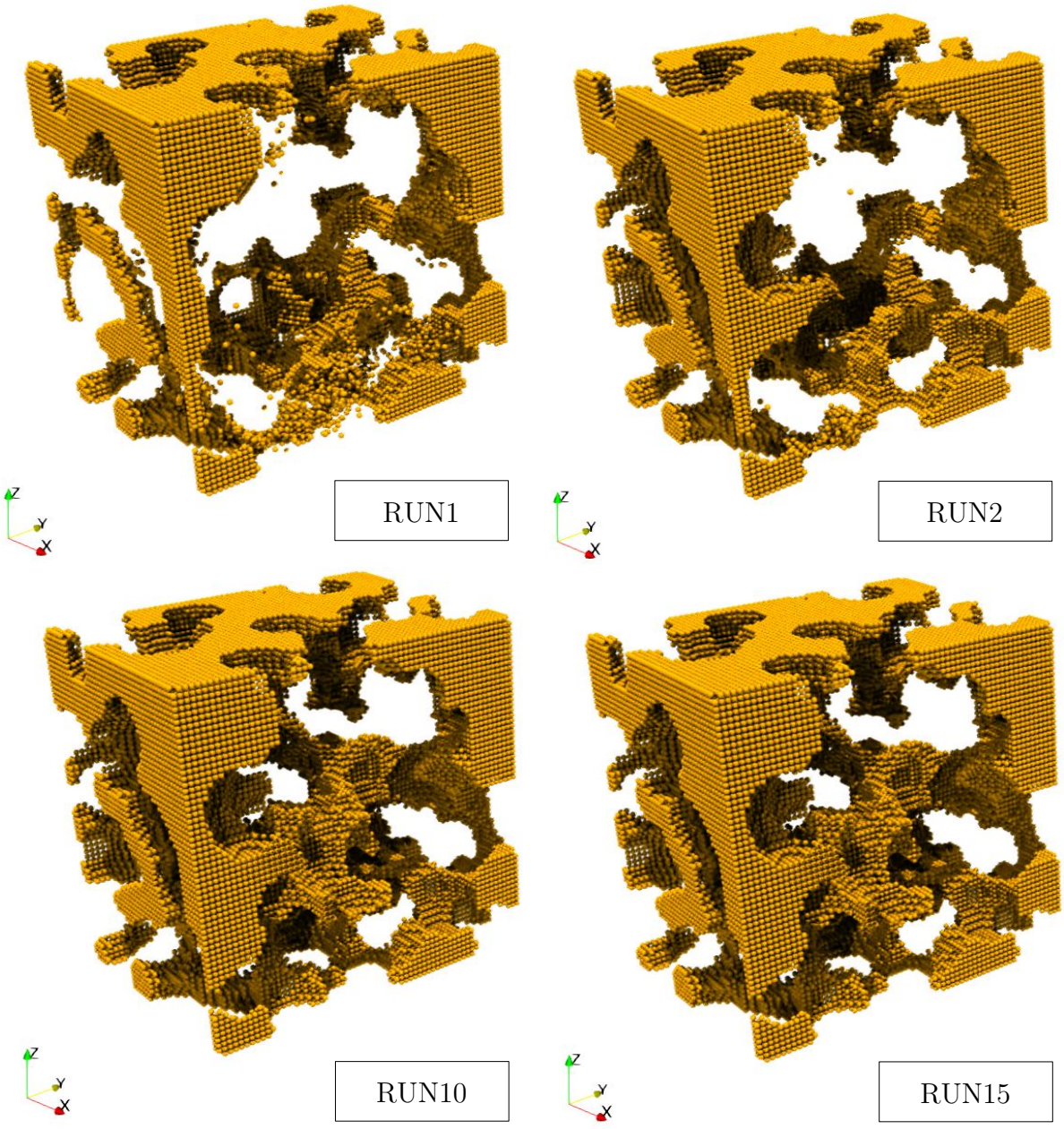

Figure 5.12: 3D renders of porous media structural configuration at the end of each corresponding simulation (R1,R2,R10 and R15).

5.2.1 Comparison of the structural evolution

We can confront the evolution of the porous material during the hydraulic fracturing process by comparing the trend of their relative structural quantities (porosity, tortuosity, specific surface area and number of broken particles) over time. These quantities have been computed separately at the end of each

simulation, evaluating the fluid and solid data with a specific post-processing algorithm. We report the results obtained for each of the cases:

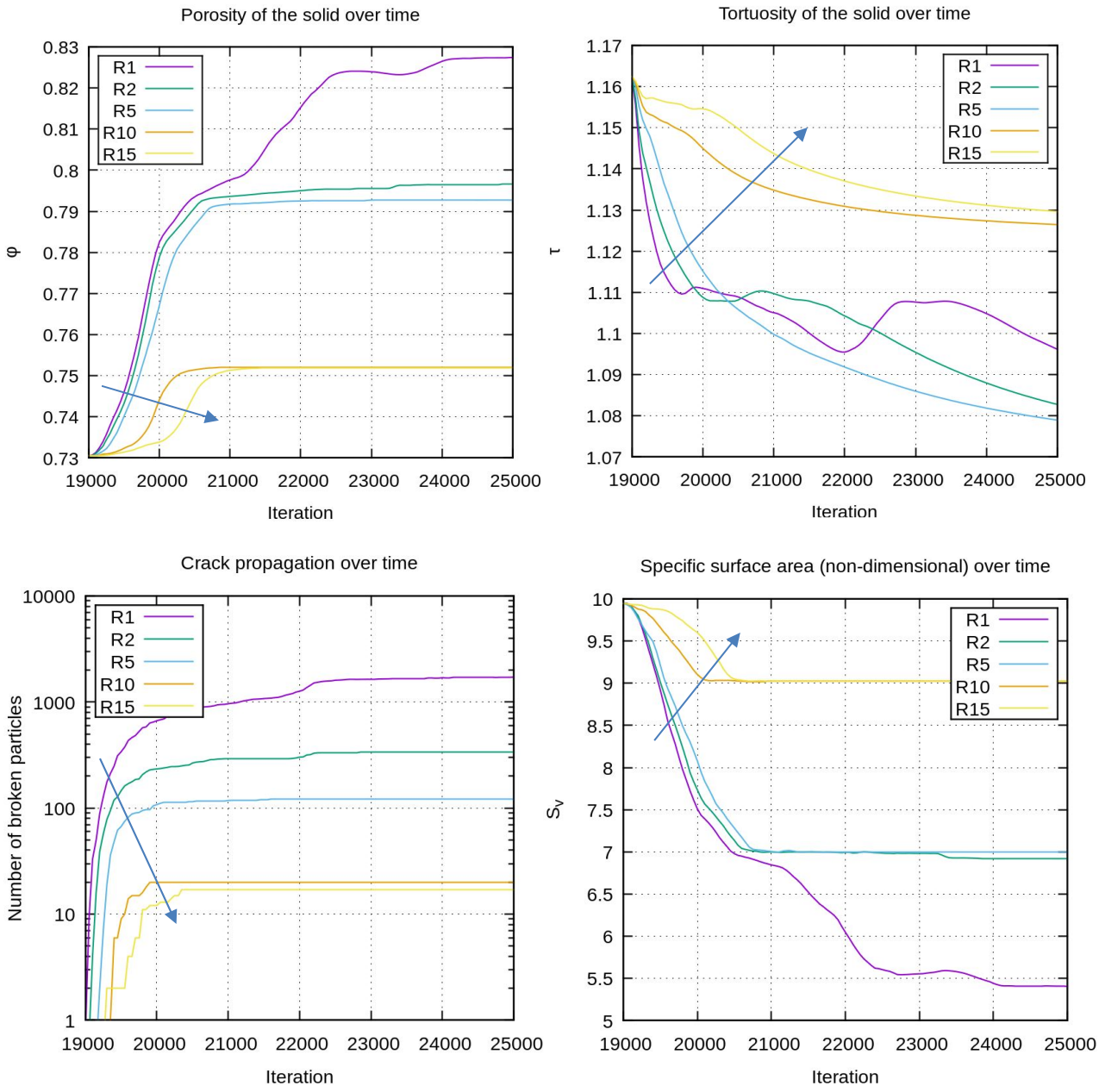

Figure 5.13: Comparison of the structural quantities of every tested configuration (R1,R2,R5,R10 and R15) over time. Arrows points in direction of increasing energy release rate.

In figure (5.13) we can evaluate the effect that hydraulic fracturing has on the structural quantities associated to the different configurations. We note immediately how RUN1 (and in some cases also RUN2) presents the most irregular plot and does not follow the overall trend displayed by the other configurations.

This is probably associated to how the fracturing process develops for RUN1: the solid shatters immediately in small fragments and single peridynamic particles are caught up downstream by the fluid. Some of these particles, however, recirculate and renter the solid frame, consequently disturbing the fluid flow. This effect does not happen when considering fracturing cases where fragments remain compact, meaning that the stronger gets the material and the less these quantities fluctuate. We expect that increasing the resolution of the computational domain could tone down these oscillations.

Let us move on and examine the trend of the different quantities. As expected, porosity rises as the porous medium breaks and fragments leave the solid domain, increasing the internal void space; the weakest configurations of the material (R1,R2,R5) respond almost immediately to the fluid pressure, displaying a steep rise of the porosity value in the first 1000 iterations. As already noted in the previous pages, when the solid fragments are completely dragged out of the porous frame, this rate progressively decreases until it reaches an almost stationary phase. On the contrary, the strongest configurations (R10 and R15) delay the fracturing process, moving the raise of porosity towards $It \in [20000, 21000]$. A similar trend can be observed by evaluating the number of broken particles; the first particle that breaks in RUN1 is around the first dozen of iterations, while in RUN15 the process starts around $It \in [19400, 19500]$.

The computed tortuosity of the media manifests a trend of decrease much more gradual (except for R1 and R2); τ progressively draws near to 1 as the solid frame is hollowed out by the flow; being dependent on the velocity field, it is subjected to fluctuations for R1 and R2, as the small fragments produced in these two cases generate noise in the average velocity field. Indeed, these oscillations manifest around $It \in [19500, 20000]$, where crack development has already happened and the fluid domain is filled with particles and chunks drifting downstream.

Interestingly, the specific surface area displays a trend which is almost symmetrical to porosity's. This is understandable given that both are purely geometrical dependent and related to the internal void volume of the porous frame.

5.2.2 Application of the capillary model

Let us further analyze the results by applying the capillary model that has been previously introduced (chapt. 4.2.3). The accuracy of the model will be evaluated for every simulation that has been performed and the results will be compared.

The first step consists on evaluating the mean pore radius associated to the dynamic structure of the porous material. Employing the capillary representation, we can compute the radius of the single capillary channel that traverses the solid frame. From equation (4.8) we obtain the following distribution of b over the fracturing process (fig. 5.14):

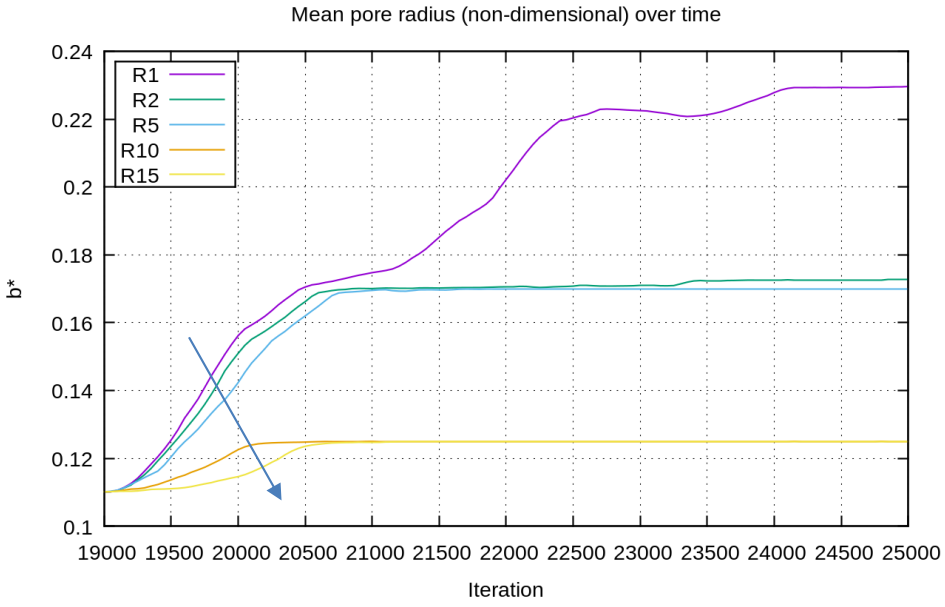

Figure 5.14: Comparison of the distribution of the non-dimensional mean pore radius (for configuration R1,R2,R5,R10 and R15) over time. Arrows points in direction of increasing energy release rate.

We can immediately evaluate the accuracy of the computed parameter by considering the value of $b*$ at $It = 19000$; we found that $b* \cong 0.113$ is fairly similar to the radius of the spheres employed in the generation process of the porous medium (Boolean subtraction, see chapt. 4.2.2). This validates the proposed model, confirming that the generated porous material is compatible with this geometrical representation. The same can be done by computing the total non-dimensional flow rate using the pressure obtained from the DNS. From equation (4.13b) obtain a value of around $Q*$=1.6, which again is similar to the reference value of Q^*_{ref}=1.0.

We can further evaluate the accuracy of the model throughout the fracturing process by computing the pressure drop using equation (4.13b) and comparing it to the one obtained from the simulation. Equation (4.13b) can be rewritten in the following way:

$$\Delta p(t)^* = Q^* \cdot \frac{L_b^*}{\varphi(t) Re} \cdot \frac{8[\tau(t)]^2}{[b(t)^*]^2 A^*} \tag{5.1}$$

In figure 5.15 are reported the results obtained for the different configurations.

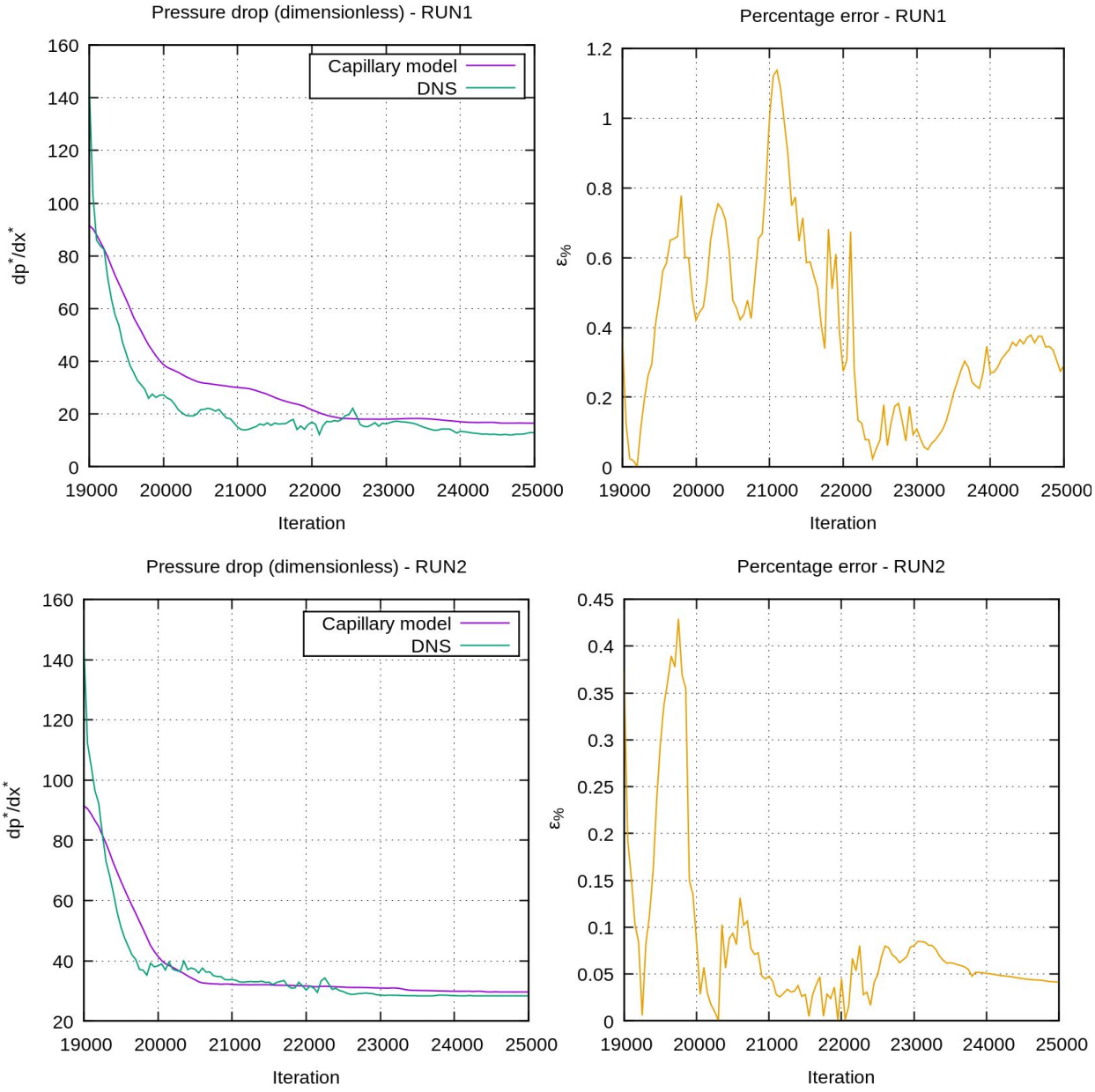

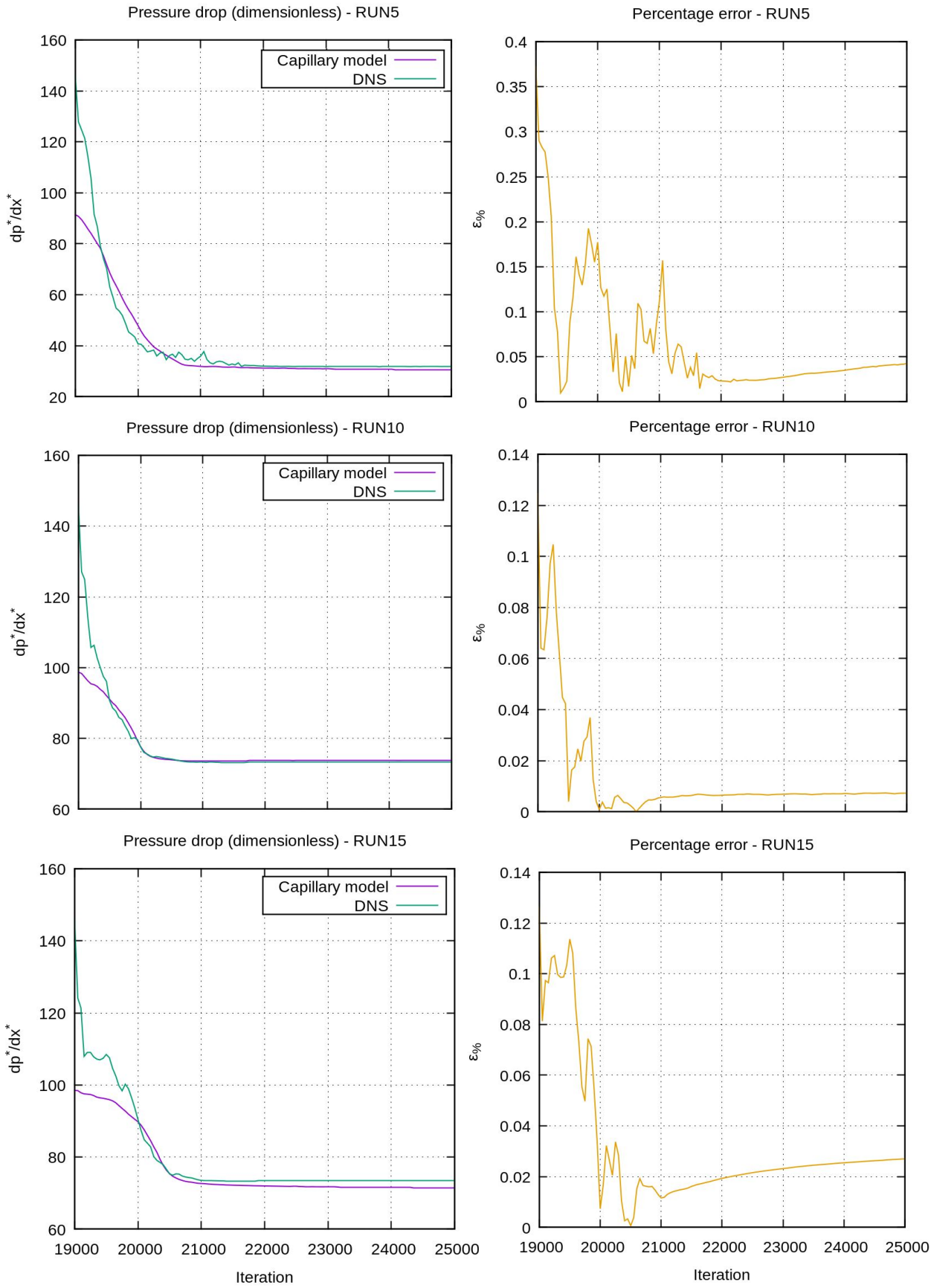

Figure 5.15: Distribution of the pressure drop computed with the capillary model together with the reference pressure drop obtained from the DNS (left); corresponding percentage error (right).

From figure (5.15) we can see how the results progressively gain accuracy as we move towards strongest configurations of the porous material. RUN1 and RUN2 are the cases most subjected to fluctuations of both the solution and the reference; these oscillations are related to the nature of the fracturing process, as it has been reviewed in the previous pages. Higher is the number of roaming broken particles and small chunks of detached material, and higher is the generated noise that affects the results of the simulation. We notice also that the initial pressure drop ($It =$ 19000) predicted by the capillary model is far lower than the one obtained through the DNS; this is probably related to pressure gradient distribution we observed in the previous chapter (see chapt. 5.1.1, fig. 5.3). The gap tends to cancel out after 100-200 iterations for the weaker configurations (R1,R2,R5), after more than 500 for the strongest ones (R10 and R15). This phenomenon could be explained by imagining that the progressive deformation of the structure at its backside progressively damps the drop in the pressure gradient, improving the overall compliance of the model to the retrieved data.

The best results are obtained for the R10 configuration, where the percentage error remains lower than 5% for most of the simulation time, settling for a minimum >1% for the remaining part. Here the fracturing process is the most stable, involving only the detachment of fragments of considerable size, without producing free roaming single particles. R15 configuration is similar; here, however, if we observe the trend associated to the number of broken particles (fig. 5.13), we note that the higher value of energy release rate delays the fracturing of the medium. In this way, the deformation of the frame is displayed only later, while in the meantime particles are pulled off from the internal surface, anticipating the erosion effect we usually grasp at the end of the process. It is possible that an increase of the computational domain resolution could enhance the results obtained both with the simulation and the model.

5.2.3 Failure prediction

It is clear that a failure criterion to predict the breaking of the material beforehand has not been proposed yet. Usually, failure criteria, being generical and applicable for a wide range of cases, are related usually to complex theories and requires detailed material analysis in order to evaluate the structural response to

the presented load configuration. In our case however, the employing of the peridynamics theory can ease the determination process of the critical parameter associated to the PMB solid. For example, we can estimate the ultimate tensile strength of a brittle peridynamic material considering, that in a pure traction condition (fracture mode I), the maximum bond stretch corresponds to the maximum linear deformation of the material. In this way, fracture occurs when the linear deformation along the stress direction reaches the limit bond stretch s_0; we can write [54]:

$$\sigma_f = E_{eff} s_0 = \sqrt{\frac{5 E_{eff} G_0}{6\delta}} = \sqrt{\frac{3 E_{eff} G_0}{32}} \tag{5.2}$$

E_{eff} is the effective Young's modulus of the porous material, which considers the morphological configuration of the solid frame. Usually computing E_{eff} requires empirical formulations, however, for a capillary model the relation can be expressed in the following way [67]:

$$E_{eff} = E\,(1\text{-}\,\varphi) \tag{5.3}$$

We can compute the estimated ultimate tensile strength for the different structural configurations:

DNS	R1	R2	R5	R10	R15
$\sigma_f \,/\, \tau_w$	29.182	41.270	65.253	**92.282**	113.021

Table 5.2: Ratio of the ultimate tensile strength to the wall shear stress for the different structural configurations.

where $\tau_w = b\,\Delta p\,/2L_b\,\tau$ is the wall shear stress computed in the single capillary tube. The axial stress applied to a porous medium can be evaluated starting from the pressure drop applied to the solid frame at the beginning of the fracturing process; we can see from their distribution over time that the trends are similar (fig. 5.16). An empirical model has been introduced to evaluate the resultant axial force applied to the porous material:

$$F_x \cong \frac{\Delta p A}{c\varphi^2} \tag{5.4}$$

where $c = 3.61$ is a geometrical constant related to the capillary model.

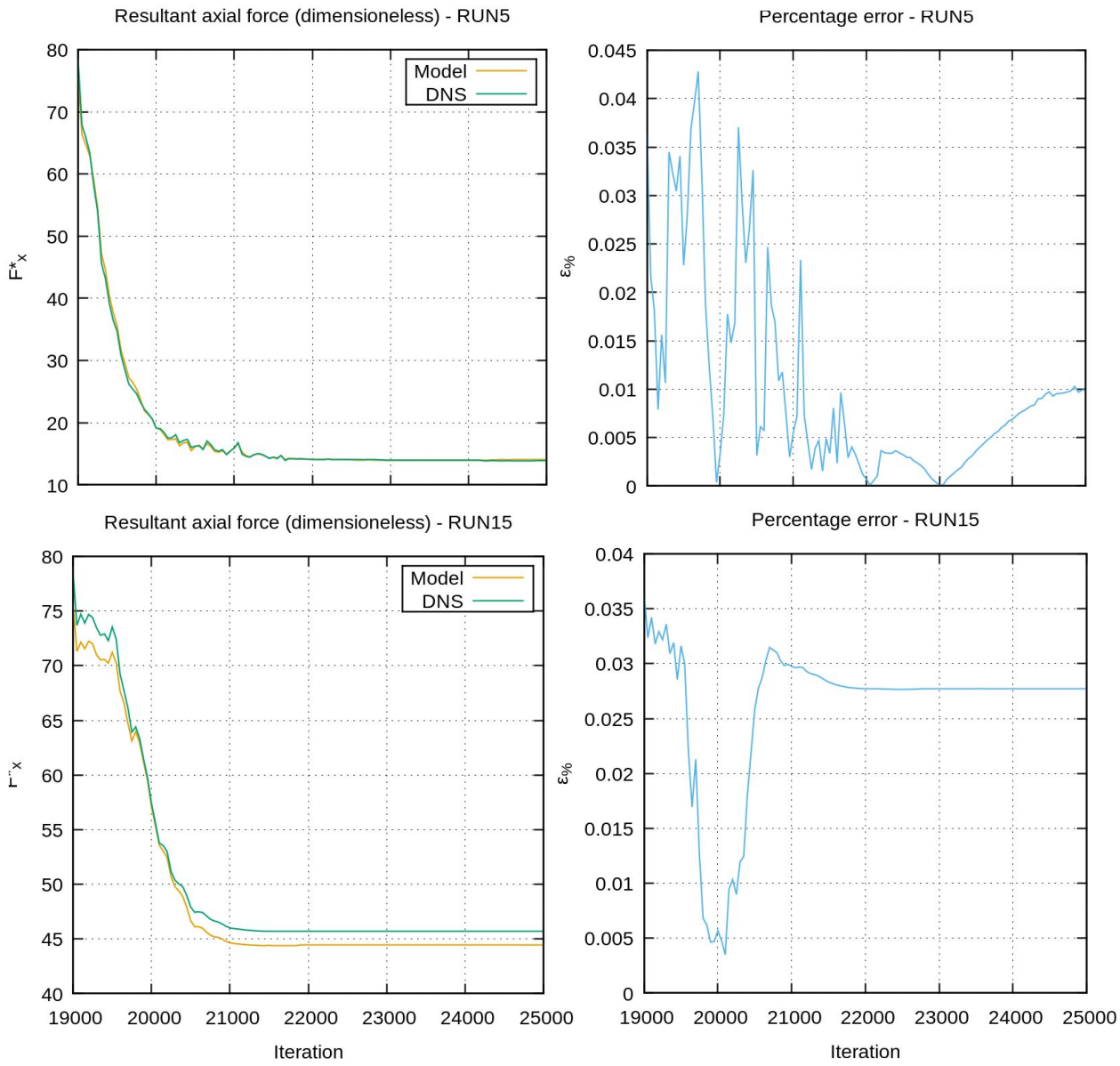

Figure 5.16: Distribution of the non-dimensional resultant axial force computed with equation (5.4) together with the reference resultant axial force obtained from the DNS (left) for R5 and R15 configurations; corresponding percentage error (right).

We can then compute the resultant axial stress in the following way:

$$\sigma_x \cong \frac{F_x}{(1 - \varphi)A} \tag{5.5}$$

Finally, we obtain $\sigma_x / \tau_w = 3080.4$, which is considerably higher than the ultimate tensile strength computed for every tested configuration. If we relate equation (5.5) with equation (5.2), we can estimate approximately the pressure drop required for the porous medium to break:

$$\Delta p_{crit} \cong c\varphi^2 \sqrt{\frac{3E\,(1\text{-}\varphi)^3 G_0}{32}} \tag{5.6}$$

Equation (5.6) can evaluate the critical pressure drop that has to be applied to a brittle porous material of initial porosity φ and Young's modulus E to initiate hydraulic fracturing. It should be noted that this relation has been derived on the hypothesis that the geometry is represented through the capillary model and the solid properties are those of an equivalent PMB material.

Chapter conclusion

The capillary model that was proposed provides acceptable solutions and successfully describes the hydraulic fracturing process over the course of time. Using the geometrical representation provided by the capillary model, an estimate of the critical pressure drop required to initiate hydraulic fracturing, has been derived. It is not excluded that an increase in the computational resolution could provide a better understanding of the phenomenon, reducing the noise caused by the dimension of the solid particles.

Chapter 6

Conclusions

The main achievement related to the present research work consisted in depicting the hydraulic fracturing process applied to porous materials caused by a laminar fluid filtering inside. This aspect represents a typical fluid-structure interaction problem and is of interest for several research areas that involve porous materials and complex geometries, as it has already been expressed before.

Navier-Stokes equations have been implemented and solved by performing a Direct Numerical Simulation of the fluid flow; the computation was carried on employing the already validated and tested CaNS-ExPS ([2],[63]), which implement a partitioned-loosely coupled approach, interfacing the fluid DNS solver together with a solid peridynamic solver. Interface detection and boundary conditions are managed through the employment of an Immersed Boundary Method based module, which allows to track the movement of solid borders through the fluid flow without the necessity of a remeshing procedure.

Five different DNSs have been performed to compare the effects of the fracturing process and crack development for several levels of solid strength, which in our case is represented by the variation of the corresponding energy release rate of the material. The fracturing process has been successfully displayed both via the DNS analysis and also via the implementation of an equivalent capillary model, representative of the complex internal geometry of the porous frame. The temporal geometry evolution related to the fractured solid frame was accurately displayed by the capillary model, correctly predicting the trend of increasing porosity which characterizes the frame throughout the process. A first approximation of the critical pressure gradient required for the porous frame to fracture has been proposed, assuming the geometry to be represented by the capillary model and introducing a basic model to predict the resultant streamwise axial force.

Regarding future perspectives, further analysis is required to evaluate the effectiveness of the methods presented, as the results obtained from a pore-scale simulation employing an equivalent brittle material could not transpose properly for real-case scenarios. Both the capillary model and equation (5.6) have been tested only for the cases presented in the previous sections, so a broader implementation could provide more general results, allowing an additional fine-tuning of the final model to help us perform more accurate predictions.

For now, the most significant limitation that was encountered resided in the large computational cost required to perform the Direct Numerical Simulation; this consequently restricted the resolution associated to the fluid and solid domain, reducing the overall accuracy of the simulation and generating noise on the final results. Moreover, the characteristics of the solid and fluid phase were set accordingly to these computational constraints, in order to anticipate the fracturing event and reduce the number of iterations required to complete the process. Either way, the solid configuration and the choice of the selected parameters should still be considered realistic, given the scale level chosen for the simulation.

We understand how the formulation of a more refined mathematical model is needed; this would allow to immediately predict the response of the solid and fluid phase, without resorting to heavy computational procedures that require time to be set up and properly optimized. In conclusion, future development should envision new strategies to model the interaction problem starting from the data collected from the performed analysis.

Bibliography

[1] Earl H. Dowell, Kenneth C. Hall, Modeling of fluid-structure interaction, *Annual Review of Fluid Mechanics,* Volume 33, 2001, Pages 445-490.

[2] Dalla Barba, F., Picano, F., A Novel Approach for Direct Numerical Simulation of Hydraulic Fracture Problems. *Flow, Turbulence and Combustion,* Volume 105, 2020, Pages 335–357.

[3] Hou, G., Wang, J., Layton, A. Numerical Methods for Fluid-Structure Interaction — A Review. *Communications in Computational Physics*, Volume 12, Issue 2, 2012, Pages 337-377.

[4] Farrukh Mazhar *et al.* On the meshfree particle methods for fluid-structure interaction problems, *Engineering Analysis with Boundary Elements,* Volume 124, 2021, Pages 14-40, ISSN 0955-7997.

[5] Javed A. (2015), Investigation on meshfree particle methods for fluid structure interaction problems. *University of Southampton, Engineering and the Environment, Doctoral Thesis,* 244pp.

[6] Adam C. Woodbury *et al.* Localized Coarsening of Conforming All-Hexahedral Meshes, *Engineering with Computers*, Volume 27, Issue 1, 2011, Pages 95-104.

[7] Bakker A. (2008), Lectures on applied computational fluid dynamics.

[8] Ariane M. *et al.* Discrete multi-physics: A mesh-free model of blood flow in flexible biological valve including solid aggregate formation, *PLoS ONE*, Volume 12, Issue 4, 2017.

[9] Henshaw W., Chesshire G., Multigrid on Composite Meshes, *Siam Journal on Scientific and Statistical Computing,* Volume 8, 1987, Pages 914-923.

[10] Bao-Lian Su (2011), Hierarchically Structured Porous Materials: From Nanoscience to Catalysis, Separation, Optics, Energy, and Life Science.

[11] Kerimov A. *et al.* The influence of convex particles' irregular shape and varying size on porosity, permeability, and elastic bulk modulus of granular porous media: Insights from numerical simulations. *Journal of Geophysical Research: Solid Earth*, Volume 123, 2018, Pages 10,563–10,582.

[12] Jinlong Fu, Hywel R. Thomas, Chenfeng Li, Tortuosity of porous media: Image analysis and physical simulation*, Earth-Science reviews*, Volume 212, 2021, ISSN 0012-8252.

[13] Ghanbarian B. *et al.* Tortuosity in Porous Media: A Critical Review*, Soil Science Society of America Journal*, Volume 77, 2013, Pages 1461-1477.

[14] Mondal S., Sibanda P., Computational study on convective flows in presence of chemical reaction and thermal radiation in porous/non-porous cavities, *Global Journal of Pure and Applied Mathematics,* Volume 12, Issue 4, 2016, Pages 3641-3671.

[15] Espinoza A, M., Sundén, B., Andersson, M., & Yuan, J. (2015). Analysis of Porosity and Tortuosity in a 2D Selected Region of Solid Oxide Fuel Cell Cathode Using the Lattice Boltzmann Method, *ECS Transactions,* Volume 65, 2015, Pages 59-73.

[16] Chueh C. C. *et al.*, Effective conductivity in random porous media with convex and non-convex porosity, *International Journal of Heat and Mass Transfer,* Volume 71, 2014, Pages 183-188, ISSN 0017-9310.

[17] Jinlong Fu, Hywel R. Thomas, Chenfeng Li, Tortuosity of porous media: Image analysis and physical simulation, *Earth-Science Reviews,* Volume 212, 2021, ISSN 0012-8252.

[18] Manjit Singh, Chanpreet Singh, Gangacharyulu Dasaroju (2016), Modelling for flow through unsaturated porous media with constant and variable density conditions using local thermal equilibrium. *Title of conference: 4th International Conference on Advancements in Engineering and Technology,* Sangur, Punjab.

[19] Zhilin Cheng *et al.,* The effect of pore structure on non-Darcy flow in porous media using the lattice Boltzmann method, *Journal of Petroleum Science and Engineering,* Volume 172, 2019, Pages 391-400, ISSN 0920-4105.

[20] Michael S. Newman, Xiaolong Yin, Lattice Boltzmann Simulation of Non-Darcy Flow In Stochastically Generated 2D Porous Media Geometries, *SPE Journal,* Volume 18, Issue 1, 2013, Pages 12-26.

[21] Clennell M., Tortuosity: A guide through the maze, *Geological Society London Special Publications*, Volume 122, Issue 1, 1997, Pages 299-344.

[22] Zhenhua C. *et al.,* Non-Darcy flow in disordered porous media: A lattice Boltzmann study, *Computers & Fluids,* Volume 39, Issue 10, 2010, Pages 2069-2077, ISSN 0045-7930.

[23] Costa, A., Permeability-porosity relationship: A reexamination of the Kozeny-Carman equation based on a fractal pore-space geometry assumption, *Geophysical Research Letters,* Volume 33, 2006.

[24] Panda M., Lake L., Estimation of Single-Phase Permeability from Parameters of Particle-Size Distribution, *AAPG Bulletin*, Volume 78, Issue 7, 1994, Pages 1028-1039.

[25] Hirasaki G. (2009), Flow and Transport in Porous Media I: Geology, Chemistry and Physics of Fluid Transports.

[26] Detournay, E., Cheng, A.H.-D., Fundamentals of poroelasticity, *Comprehensive Rock Engineering: Principles, Practice and Projects,* Volume 2, 1993, Pages 113-171.

[27] Binshan Ju, Yushu Wu, Tailiang Fan, Study on fluid flow in nonlinear elastic porous media: Experimental and modeling approaches, *Journal of Petroleum Science and Engineering,* Volume 76, Issues 3–4, 2011, Pages 205-211, ISSN 0920-4105.

[28] Gorbunov, A. A., Solov'eva, L.Ya., Pasechnik, V.A. Determination of the porous structure characteristics of sorbents by gel permeation chromatography of polymers, *Polymer Science U.S.S.R.,* Volume 26, Issue 5, 1984, Pages 1078-1086, ISSN 0032-3950.

[29] Huang T. *et al.* Pressure drop and fractal non-Darcy coefficient model for fluid flow through porous media, *Journal of Petroleum Science and Engineering,* Volume 184, 2020, 106579, ISSN 0920-4105.

[30] Liang-Ping *et al.* Phase field modeling of hydraulic fracturing in porous media formation with natural fracture. *Engineering Fracture Mechanics*. Volume 236, 2020, 107206, ISSN 0013-7944.

[31] Li Wang *et al.* A poromechanical model of hydraulic fracturing volumetric opening. *Engineering Fracture Mechanics*, Volume 235, 2020, 107172, ISSN 0013-7944.

[32] U.S. EPA. Plan to Study the Potential Impacts of Hydraulic Fracturing on Drinking Water Resources (Nov 2011). U.S. Environmental Protection Agency, Washington, DC, EPA/600/R-11/122A, 2012.

[33] Stephen G. Osborn *et al.* Methane contamination of drinking water accompanying gas-well drilling and hydraulic fracturing. *Proceedings of the National Academy of Sciences*, 2011, 108 (20), ISSN 8172-8176.

[34] M.Y. Wu *et al.* Numerical simulation of hydraulic fracturing based on two-dimensional surface fracture morphology reconstruction and combined finite-discrete element method. *Journal of Natural Gas Science and Engineering*, Volume 82, 2020, 103479, ISSN 1875-5100.

[35] Qi Zhao *et al.* Numerical simulation of hydraulic fracturing and associated microseismicity using finite-discrete element method, *Journal of Rock Mechanics and Geotechnical Engineering*, Volume 6, Issue 6, 2014, Pages 574-581, ISSN 1674-7755.

[36] Tao Ni *et al.* Hybrid FEM and peridynamic simulation of hydraulic fracture propagation in saturated porous media, *Computer Methods in Applied Mechanics and Engineering*, Volume 366, 2020, 113101, ISSN 0045-7825.

[37] William D. Norman Raymond, J. Jasinski, Erik B. Nelson (1996). Hydraulic fracturing process and compositions (U.S. Patent No. 5,551,516). U.S. Patent and Trademark Office.

[38] Healy, D. (2012). Hydraulic Fracturing or 'Fracking': A Short Summary of Current Knowledge and Potential Environmental Impacts. EPA Ireland.

[39] J. Adachi *et al.* Computer simulation of hydraulic fractures. *International Journal of Rock Mechanics and Mining Sciences*, Volume 44, Issue 5, 2007, Pages 739-757, ISSN 1365-1609.

[40] Pope, S. B. Turbulent flows. Cambridge University Press, 2000.

[41] Chorin, A.J. A numerical method for solving incompressible viscous flow problems, *Journal of Computational Physics*, Volume 2, Issue 1, 1967, Pages 12-26, ISSN 0021-9991.

[42] Picano, F. Laboratorio di fluidodinamica computazionale: modulo di modellistica e di simulazione fluidodinamica, 2020.

[43] De Vanna, F. Appunti del corso di Laboratorio di Fluidodinamica Computazionale, 2020.

[44] Orszag, S. Analytical theories of turbulence. *Journal of Fluid Mechanics*, Volume 41, Issue 2, 1970, Pages 363-386.

[45] Thomadakis, M., Leschziner, M. A pressure-correction method for the solution of incompressible viscous flows on unstructured grids, *Int. Journal for Numerical Meth. in Fluids,* Volume 22, 1996.

[46] Mittal, R., Iaccarino, G. Immersed boundary methods, *Annual Review of Fluid Mechanics,* Volume 37, 2005, Pages 239-261.

[47] Breugem, W.P. A second-order accurate immersed boundary method for fully resolved simulations of particle-laden flows, *Journal of Computational Physics*, Volume 231, Issue 13, 2012, Pages 4469-4498, ISSN 0021-9991.

[48] De Tullio, M.D. Pascazio, G. A moving-least-squares immersed boundary method for simulating the fluid–structure interaction of elastic bodies with arbitrary thickness, *Journal of Computational Physics*, Volume 325, 2016, Pages 201-225, ISSN 0021-9991.

[49] Wang, S., Vanella, M., Balaras, E. A hydrodynamic stress model for simulating turbulence/particle interactions with immersed boundary methods,

Journal of Computational Physics, Volume 382, 2019, Pages 240-263, ISSN 0021-9991.

[50] Fadlun, E.A. *et al.*, Combined Immersed-Boundary Finite-Difference Methods for Three-Dimensional Complex Flow Simulations, *Journal of Computational Physics*, Volume 161, Issue 1, 2000, Pages 35-60, ISSN 0021-9991.

[51] Vamsi Spandan *et al.,* A parallel interaction potential approach coupled with the immersed boundary method for fully resolved simulations of deformable interfaces and membranes, *Journal of Computational Physics*, Volume 348, 2017, Pages 567-590, ISSN 0021-9991.

[52] Roma A.M. *et al.* An adaptive version of the immersed boundary method. *Journal of computational physics*, Volume 153, Issue 2, 1999, Pages 509-534.

[53] Uhlmann, M. An immersed boundary method with direct forcing for the simulation of particulate flows, *Journal of Computational Physics*, Volume 209, Issue 2, 2005, Pages 448-476, ISSN 0021-9991.

[54] Dalla Barba, F., Picano, F. (2020) Direct numerical simulation of the scouring of a brittle stream-bed in a turbulent channel flow.

[55] Arman Shojaei Barjoui, 2018, On the coupling of peridynamics with the classical theory of continuum mechanics in a meshless framework. *Università degli Studi di Padova, Scienze Tecnologie e Misure Spaziali, Doctoral Thesis,* 158pp.

[56] Zaccariotto, M. (2020) Discontinuous mechanical problems studied with a peridynamics-based approach: simulation of fracture and damage propagation, *Title of the conference: innovative structures for lightweight vehicles,* CISM-UNIUD Advanced Webinar.

[57] Dipasquale, D. 2017, Adaptive grid refinement and scaling techniques applied to peridynamics, *Università degli Studi di Padova, Scienze Tecnologie e Misure Spaziali, Doctoral Thesis,* 156pp.

[58] Silling, S.A., Askari, E. A meshfree method based on the peridynamic model of solid mechanics, *Computers & Structures*, Volume 83, Issues 17–18, 2005, Pages 1526-1535, ISSN 0045-7949,

[59] Le, Q. V., Bobaru, F. Surface corrections for peridynamic models in elasticity and fracture, *Computational Mechanics*, Volume 61, Issue 4, 2018, Pages 1-20.

[60] Dipasquale, D. *et al.* Crack propagation with adaptive grid refinement in 2D peridynamics. *International Journal of Fracture*, Volume 190 (1-2), 2014.

[61] Dipasquale, D. *et al.* Dependence of crack paths on the orientation of regular 2D peridynamic grids, *Engineering Fracture Mechanics,* Volume 160, 2016, Pages 248-263, ISSN 0013-7944.

[62] Littlewood, D. J. (2015) Roadmap for Peridynamic Software Implementation.

[63] Costa, P. A FFT-based finite-difference solver for massively-parallel direct numerical simulations of turbulent flows, Computers & Mathematics with Applications, Volume 76, Issue 8, 2018, Pages 1853-1862, ISSN 0898-1221.

[64] Dalla Barba, F. *et al.* (2018) A fluid-structure interaction model based on peridynamics and navier-stokes equations for hydraulic fracture problems.

[65] Campagnari, P. Studio dell'interazione fluido-struttura con un metodo "immersed boundary" accoppiato alla peridinamica. *Università degli Studi di Padova, Master Thesis,* 56pp.

[66] Campice, A. Direct numerical simulation of the erosion of a wall of a turbulent channel, *Università degli Studi di Padova, Master Thesis,* 85pp.

[67] Phani, K.K., Niyogi, S.K. Young's modulus of porous brittle solids. *Journal of material science,* Volume 22, 1987, Pages 257–263.